Characterization of Brown Carbon absorption in different European environments through source contribution analysis

Hector Navarro-Barboza[1], Jordi Rovira[2], Vincenzo Obiso[1], Andrea Pozzer[3,4], Marta Via[2], Andres Alastuey[2], Xavier Querol[2], Noemi Perez[2], Marjan Savadkoohi[2,21], Gang Chen[5], Jesus Yus-Díez[6], Matic Ivancic[7], Martin Rigler[7], Konstantinos Eleftheriadis[8], Stergios Vratolis[8], Olga Zografou[8], Maria Gini[8], Benjamin Chazeau[9,20], Nicolas Marchand[9], Andre S.H. Prevot[9], Kaspar Dallenbach[9], Mikael Ehn[10], Krista Luoma[10,11], Tuukka Petäjä[10], Anna Tobler[12], Jaroslaw Necki[13], Minna Aurela[14], Hilkka Timonen[14], Jarkko Niemi[13], Olivier Favez[15], Jean-Eudes Petit[16], Jean-Philippe Putaud[17], Christoph Hueglin[18], Nicolas Pascal[19], Aurélien Chauvigné[19], Sébastien Conil[22], Marco Pandolfi[2], and Oriol Jorba[1]

[1]Barcelona Supercomputing Center, Plaça Eusebi Güell 1-3, Barcelona, 08034, Spain.
[2]Institute of Environmental Assessment and Water Research, c/Jordi-Girona 18-26, Barcelona, 08034, Spain.
[3]Atmospheric Chemistry Department, Max Planck Institute for Chemistry, Mainz, Germany.
[4]Climate and Atmosphere Research Center, The Cyprus Institute, Nicosia, Cyprus.
[5]MRC Centre for Environ. and Health, Environ. Research Group, Imperial College London, London, U.K.
[6]Centre for Atmospheric Research, University of Nova Gorica, Vipavska 11c, SI-5270 Ajdovščina, Slovenia.
[7]Aerosol d.o.o., Kamniška 39A, 1000 Ljubljana, Slovenia.
[8]ENRACT, Institute of Nuclear & Radiological Sciences & Technology, Energy & Safety, National Centre of Scientific Research "Demokritos", GR-15310 Ag. Paraskevi, Attica, Greece.
[9]Paul Scherrer Institute, PSI Center for Energy and Environmental Sciences.
[10]Institute for Atmospheric and Earth System Research/Physics, Faculty of Science, University of Helsinki, Helsinki, 00014, Finland.
[11]Atmospheric Research Centre of Eastern Finland, Finnish Meteorological Institute, Kuopio, Finland.
[12]Datalystica Ltd., Parkstrasse 1, 5234 Villigen, Switzerland.
[13]AGH University of Science and Technology, Faculty of Physics and Applied Computer Science, Department of Applied Nuclear Physics, Krakow, Poland
[14]Atmospheric Composition Research, Finnish Meteorological Institute, P.O. Box 503, 00101 Helsinki, Finland.
[15]Institut National de l'Environnement Industriel et des Risques (INERIS), 60550 Verneuil-en-Halatte, France.
[16]Laboratoire des Sciences du Climat et de l'Environnement, CEA CNRS UVSQ, Université Paris-Saclay, Gif-sur-Yvette, France.
[17]European Commission, Joint Research Centre (JRC), Ispra, Italy.
[18]Empa, Swiss Federal Laboratories for Materials Science and Technology, 8600 Duebendorf, Switzerland.
[19]Univ Lille, ICARE Data & Serv Ctr, CNRS, CNES,UMS 2877, Lille, France.
[20]Aix Marseille Univ, CNRS, LCE, Marseille, France.
[21]Department of Mining, Industrial and ICT Engineering (EMIT), Manresa School of Engineering (EPSEM), Universitat Politècnica de Catalunya (UPC), 08242 Manresa, Spain.
[22]Andra CMHM, DISTEC/EES, RD960, 55290 Bure, France.

Correspondence: Hector Navarro-Barboza (hector.navarro@bsc.es), Oriol Jorba (oriol.jorba@bsc.es)

Abstract.

Brown carbon (BrC) is a fraction of Organic Aerosols (OA) that absorbs radiation in the ultraviolet and short visible wavelengths. Its contribution to radiative forcing is uncertain due to limited knowledge of its imaginary refractive index (k). This study investigates the variability of k for OA from wildfires, residential, shipping, and traffic emission sources over Europe. The MONARCH atmospheric chemistry model simulated OA concentrations and source contributions, feeding an offline optical tool to constrain k values at 370 nm. The model was evaluated against OA mass concentrations from Aerosol Chemical Speciation Monitors (ACSM) and filter sample measurements, and aerosol light absorption measurements at 370 nm derived from Aethalometer[TM] from 12 sites across Europe. Results show that MONARCH captures the OA temporal variability across environments (regional, suburban and urban background). Residential emissions are a major OA source in colder months, while secondary organic aerosols (SOA) dominate in warmer periods. Traffic is a minor primary OA contributor. Biomass and coal combustion significantly influence OA absorption, with shipping emissions also notable near harbors. Optimizing k values at 370 nm revealed significant variability in OA light absorption, influenced by emission sources and environmental conditions. Derived k values for biomass burning (0.03 to 0.13), residential (0.008 to 0.13), shipping (0.005 to 0.08), and traffic (0.005 to 0.07) sources improved model representation of OA absorption compared to a constant k. Introducing such emission source-specific constraints is an innovative approach to enhance OA absorption in atmospheric models.

1   Introduction

Brown carbon (BrC) is the fraction of organic aerosols (OA) which exhibits light-absorbing properties, particularly in the
45   ultraviolet and visible spectrum (Andreae and Gelencsér, 2006; Laskin et al., 2015). The role of BrC in atmospheric radiative forcing, while possibly significant, remains incompletely quantified (Brown et al., 2018; Zhang et al., 2020a; Sand et al., 2021). This is in part due to the historical treatment of OA in atmospheric models as mostly scattering solar radiation (Feng et al., 2013). BrC emissions originate from a variety of sources, significantly influenced by regional factors, including biomass, biofuel, and fossil fuel (Lu et al., 2015) combustion. Global estimates of BrC emissions reveal distinct regional patterns (Xiong
50   et al., 2022). In Africa and South America, more than 70% of the primary BrC emissions are attributed to natural sources, such as wildfires. However, East Asia's BrC emissions are primarily anthropogenic, with residential solid fuel combustion accounting for more than 80% of the emissions. Europe presents a more mixed source profile, where natural sources are currently considered to be responsible for approximately 36% of BrC emissions, while residential activities (e.g., coal and solid biomass combustion for domestic heating) contribute approximately 48%. Furthermore, BrC is originating originates not
55   only through primary emissions, but also through secondary formation processes in the atmosphere, such as darkening (Kumar et al., 2018; Li et al., 2023). However, as BrC ages in the atmosphere, it can undergo photochemical and oxidative processes that lead to a reduction in its absorption capabilities, a phenomenon known as photobleaching (Hems et al., 2021). The complexity of BrC lies in its changing absorption characteristics and diverse composition. In fact, factors like burning conditions, solar exposure, and chemical composition determine BrC optical properties such as imaginary refractive index (k) and Absorption
60   Angstrom Exponent (AAE). The optical properties of BrC present a high variability that arises from the formation of different chromophores and molecular structures, thus complicating the representation of BrC in climate models and our understanding of its atmospheric impact (Laskin et al., 2015; Brege et al., 2021; Washenfelder et al., 2022).

Several processes that alter BrC absorptive characteristics have recently been identified. Photobleaching stands out as a key process in this context. It describes the phenomenon in which BrC loses its absorptive capacity, particularly under conditions of
65   high OH oxidation. For instance, a laboratory study conducted by Wong et al. (2019) observed that high-molecular weight BrC undergoes initial photoenhancement and subsequent gradual photobleaching, a phenomenon supported by observations from ambient BrC samples collected during fire seasons in Heraklion, Crete, Greece. Both primary and secondary BrC are subject to photobleaching, as shown in various studies, e.g. Forrister et al. (2015); Wang et al. (2018b). Contrasting photobleaching, Kodros et al. (2020) introduced the concept of "dark aging" or darkening, a novel BrC secondary organic aerosol (SOA)

70 formation pathway from biomass burning emissions. This process, which occurs under low or no light conditions and takes hours, involves OA oxidation initiated by the NO_3 radical with phenol, cresol, and furanoic compounds as primary reactants, and is influenced by relative humidity. Another process that has so far been less understood and is currently not treated in modeling studies is the *lensing effect* of BrC, as explored e.g. by Basnet et al. (2023); Cappa et al. (2012). This process can enhance the absorption of BrC. It is based on the mixing state of BrC, typically assuming a core-shell structure. In this structure,

75 the core is composed of black carbon (BC), while the shell, which can consist of BrC or a purely scattering material, acts like a lens. This lens effect focuses and intensifies the light absorption of the entire particle, thereby potentially altering its radiative impact.

Understanding the optical properties of BrC is of fundamental importance, especially its *k* because is a key parameter used to quantify the light-absorbing properties of BrC. However, this parameter is not well constrained, and it exhibits significant

80 uncertainty and variability. Research indicates that the imaginary refractive index of BrC can vary by 30-50%, highlighting the complex and diverse nature of its light-absorbing properties (Wang et al., 2013). Further studies, such as by Cheng et al. (2021), suggest that light-absorption properties of BrC vary depending on the source of emission, as demonstrated in comparisons of BrC generated from different fuels. Saleh (2020) introduced a classification for BrC based on its imaginary refractive index at k_{550} into four categories ranging from very weakly (10^{-4} to 10^{-3}) to strongly absorbing ($> 10^{-1}$) BrC, with a

85 noted correlation between BrC's source and its absorption category. This categorization highlights a gradient in absorption capabilities and associates more absorptive BrC, primarily resulting from high-temperature biomass combustion, with flatter absorption spectra. The classification underscores the complex and variable optical properties of BrC. It should be noted that the absorption categories for OA proposed by Saleh (2020) were based on 20 chamber experiments, which ~~might~~ may not fully reflect the conditions found in the field.

90 A seminal work on modeling the effects of BrC in the atmosphere using 3D atmospheric models was the characterization of OA as absorbing with a k_{550} assigned of 0.27 by Park et al. (2010). Feng et al. (2013) extended this by modeling the absorbing fraction of OA separated into two categories: moderately absorbing, characterized by a k_{550} value of 0.003, and strongly absorbing, with a k_{550} value of 0.03. Lin et al. (2014) continued this approach and classified into two groups: low (k_{550}: 0.001) and high (k_{550}:0.03). This classification, particularly distinguishing primary organic aerosol (POA) from SOA, was based on

95 the understanding that POA generally exhibits greater absorption potential than SOA which is chemically very different. Saleh et al. (2014) advanced the field by deriving equations based on experimental data to parameterize the absorption of OA from the ratio of emitted BC and OA. ~~Such parameterization was subsequently utilized~~ Subsequently, this parameterization was used in the GEOS-Chem model by Saleh et al. (2015) and Wang et al. (2018b), and in the CAM5 model by Brown et al. (2018) to represent OA absorption.

100 At a global scale, studies have highlighted the significant warming effect of BrC alongside BC and greenhouse gases (GHGs). Feng et al. (2013) estimated that BrC's warming effect could be approximately one-fourth that of BC, identifying BrC, mainly emitted from fuel combustion and open vegetation burning, as a substantial component contributing to global warming. Zhang et al. (2020a) suggested that BrC might be a larger heating source in the tropical free troposphere than BC. A recent study by Liu et al. (2023) found that a decrease in single scattering albedo (SSA) at near-ultraviolet wavelengths significantly reduces

105   the efficiency of the direct radiative forcing (DRF) due to strong absorption capabilities of BrC, which impacts both local and global radiation budgets. This is further supported by Wang et al. (2014), who utilized the GEOS-Chem model to demonstrate that incorporating BrC significantly improves the accuracy of absorption aerosol optical depth (AAOD) predictions by over 50% at AERONET stations, contributing an estimated +0.11 Wm^{-2} to DRF.

    Regional studies complement global models by offering detailed insights into BrC formation processes and its effects at a

110 local scale, highlighting the importance of focusing on specific geographical areas to understand local and regional atmospheric phenomena. For example, research conducted in Northwestern and Southeastern Europe and northern peninsular Southeast Asia have revealed significant seasonal variations in BrC concentrations, which are particularly impactful in urban settings often due to residential wood burning (Zhang et al., 2020b; Paraskevopoulou et al., 2023; Methymaki et al., 2023; Pani et al., 2021). These variations not only affect air quality but also complicate the broader understanding of regional climate impacts.

115 ~~Moreover~~In addition, research conducted in the northwestern United States ~~have examined the emissions of BrC~~ has examined the BrC emissions from wildfires. These studies indicate that the inclusion of SOA formation and photobleaching effects in atmospheric models can enhance the simulation of aerosol optical properties. For example, incorporating these processes improves the representation of aerosol optical depth (AOD) and ~~single scattering albedo (SSA)~~SSA, making the model outputs more consistent with observed data (Neyestani and Saleh, 2022). These regional studies underscore the value of localized

120 research in enhancing our understanding of BrC aerosols. They not only ~~provide insights into~~ offer valuable understanding of the specific sources and behaviors of BrC in different environments but also help in refining global models that are used to predict atmospheric conditions. Unlike these studies, which often focus on specific events or short time periods, the current research extends over an entire year, providing a comprehensive analysis of seasonal trends and identifying diverse BrC sources. This approach not only broadens the scope of understanding BrC dynamics, but also enhances the predictive capabilities of

125 climate models concerning BrC's environmental impacts.

    In this research, we aim to investigate the light absorption properties of OA at different environments in Europe. We employ both modeling techniques and experimental approaches to constrain specific k indexes for OA originating from different emission sources, such as fires, residential, shipping, traffic, and others. We use the Multiscale Online Nonhydrostatic Atmosphere Chemistry model (MONARCH; Badia and Jorba, 2015; Badia et al., 2017; Klose et al., 2021; Navarro-Barboza et al., 2024) to

130 simulate the light absorption of OA in Europe during 2018. Our results provide an estimate of OA light absorbing properties in Europe. This comprehensive approach allows us to provide a first attempt to constrain OA optical properties representative of field conditions based on the current knowledge on emission sources and transport modeling. ~~While~~ Although previous extensive studies in laboratory conditions such as Saleh (2020) are highly valuable for modeling purposes, they may not fully represent the actual ambient conditions.

135   In Section 2, we detail the experimental framework and the methodologies employed in this research. The observational dataset is introduced and the modeling tools and optimization method to derive k values described. Section 3 presents our results, starting with an evaluation of the modeled OA mass against observational data and providing an in-depth analysis of source contributions. We ~~discuss then~~ then discuss the optimization of k values under different assumptions for OA emission sources. Finally, Section 4 summarizes our key conclusions and outlines the recommendations arising from this study.

2 Materials and Methods

2.1 Observational dataset

The OA/Organic Carbon (OC) mass concentrations and multi-wavelengths absorption measurements used in this study were collected at 12 sites in Europe covering urban, suburban, and regional background environments. Figure 1 and Table 1 show the geographical locations of these atmospheric research stations. Figure 1 also shows the relative contribution of black carbon

(BC) and BrC to the total absorption measured at 370 nm that was obtained applying the procedure detailed in Section 2.1.1.
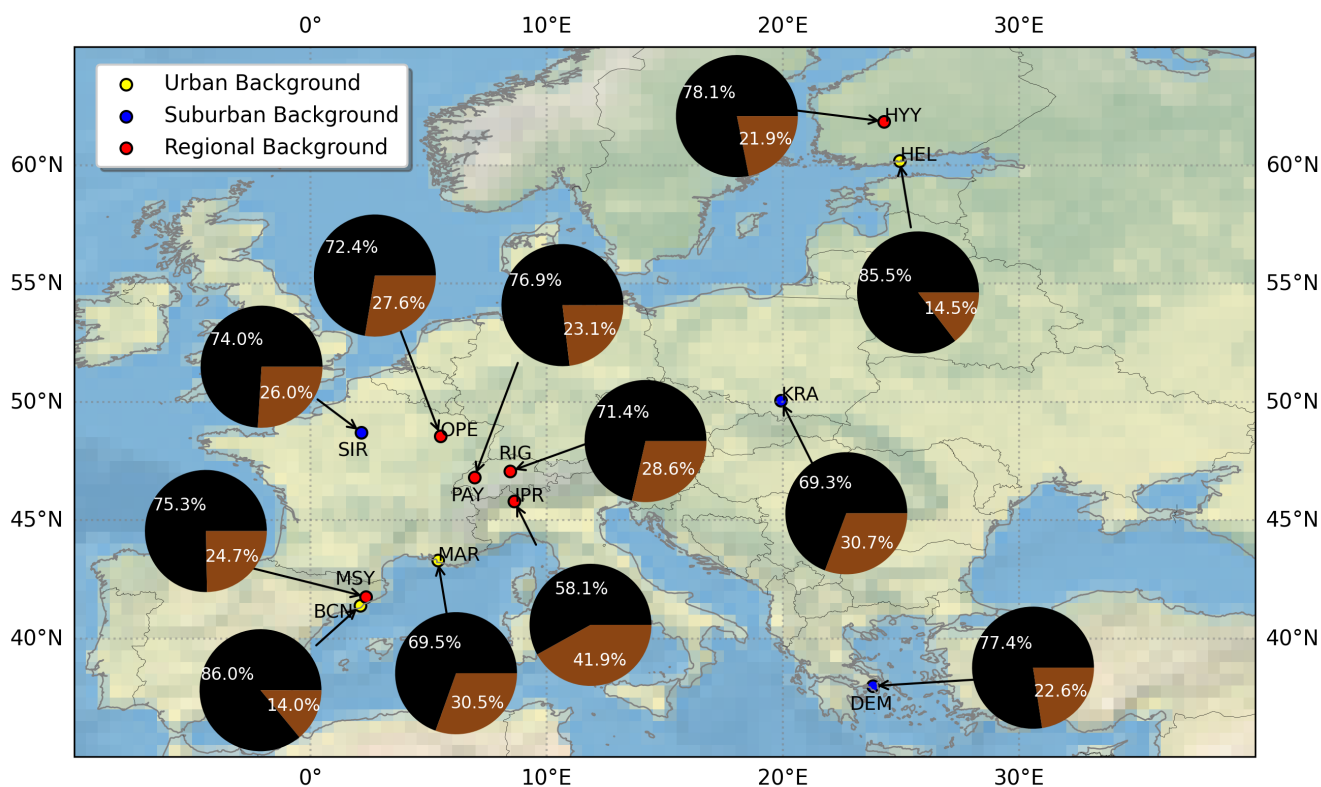
Figure 1. Annual average contributions [%] of BrC (~~orange~~brown) and BC (~~gray~~black) to the total absorption at 370 nm, measured at twelve different monitoring stations across Europe in 2018. ~~The location of each station is indicated~~ Station locations are marked by ~~a~~ colored ~~dot, categorized by the station classification~~dots: urban background (yellow), suburban background (blue), and regional background (red)~~environments. The~~ Station acronyms ~~used for the stations in the figure~~ are ~~explained~~ listed in ~~the~~ Table 1.

Data from these measurement sites were collected from different infrastructures/projects as EBAS (https://ebas.nilu.no/), RI-URBANS Project (Savadkoohi et al., 2023, https://riurbans.eu/), COLOSSAL COST Action (Chen et al., 2022, https://www.cost.eu/actions/CA16109/), and the FOCI Project (https://www.project-foci.eu/wp/). At some sites (Table 1), OA mass concentrations were directly provided by Aerosol Chemical Speciation Monitor (ACSM) instruments with 30 minute time res-

150   olution (Chen et al., 2022), while OC mass concentrations were obtained from the analysis of 24h filters by means of thermal-optical off line technique (SUNSET Instruments) following the EUSAAR II Protocol (Cavalli et al., 2010). Details about ACSM instruments used for OA determination, measurement principle~~and accuracy of these instruments~~, accuracy and treatment of sources of error as collection efficiency can be found in ~~Chen et al. (2022)~~Ng et al. (2011), Middlebrook et al. (2012), Fröhlich et al. (2013), ~~and Ng et al. (2011)~~Freney et al. (2019) and Chen et al. (2022). At sites where OC mass concentrations from

155   24h filters were available (Table 1), specific organic-aerosol-to-organic-carbon (OA/OC) ratios were applied depending on the characteristic of the measurement sites. A factor of 1.4 is traditionally used, although some studies support larger values (e.g., Zhang et al., 2005). Here, we applied OA/OC ratios of 1.8 at urban sites and 2.1 at regional/remote sites. These values agreed with some estimations reported in literature. For example, Minguillón et al. (2011) reported OA/OC ratios of 2.0 and 1.6 for the regional background, MSY, and urban background BCN sites, respectively. Similarly, Daellenbach et al. (2016) and Favez

160   et al. (2010) documented OA/OC ratios of 1.84 and 1.8 at two urban background sites in Switzerland and France, respectively.

      Aerosol particles light absorption coefficients was derived at 7 different wavelengths (370, 470, 520, 590, 660, 880, and 950 nm) with 1h time resolution using AE33/AE31 Aethalometers (Magee Scientific) instruments. An extensive description of the AE33 and AE31 instruments is provided for example by Drinovec et al. (2015, 2017) and Backman et al. (2017), respectively. Briefly, the Aethalometers measure the attenuation of light by aerosol particles collected onto a fiber filter tape converting the

165   measured attenuation into absorption.

Table 1. Monitoring stations used in this study

Station	Acronym	Country	Station Type	Variable/ Instrument	Cut-off size Mass/Abs	Time/ Resolution	Latitude	Longitude
SMEAR II Hyytiala[*]	HYY	Finland	RB	OA/ACSM[a] Abs/AE33[b]	PM_{10}/ PM_{10}	30 min, 1h	61°51'0.00" N	24°17'0.00" E
Helsinki[*]	HEL	Finland	UB	OA/ACSM[a] Abs/AE33[b]	PM_1/ PM_1	30 min, 1h	60°11'47.11"N	24°57'1.31"E
Krakow[*]	KRA	Poland	SUB	OA/ACSM[a] Abs/AE33[b]	PM_1/ $PM_{2.5}$	30 min, 1h	50°3'56.00" N	19°54'56.00" E
Sirta[***]	SIR	France	SUB	OA/ACSM[a] Abs/AE33[b]	$PM_{2.5}$/ PM_1	30 min, 1h	48°42'36.00" N	2°9'36.00" E
Observatoire Perenne de l'Environnement[**]	OPE	France	RB	OC/SUNSET[c] Abs/AE31[d]	$PM_{2.5}$/ PM_{10}	24h, 1h	48°33'44.00" N	5°30'20.00" E
Rigi[**]	RIG	Switzerland	RB	OC/SUNSET[c] Abs/AE33[b]	$PM_{2.5}$/ $PM_{2.5}$	24h, 1h	47°4'3.00" N	8°27'50.00" E
Payerne[**]	PAY	Switzerland	RB	OC/SUNSET[c] Abs/AE33[b]	$PM_{2.5}$/ PM_{10}	24h, 1h	46°48'47.00" N	6°56'41.00" E
Ispra[**]	IPR	Italy	RB	OC/SUNSET[c] Abs/AE31[d]	$PM_{2.5}$/ PM_{10}	24h, 1h	45°49'N	8°38'E
Marseille[*]	MAR	France	UB	OA/ACSM[a] Abs/AE33[b]	PM_1/ $PM_{2.5}$	30 min, 1h	43°18'19.1"N	43°18'19.1"E
Montseny[**]	MSY	Spain	RB	OC/SUNSET[c] Abs/AE33[b]	PM_{10}/ PM_{10}	24h, 1h	41°46'45.63" N	02°21'28.92" E
Barcelona[*]	BCN	Spain	UB	OA/ACSM[a] Abs/AE33[b]	PM_{10}/ PM_{10}	30 min, 1h	41° 23' 14" N	2° 06' 56"E
Demokritos Athens[*]	DEM	Greece	SUB	OA/ACSM[a] Abs/AE33[b]	$PM_{2.5}$/ PM_{10}	30 min, 1h	37°59'24.00" N	23°49'12.00" E

[*] Project/Source: RI-URBANS/FOCI/COLOSSAL (Savadkoohi et al., 2023; Chen et al., 2022)

[**] EBAS (https://ebas.nilu.no/)

[***] RI-URBANS/FOCI/EBAS (Savadkoohi et al. (2023); https://ebas.nilu.no/)

[a] OA/ACSM: Organic aerosol/Aerosol Chemical Speciation Monitor

[b] Abs/AE33: Total absorption (370-950 nm)/Aethalometer AE33 model

[c] OC/SUNSET: Organic Carbon/OCEC Carbon Aerosol Analyzer

[d] Abs/AE31: Total absorption (370-950 nm)/Aethalometer AE31 model

2.1.1 BrC absorption from aethalometer data

Most of the filter-based absorption techniques that determine the absorption coefficients from the measurements of light passing through an aerosol-laden filter (as the aethalometers), suffer from various systematic errors that need to be corrected. These artifacts include the enhancement of the measured attenuation due to multiple scattering of light by the filter fibers, a further enhancement of light attenuation due to the scattering of aerosols embedded in the filter and a progressive saturation of the instrumental response due to the accumulation of the sample in the filter matrix (e.g., Bond et al., 1999; Weingartner et al., 2003; Moosmüller et al., 2009; Drinovec et al., 2015, 2017; Müller and Fiebig, 2018; Yus-Díez et al., 2021). Thus, absorption data

from aethalometer instruments need to be harmonized to ~~take into~~ account for these artifacts. All AE33 data were harmonized as described in Savadkoohi et al. (2023). AE31 data were taken from EBAS Level 2 quality assured/quality checked (QA/QC) dataset and were directly downloaded from the EBAS database (EBAS, https://ebas-data.nilu.no/). These data were processed following the ACTRIS recommendations for the reporting of absorption (Müller and Fiebig, 2018), ensuring the comparability of absorption measurements across the sites by employing harmonized measurement protocols.

The contribution of brown carbon (BrC; $b_{\mathrm{abs},BrC}(\lambda)$) to the total measured absorption ($b_{\mathrm{abs}}(\lambda)$) at different wavelengths from 370 nm to 660 nm was estimated by subtracting the absorption due to BC (BC; $b_{\mathrm{abs},BC}(\lambda)$ to the measured ($b_{\mathrm{abs}}(\lambda)$):

$$b_{\mathrm{abs},BC}(\lambda) = b_{\mathrm{abs}}(880\mathrm{nm}) \cdot \left(\frac{\lambda}{880\mathrm{nm}}\right)^{-AAE_{BC}} \tag{1}$$

$$b_{\mathrm{abs},BrC}(\lambda) = b_{\mathrm{abs}}(\lambda) - b_{\mathrm{abs},BC}(\lambda) \tag{2}$$

where AAE_{BC} is the Absorption Angstrom Exponent (AAE) of BC, which allows for the calculation of $b_{\mathrm{abs},BC}(\lambda)$ (in units of Mm^{-1}) from the measurements of $b_{\mathrm{abs},BC}(\lambda)$ at 880 nm assuming that BrC does not absorb at 880 nm (e.g., Qin et al., 2018). ~~The main~~ It should be noted, however, that recent studies have shown the existence of specific dark BrC components in biomass-burning (BB) smoke (tar balls or tar BrC) that can absorb radiation also in the near-infrared (e.g. Chakrabarty et al. (2010); Hoffer et al. (2016, 2017); Chakrabarty et al. (2023); Mathai et al. (2023)). Thus, a contribution to near-IR absorption from possible presence of dark BrC cannot be ruled and would lead to an underestimation of the BrC absorption reported here. However, the dark BrC contribution to absorption at 880 nm is expected to be smaller compared to that of BC. For example, Hoffer et al. (2017) reported that the absorption coefficient at 880 nm of dark BrC produced in a laboratory was 10% of that at 470 nm and, consequently, even lower compared to that at 370 nm. Similarly, Cuesta-Mosquera et al. (2023) estimated a contribution of BrC to absorption at 880 nm of 3% in a rural area in central Europe strongly affected by residential wood burning emissions in Winter. Given the complexity of these specific BrC components, the imaginary refractive index (k) of tar balls generated in laboratory experiments vary over a wide range of values depending on the specific type of fuel (wood) burned and the different analytical method employed. For example, Mathai et al. (2023) reported k values at 550 nm of tar balls measured in ambient BB plumes 10 times lower than the values reported by Hoffer et al. (2016), Chakrabarty et al. (2010) or Saleh et al. (2018); Saleh (2020) for laboratory generated particles. Also, Mathai et al. (2023) highlighted that even though Hoffer et al. (2016) and Chakrabarty et al. (2010) used similar methods, their k was at least 10 times different. Thus, due to poorly characterized optical properties, the impact of tar BrC on IR absorption at ambient conditions is still uncertain. Consequently, we follow here the common practice of considering ambient BC as the dominant absorber at 880 nm (e.g. Kirchstetter et al. (2004); Massabò et al. (2015); Liakakou et al. (2020); Zhang et al. (2020b); Yus-Díez et al. (2022)).

One important source of uncertainty in equations 1 and 2 is the AAE assumed for BC. In many studies a value of 1 was used (Liakakou et al., 2020; Tian et al., 2023; Cuesta-Mosquera et al., 2023, e.g.,). However, theoretical simulations have shown that the AAE_{BC} can reasonably vary between 0.9 and 1.1 depending on the size and internal mixing of BC particles (Bond et al., 2013; Lu et al., 2015, e.g.,). Here we estimated the site dependent AAE_{BC} as the first percentile of the AAE frequency distribution. The AAE can be calculated from multi-wavelengths (370, 470, 520, 590, 660, 880, and 950 nm) total absorption

measurements as the linear fit in a log-log plot of the total absorption versus the measuring wavelengths. The effect of BrC absorption is to increase the AAE and, consequently, the first percentile of AAE represents conditions where the absorption is dominated by BC. In order to reduce the noise, the 1st percentile at each site was calculated from AAE values obtained from fit with $R^2 > 0.99$ ~~(Tobler et al., 2021)~~(Tobler et al., 2021; Glojek et al., 2024). Other approaches used a combination of Mie theory and experimental data to explore the wavelength dependence of AAE_{BC} and proposed an estimation of $b_{abs,BrC(\lambda)}$ based on the ratio between the AAE calculated from 370 to 520 nm and from 520 to 880 nm (Wang et al., 2018a; Li et al., 2019). However, this methodology assumed that BrC particles do not absorb at 520 nm whereas it has been shown that the contribution of BrC to absorption at this wavelength can be high (e.g. Cuesta-Mosquera et al. (2023)). As a consequence, other studies (e.g. Zhang et al. (2019); Luo et al. (2022)) used the AAE calculated from 880 to 950 nm to calculate the AAE_{BC} assuming that BrC particles do not absorb in the near IR. Nevertheless, the latter methodology may suffer from additional uncertainties related to the possible low aethalometer signal at 950 nm, frequently observed especially at remote sites. Thus, it should be considered that the methodologies proposed to estimate AAE_{BC}, including the use of the 1st percentile applied here, are prone to uncertainties. On the other hand, Zhang et al. (2020b) have reported an uncertainty of approximately 11% in the estimation of the $b_{Abs,BrC(370)}$ contribution to $b_{Abs,370}$ when using different AAE values ranging from 0.9 and 1.1. For sites included here, the 1st percentile method provide AAE_{BC} values ranging from 0.928 to 1.088 confirming that this experimental method can provide reasonable estimations of the AAE_{BC}. It should be noted that mineral dust particles from North African deserts can absorb at 880 nm even if much less efficiently compared to BC. We assumed that the effect of dust at the surface was present mostly in Mediterranean sites (as BCN, MSY and DEM) due to their proximity to dust source emission (as North African deserts). The measurements possibly affected by dust absorption were removed from the datasets of the above three sites. In the case of BCN and MSY, dusty days were detected using the methodology that has been officially accepted by the European Commission for reporting on natural contributions to ambient PM levels over Europe (European Commission, 2011). At DEM, dusty days were detected and removed using the scattering Angstrom exponent (SAE) from in-situ surface nephelometer measurements available in the EBAS database (www.ebas.nilu.no) assuming that SAE values lower than one indicate the presence of dust particles in the atmosphere (e.g. Valenzuela et al. (2015)).

Figure 1 shows the average annual contributions of BC and BrC to the total absorption measured at 370 nm at twelve European stations, identified by color-coded markers indicating their background settings: yellow for urban, blue for suburban ~~,~~ and red for regional areas. ~~Urban sites, which are BCN, HEL and MAR, report a contribution rangefrom~~ Here we report the BrC absorption at 370 nm given that the BrC absorption efficiency is the highest in the UV spectral range, and consequently, the observed BrC absorption is less uncertain compared to the visible range. A low BrC contribution, around 14%~~to~~, was observed at the urban sites of BCN and HEL, both affected by direct traffic emissions, making BC the dominant absorber at these sites (Okuljar et al., 2023; Via et al., 2021). MAR urban site registered higher BrC contribution (30~~% of BrC, reflecting the significant influence of combustion processes within the cities, with MAR showing a notably high BrC percentage, most probably due to industrial activities and emissions from the port~~%) likely reflecting the accumulation of biomass burning emissions in winter and the presence of BrC sources as shipping emissions (Corbin et al., 2018; Chazeau et al., 2022). Subur-

240 ban stations, including SIR, KRA, and DEM, exhibit BrC ~~proportions~~ contributions from 22% to 30%, reflecting a blend of local urban emissions and regional influences such as biomass burning ~~.~~

and coal combustion. KRA is considered a pollution hotspot in Europe (e.g. Casotto et al. (2023)) with high consumption of coal and wood (both important sources of BrC) for energy production and residential heating, making the OA concentrations measured in KRA the highest among the European measuring sites included in Chen et al. (2022). DEM and SIR are affected by

245 biomass burning emissions especially in winter, which causes a considerable accumulation of BrC during the cold season (see, e.g., Liakakou et al. (2020); Zhang et al. (2020a); Savadkoohi et al. (2023)). Regional stations, represented by HYY, OPE, RIG, PAY, IPR, and MSY, display BrC ~~levels~~ contributions from 21% to 41%. These percentages indicate a ~~mix~~ mixture of biogenic sources, local emissions, agricultural activities, and ~~trans-boundary pollution affecting~~ transboundary pollution that affects the regional atmosphere. IPR stands out with the highest contribution ~~, suggesting~~ (around 40%), suggesting a significant contribu-

250 tion of ~~low temperature combustion processes~~ low-temperature combustion processes as residential sources (e.g. ~~, residential sources).~~

Putaud et al. (2018)). Overall, although BC typically represents the most absorbing aerosols component at these stations (usually > 70%), it is noteworthy that BrC could contribute comparably to absorption in some instances.

2.2 Model description

2.2.1 The MONARCH atmospheric chemistry model

255 The MONARCH model (Jorba et al., 2012; Badia and Jorba, 2015; Badia et al., 2017; Klose et al., 2021) consists of advanced chemistry and aerosol packages coupled online with the Nonhydrostatic Multiscale Model on the B-grid (NMMB; Janjic et al., 2001; Janjic and Gall, 2012). The model allows running both global and regional simulations with telescoping nests. Multiple choices of gas- and aerosol chemistry schemes can be selected in the model. Here, we briefly describe the configuration adopted

260 in this work.

The gas-phase chemistry solves the Carbon Bond 2005 chemical mechanism (CB05; Yarwood et al., 2005) extended with chlorine chemistry (Sarwar et al., 2012). The CB05 is well formulated for urban to remote tropospheric conditions, and it uses photolysis rates computed with the Fast-J scheme (Wild et al., 2000) considering the physics of each model layer (e.g., clouds, absorbers such as ozone). A mass-based aerosol module describes the life cycle of dust, sea salt, BC, OA (both primary and

265 secondary), sulfate, ammonium and nitrate aerosol components (Spada, 2015). A sectional approach is used for dust and sea salt, while the other aerosol species are represented by a fine mode, except nitrate which is extended with a coarse mode to consider the condensation of nitric acid on coarse particles. Sulfate production considers the gas-phase oxidation of both sulfur dioxide (SO_2) and dimethyl sulfide, and the aqueous chemistry of SO_2. The heterogeneous hydrolysis of N_2O_5 contributes to the production of nitric acid using the parameterization of Riemer et al. (2003). A thermodynamic equilibrium model (Metzger

270 et al., 2002) solves the partitioning of semivolatile inorganic aerosol components in the fine mode, and an irreversible uptake reaction accounts for the production of coarse nitrate in dust and sea salt (Hanisch and Crowley, 2001; Tolocka et al., 2004). Different meteorology-driven emissions are computed online in MONARCH (i.e., mineral dust, sea salt, and biogenic gas

species). The mineral dust scheme of the model is described in detail in Pérez et al. (2011) and Klose et al. (2021). Sea salt emissions are calculated following the source function of Jaeglé et al. (2011) as described in Spada et al. (2013), while biogenic

275 Non-Methane Volatile Organic Compounds (NMVOC) and soil NO emissions are estimated with the Model of Emissions of Gases and Aerosols from Nature (MEGAN) v2.04 model (Guenther et al., 2006).

Black carbon is represented in MONARCH following Chin et al. (2002). Two primary hydrophobic/hydrophilic modes are defined with an aging process converting mass from the hydrophobic to the hydrophilic mode with a lifetime of 1.2 days. Primary emissions are assumed to be emitted as 80% hydrophobic.

280 The simple scheme proposed in Pai et al. (2020) is adopted to model OA. It is computationally efficient and reproduces well the organic mass assuming fixed SOA yields adjusted to match results from the more complex volatility-based scheme approach. Here, we briefly describe the scheme. Primary organic carbon (OC) emissions are emitted as 50% hydrophobic species with an and 50% hydrophilic species. An OA/OC ratio of 1.4 is adopted for the hydrophobic component, while the hydrophilic oxygenated component one assumes an OA/OC ratio of 2.1 to convert OC to OA mass transported in the model.

285 Similarly to BC, an atmospheric aging of hydrophobic to hydrophilic primary species is simulated with a conversion lifetime of 1.15 days. In our implementation, no marine primary organic aerosol is considered. The scheme includes sources of SOA precursors from biogenic, pyrogenic, and anthropogenic origin with fixed SOA yields. Biogenic sources of SOA uses a 3% yield for isoprene and 10% yield for both monoterpenes and sesquiterpenes. A 50% of biogenic SOA is emitted directly to account for the near-field formation of SOA. On the other hand, precursors from combustion emissions are scaled from CO

290 emissions as a proxy, of which 1.3% come from fires and biofuels (combustion sources) and 6.9% from fossil fuels. The gas-phase SOA products converts to the aerosol phase based on a first-order rate constant with a lifetime of 1 day.

2.2.2   Integration of Brown Carbon in MONARCH

We have advanced the MONARCH code by implementing a representation of BrC and emission sources derived from biomass burning (BB) and Biofuel (BF) emissions following Saleh et al. (2014). The absorptivity of OA in BB and BF emissions can
295 be effectively parameterized as a function of the ratio of BC-to-OA. Based on this, the imaginary refractive index of OA (effective absorptivity; k_{OA}) (eq. **??**) is parameterized across various fuel types and burn conditions using the BC-to-OA ratio of emissions.

$$k_{OA,550} = 0.016 \log_{10}\left(\frac{E_{BC}}{E_{OA}}\right) + 0.03925,$$

where $k_{OA,550}$ denotes the OA absorptivity at the wavelength of 550 nm. Here, E_{BC} and E_{OA} are the emission rates of
300 BC and OA, respectively, in $g\,m^{-2}\,s^{-1}$. This formulation allows for the computation of $k_{OA,550}$ as an intermediate step in calculating BrC emissions. Then, the methodology of Liu et al. (2013) is adopted to scale the BrC emissions in the model:

$$E_{BrC} = \frac{4\pi k_{OA,550} \cdot E_{OA}}{\rho \cdot 550\text{nm} \cdot MAE_{BrC}(550\text{nm})}$$

where ρ represents the density of the particle in $g\,m^{-3}$, E_{BrC} indicates the BrC emission rate in $g\,m^{-2}\,s^{-1}$, and $MAE_{BrC}(550\text{nm})$ is the mass absorption efficiency of BrC.

In addition, we implemented the "photobleaching effect" to account for the aging process of BrC particles, as photobleaching significantly changes their absorption properties. Forrister et al. (2015) has shown that 6% of the emitted BrC of BB and BF resist bleaching, while in Wang et al. (2018b); Neyestani and Saleh (2022) 25% of all BrC emissions are considered unchanged. Wong et al. (2019) found that up to 20% of BrC does not lose its light-absorbing properties, suggesting a minimum threshold for BrC light absorption that could be attributed to refractory and relatively inert BrC associated with macromolecules. In our simulation, we assume an intermediate value where 8% of BrC retains its hydrophobic properties, while the rest transitions to a hydrophilic state and possibly loses its absorption properties.

The modeling strategy applied by Zhang et al. (2020a) considers different photobleaching effects for BrC based on its sources. For BB and BF BrC sources, the model adopts the framework used by Forrister et al. (2015), while photobleaching of aromatic SOA is represented according to the method described by Liu et al. (2016). These approaches are based on the principle that BrC absorption decreases with increasing concentration of hydroxyl radicals (OH), as shown in the following equation:

$$k_{BrC\,t+\Delta t} = k_{BrC\,t} \cdot \exp\left(-\frac{[\text{OH}]\cdot \Delta t}{5\times 10^5}\right)$$

where $k_{BrC\,t}$ and $k_{BrC,t+\Delta t}$ denote the absorption at the model integration time t and $t+\Delta t$. The constant 5×10^5 $mol\,cm^{-3}$ is used to represent the typical OH concentration in the atmosphere during the day, based on the study by Wang et al. (2016). In our model, this photobleaching equation is applied to 92% of the BrC emissions, as stated above, reflecting the proportion that is susceptible to this process. We only account for BrC sources from BB and BF, neglecting secondary production of BrC as it is currently a highly uncertain process.

2.2.2 Optical properties

We use an offline optical package (Obiso, 2018) to calculate the absorption by OA using the mass concentration simulated by the model. The package allows calculating intensive optical properties of a size-distributed particle ensemble, including the absorption efficiency (Q_a) as the difference between extinction and scattering efficiencies (Mishchenko et al., 2002). The required input physical properties of the aerosols are the size distribution, the complex refractive index, the particle shape and the hygroscopicity. Our package only uses the log-normal size distribution, that is defined by two parameters: the geometric radius (r_g) and the standard deviation (σ_g). The real (n) and imaginary (k) parts of the complex refractive index determine the scattering and absorption properties of the particles, respectively, and primarily depend on their internal composition. The spherical shape is assumed by default in the package while the water uptake of the hydrophilic modes is taken into account through a grid of hygroscopic growth factors (α) defined for specific values of relative humidity (RH). The assumption of external mixture is adopted in the calculation of the absorption by OA.

The package is built on a data set of monodisperse single-wavelength optical properties, pre-calculated using the Mie-theory code by Mishchenko et al. (2002), whose structure allows computational efficiency while preserving application flexibility. In general, the optical properties of a single particle depend on the ratio of its size to the incident wavelength, rather than on those two quantities separately (Mishchenko et al., 2002). For this reason, the data set is calculated on a grid of size parameters ($x = 2\pi r/\lambda$, where r and λ are the particle radius and the incident wavelength, respectively) ranging from 0.011 to ~ 1000. Following Gasteiger and Wiegner (2018), we apply an increment of 1% to each grid value x_i to obtain the next one; moreover, we store the optical properties integrated in very narrow size bins centered in each x_i and ranging from $x_i/\sqrt{1.01}$ to $x_i\sqrt{1.01}$. The entire set of size parameters is then considered for a grid of real indexes (ranging from 1.3 to 2, with a step of 0.05) and imaginary indexes (from 0 to 1, with varying resolution across different orders of magnitudes).

The physical properties of OA used in this work, that align with the model aerosol representation, are presented in Table 2. Size distribution and standard refractive indexes are taken from the Optical Properties of Aerosols and Clouds (OPAC) database (Hess et al., 1998). The hygroscopic growth factors for seven prescribed RH values are from Chin et al. (2002). Once defined the working wavelength of 370 nm, which allows mapping the size parameters onto particle radii, the needed pre-calculated optical efficiencies are integrated over the input size distribution. Then, the actual extinction and scattering efficiencies corresponding to the input refractive index are obtained by means of bilinear interpolation from the integrated values at the four closest gridded refractive indexes. The water uptake affects both the input size distribution and refractive index of the hydrophilic modes of OA. Once read a specific RH level calculated by the model, the corresponding hygroscopic growth factor is set by linearly interpolating between the closest gridded values and subsequently applied to the geometric radius of the size distribution (as well as to the extremes of the size integration): $r_{g,w} = \alpha r_g$. The refractive index of the wet particles is obtained as the volume-weighted mean of the refractive index of the dry particles and that of water (the latter taken from Segelstein, 1981).

Once obtained the size-integrated absorption efficiency, the absorption coefficient of OA is calculated as follows:

$$b_a = \frac{3Q_{a,w}\alpha^3}{4\rho r_{e,w}} M \tag{3}$$

where $Q_{a,w}$ is the wet absorption efficiency, α^3 is the wet-to-dry mean volume ratio, ρ is the mass density of the dry particles (Table 2), $r_{e,w}$ is the wet effective radius (defined as the projected-surface-weighted mean radius) and M is the mass concentration of OA from the model. Note that the wet quantities only refer to the hydrophilic OA modes and tend towards the corresponding dry quantities for the hydrophobic mode (for which $\alpha = 1$).

Table 2. ~~Physical~~ Microphysical properties of the ~~organic aerosol~~ OA species implemented in the MONARCH model and used in this work for optical calculations (Spada, 2015; Chin et al., 2002; Hess et al., 1998): geometric radius (r_g), standard deviation (σ_g) and effective radius (r_e) of the size distribution, real (n) and imaginary (k) refractive indexes, mass density (ρ) and hygroscopic growth factor (α). In the second column, *phob* stands for "hydrophobic mode" and *phil* for "hydrophilic mode". The range extremes used for size integration (r_1–r_2) are reported within parentheses close to the corresponding r_e values. The seven values for α apply to the hydrophilic modes and are relative to RH levels of 0%, 50%, 70%, 80%, 90%, 95% and 99%. The refractive indexes reported are relative to a wavelength of 550 nm.

Parameters	Modes	Organic Aerosol
r_g (μm)	*phob-phil*	$2.12 \cdot 10^{-2}$
σ_g	*phob-phil*	2.2
r_e (μm)	*phob-phil*	$1.003 \cdot 10^{-1}$ (0.005–20)
n	*phob-phil*	1.53
k	*phob-phil*	$6.0 \cdot 10^{-3}$ to > 0.1
ρ (g cm^{-3})	*phob-phil*	1.8
α	*phob*	1.0
	phil	(1.0, 1.2, 1.4, 1.5, 1.6, 1.8, 2.2)

2.2.3 Emissions

The High-Elective Resolution Modelling Emission System version 3 (HERMESv3; Guevara et al., 2019, 2020) is used to provide anthropogenic, biomass burning, and ocean emissions to be used as input in the MONARCH model. In this study, we employ the global-regional module (HERMESv3_GR; Guevara et al., 2019), which allows users to flexibly combine gridded global and regional emission inventories. In addition, this module facilitates the application of country-specific scaling factors and masks. HERMESv3 disaggregates the original datasets both spatially and temporally, and applies user-defined speciated emissions.

In this study, we used the European-scale emission inventory CAMS-REG-AP_v4.2 (Kuenen et al., 2022), developed under the Copernicus Atmosphere Monitoring Service (CAMS). Within this framework, the CAMS-REG-AP_v4.2_REF2 represents a specific dataset or version of the CAMS-REG-AP_v4.2 inventory, which adopts a harmonized approach for consistently including the condensable fraction for the residential wood combustion (RWC) particulate matter emissions. This is important to address the previously identified inconsistencies across European inventories, as highlighted by Denier Van Der Gon et al. (2015), which mainly stem from variable emission factors used by different countries accounting or not for condensables impacting modeling results (e.g., Navarro-Barboza et al., 2024). To accurately quantify biomass burning (BB) emissions, our study utilized data from the Global Fire Assimilation System version 1.2 (GFASv1.2) analysis. This dataset provides detailed emission fluxes derived from satellite information for various sources such as forest, grassland, and agricultural waste fires (Kaiser et al., 2012). Additionally, for oceanic dimethyl sulfide (DMS) emissions, we relied on the CAMS Global Ocean dataset ~~(Lana et al., 2011; Granier et al., 2019)~~(Lana et al., 2011; Granier et al., 2019).

2.3 Model simulations

380 ~~In this study, we~~ We used the MONARCH model with a domain that covers the European continent and part of North Africa at a horizontal resolution of ~ 20 km, as shown in Figure 2. Perturbation runs (commonly know as the brute force method) were conducted to apportion the contribution from fires, traffic, shipping, residential, and other sources. Biomass burning emissions derived from the GFASv1.2 product are tagged (GFAS) as one of the main contributors to OA absorption. Traffic emissions (TRAF) categorized under sectors GNFR_F1, F2, F3, and F4 account for exhaust and non-exhaust emissions of gasoline,
385 diesel and liquefied petroleum gas vehicles. Shipping emissions (SHIP) are derived from GNFR_D sector. The emissions from commercial, institutional and residential sources (RESI) consider a wide range of sources related to buildings and facilities and are categorized under sector GNFR_C. RESI includes activities of combustion in different types of devices, including boilers, turbines, engines, and chimneys, for different fuel types (i.e., natural gas, wood, fuel oil, LPG, coal). In this sector, only combustion activities related to space heating, cooking, and water heating are included (cleaning activities are not considered).
390 Furthermore, the rest of sources are tagged together as other sources (OTHR) including public power, industry, fugitives, solvents, aviation, offroad, waste, agriculture, and biogenic emissions.
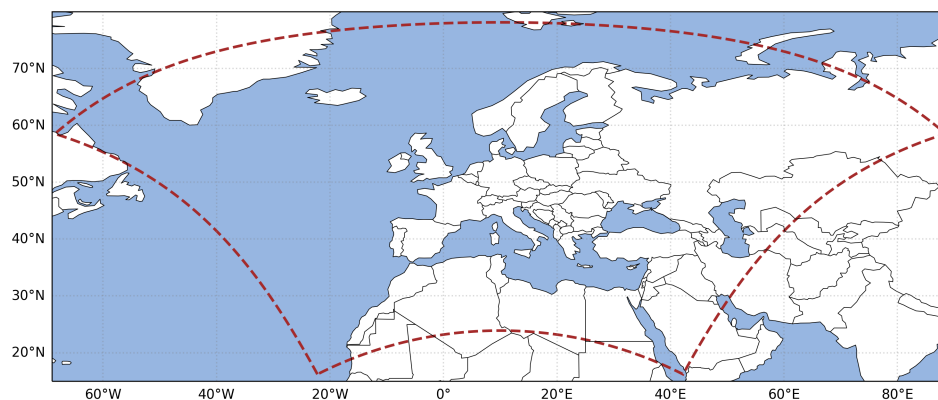

Figure 2. Model domain at ~ 20 km of horizontal resolution.

The model ran with 24 vertical layers and a top of the atmosphere set at 50 hPa. Meteorology initial and boundary conditions were obtained from the ECMWF global model at $0.125°$, and the chemical boundary conditions from the CAMS global system at $0.45°$ (Flemming et al., 2015). ~~Emissions~~ The emissions were processed as described in Section 2.2.3. The atmospheric
395 meteorological variables are initialized every 24h to keep the modeled circulation close to observations, while the chemistry initial conditions are those prognostically estimated by MONARCH (i.e., every day the model uses as an initial state for these variables their modeled value at 24 UTC of the day before). A spin-up period of 15 days is used to derive the chemistry initial conditions for 2018.

For efficient execution of the MONARCH modeling chain, we utilized the autosubmit workflow manager, a tool proven
400 effective in such complex modeling simulations (Manubens-Gil et al., 2016).

16

2.4   Off-line Refractive index optimization

Since k is a highly uncertain parameter with a strong dependence on the sources of OA, we employed a method to derive an optimized k for each OA component (aggregating both primary and secondary contribution) that combines the results of the perturbation runs, which provides source apportionment of OA mass, and observations described in Section 2.1.

Based on the aerosol mass calculated by the model, we use the offline optical tool described in Section 2.2.2 to derive k values that minimize the error with the absorption measured at the 12 monitoring stations across Europe (see Figure 1Figure S1 illustrates the steps of the optimization process). The optimized k values are derived using the SLSQP algorithm (Sequential Least Squares Programming), which is particularly well-suited for nonlinear objective functions and constraints to minimize a cost function. This process handles the task of minimizing the error between the modeled and the observed absorption. The cost function calculated here evaluates this error at each time step, guided by predefined boundary conditions bounds for k values obtained derived from Saleh (2020). These conditions categorize OA absorption into four optical classes: very weakly absorptive OA (VW-OA), weakly absorptive OA (W-OA), moderately absorptive OA (M-OA), and strongly absorptive OA (S-OA). The relation between OA absorbing categories and OA sources is described in Section 2.5Note that Saleh (2020) categories for OA absorption were derived from 20 chamber experiments that may not be completely representative of ambient conditions in the field. Regarding the constraints used in the SLSQP algorithm, we have applied the condition which is based on extensive experimental and modeling results, e.g., (Andreae et al., 1998; Bond et al., 2013; Laskin et al., 2015; Saleh, 2020), suggesting that OA from fires exhibit the highest k values. The resulting k values are representative of OA in environmental conditions, which may include interactions with other species, providing an empirical range of k values that account for various OA sources and potential interference.

For the computation of k at 370 nm within the optimization module, we adopt the equation described in Saleh (2020), which describes the wavelength dependency of k for BrC:

$$k(\lambda) = k_{550} \times \left(\frac{550}{\lambda} \right)^{w} \tag{4}$$

where k_{550} represents the imaginary refractive index (k) at 550 nm, λ is the wavelength in nm, and w denotes the wavelength dependence. The values of w and k_{550} for each OA class (VW-OA, W-OA, M-OA, and S-OA) were determined based on Table 1 in Saleh (2020).

Regarding the constraints used in the SLSQP algorithm, we have applied the condition which is based on extensive experimental and modeling results e.g., (Andreae et al., 1998; Bond et al., 2013; Laskin et al., 2015; Saleh, 2020), suggesting that OA from fires exhibit the highest k values.

Figure ?? illustrates the steps of the optimization process. The procedure starts with the tagging of OA per source derived from MONARCH runs, followed by the application of a priori k values imposed based on Saleh (2020). Note that Saleh (2020) categories for OA absorption were derived from 20 chamber experiments that may not be completely representative of ambient conditions in the field. The subsequent steps include calculating absorption and determining k values for each source with the

SLSQP algorithm. The process concludes with the resulting optimization of k values at 370 nm for each component and the calculation of the final OA absorption.

Steps to derive optimized imaginary refractive index k for total or tagged OA.

The resulting k are representative of OA in environmental conditions, which may include interactions with other species, providing an empirical range of k values that account for various OA sources and potential interference.

The optical calculation relies on the external mixing assumption. Attempting to constrain k of OA by assuming internal mixing or core-shell configurations with other species would be complex and unlikely to yield results with less uncertainty. The internal mixing approach would introduce additional modeling uncertainties, such as mixing rules, refractive indices of other species, and OA fractions relative to these species. Therefore, assuming externally mixed OA is considered a simpler approximation and more suited to constrain source specific contributions, despite its inherent limitations.

2.5 Scenario-Based Approach for k Optimization

To investigate the absorption characteristics of different OA sources sources of OA, we have defined six distinct optimization cases, labeled Case 1 through Case 5, as detailed in Table 3. In particular, each case provides the imposes different boundaries for the optimization method described above that are used to find the optimal k value for a specific OA source. Note that the boundaries limit the range where the SLSQP algorithm employed searches for an optimized solution.

Cases 1 to 4 were confined within specific k range boundaries at 370 nm, as recommended by Saleh (2020). These recommended The ranges, originally specified at 550 nm based on chamber experiments (Saleh, 2020), were adapted to 370 nm using the wavelength dependence (w values) provided in Table 1 of Saleh (2020). It is important to note that while the k ranges at 370 nm are broader and may overlap between categories, this is attributed to the greater wavelength dependence observed.

18

Table 3. Scenarios and ranges of *k* used in the optimization process.

Case	Source	Absorption Category	*k* range boundaries at 370 nm
Case 1	Fires, Residential, Shipping	Weakly	0.0049 to 0.1604
	Traffic, Others	Very Weakly	0.0011 to 0.0354
Case 2	Fires, Residential, Shipping	Moderately	0.0181 to 0.4883
	Traffic, Others	Very Weakly	0.0011 to 0.0354
Case 3	Fires	Strongly	0.1219 to 0.6887
	Residential, Shipping	Moderately	0.0181 to 0.4883
	Traffic, Others	Very Weakly	0.0011 to 0.0354
Case 4	Fires	Moderately	0.0181 to 0.4883
	Traffic, Shipping, Residential	Weakly	0.0049 to 0.1604
	Others	Very Weakly	0.0011 to 0.0354
Case 5	Total OA	N/A	N/A

~~To enhance our methodology, we introduced two additional~~ We followed two strategies to optimize *k*. The first approach involves optimizing *k* individually at each monitoring station, allowing for a tailored assessment that accounts for local variations in the properties of OA. The second strategy consolidates data from all stations to derive a single unified *k* value, providing a broader and more generalized perspective on OA absorption characteristics. Both methods were applied separately for specific sources of OA and for the total OA observed, enabling a comprehensive analysis of the influence of source-specific and aggregate OA contributions on absorption properties. This dual approach ensures a robust optimization process that accommodates both localized and generalized environmental conditions.

As detailed in Table 3, Case 1 categorizes OA from fires (GFAS), residential (RESI), and shipping sources (SHIP) as weakly absorbing, with *k* values ranging from 0.0049 to 0.1604. In contrast, traffic (TRAF) and other sources (OTHR) are considered very weakly absorbing, with *k* values from 0.0011 to 0.0354. Case 2 adjusts the absorption levels for OA from GFAS, RESI and SHIP to moderately absorbing, with *k* values from 0.0181 to 0.4883, while maintaining the same very weak absorption for TRAF and OTHR sources as observed in Case 1. In Case 3, OA from GFAS are assigned strong absorption properties with *k* values from 0.1219 to 0.6887, whereas RESI and SHIP are treated as having moderate absorption, similar to the *k* values in Case 2, and the TRAF and OTHR sources continue to be categorized as very weak absorbers. Case 4 adjusts the absorption categorization, treating fires with moderate absorption, while TRAF, SHIP, and RESI are considered weakly absorbing, and OTHR remains very weakly absorbing. Finally, Case 5 involves calculating the optimized *k* by integrating all OA components (ALL) without predefined boundaries, facilitating a comprehensive exploration of *k* values. Note that contribution from both primary and secondary aerosols is accounted within each OA categorization.

3   Results

3.1   OA mass and source contribution

Our study focuses on understanding the light absorption properties of OA across different European environments. Since the light absorption of OA (b_a) is intrinsically ~~linked~~ related to its mass concentration, ~~a~~ the first step is to evaluate the accuracy and reliability of our model in simulating ~~the~~ mass concentrations. ~~In this section, we examine the model's ability to describe the variability of OA mass concentration at the 12 monitoring stations presented in Table 1.~~

Figure 3 shows the time series of the measured and modeled OA mass concentrations for 2018 (note the varying y-axis scales in different panels). ~~For a detailed comparison of modeled versus observed OA concentrations across the same stations, refer to the scatter plots provided in the supplementary material (see Figure S2). Observational data (OBS), depicted by red dots, show the actual OA concentrations measurements at each station. These values provide a baseline against which the model's performance can be evaluated.~~ The modeled concentrations of OA, derived from the source-tagged simulation, are represented by filled colors, where each color shows the contribution from different emission sources. Specifically, SHIP is marked in purple, RESI emissions in light blue, GFAS in orange, TRAF in black, and OTHR in brown (only primary contribution shown). Additionally, Secondary Organic Aerosols (SOA) contribution is depicted in green.

~~As reported in Figure 3 and Table **??**, overall~~ Overall, a good agreement ~~was~~ is observed between measured and modeled OA concentrations~~in terms of statistics metrics (see below). This indicates the model ability to capture the pronounced seasonal trends and the peak concentrations at the majority of the monitoring stations studied. For example, one episode of increased concentration in Marselle site (MAR)in February, when the observed concentrations reached 9.1 $\mu g m^{-3}$, was closely approximated by the model which reported 7.4 $\mu g m^{-3}$. Similarly, a significant event in Ispra (IPR)towards the end of December with observed OA concentration of 27.8 $\mu g m^{-3}$ was closely simulated by the model with a value of 27.4 $\mu g m^{-3}$.~~ We followed the performance assessment approach recommended by Emery et al. (2017) for statistical evaluation of photochemical models. These recommendations are based on statistical metrics that should meet the "goal" or "criteria" proposed by Boylan and Russell (2006), where the "goal" signifies the peak performance expected from a model, and the "criteria" represent a level of performance that should be achievable by most models (see Table S1 in Sect. S2 in the Supplement). A detailed statistical evaluation is included in Sect. S3 in the Supplement. In general, the "criteria" are met in most stations and seasons, although some sites fall short of the more stringent "goal" (Table S2). A key trend observed is that the model performs most robustly during the spring season (MAM), with many stations reaching the "goal" and "criteria". In contrast, the summer (JJA) and winter (DJF) seasons exhibit greater variability.

The residential component consistently emerges as the predominant source across all monitoring sites. A consistent seasonal pattern is evident, particularly during colder months, which is likely associated with the increase in residential heating demand during these months. However, Navarro-Barboza et al. (2024) identified inaccuracies in carbonaceous aerosol emissions attributed to the residential sector within the CAMS_REGv4.2 emission inventory for some western Mediterranean stations (Barcelona (BCN) and Montseny (MSY)), suggesting an overestimation of its contribution which was particularly relevant during winter. This issue is shown in Figure S3 and Sect. S4 in the Supplement, where results using a local bottom-up emission inventory for Spain (Guevara et al., 2020) reveal that traffic emissions are more significant than residential emissions at these sites. This represents a limitation of the dataset utilized in this study and underscores the need for continuous improvement of continental-scale emission inventories such as CAMS_REGv4.2, which remains among the best resources for modeling studies in Europe.

The second most significant contributor to OA mass is SOA, particularly during summer months. SOA shows important spatial and temporal variability, with mass formation peaking during warm periods. For example, as observed in HYY, the model tends to underestimate the high observed OA concentrations in July associated with high SOA mass formation (Heikkinen et al., 2021; Yli-Juuti et al., 2021). Similarly, the model underestimates the high OA concentrations observed in MSY in summer, which were also driven by SOA (e.g., In't Veld et al., 2021). The SOA yields utilized in this model simulation for biogenic precursors, as derived from Pai et al. (2020), might result in limited SOA production and could account for this negative bias.

Other contributions (OTHR) increase during the warm months in most stations, except KRA and IPR. The increase in activity could be related to the increased agricultural practices prevalent during the warmer period (e.g., agricultural waste burning). The emissions of SHIP contribute significantly to stations near ports, such as BCN, DEM, and MAR. Traffic contribution (TRAF) remains fairly low across all sites; although according to Chen et al. (2022), this component should not only be more pronounced at urban stations such as BCN, MAR and HEL, but non-negible at non-urban stations either. The low contribution of TRAF suggests a need for refinement in the emission inventory as discussed above.

Specific events, such as forest fires or high-pollution episodes, are reflected in pronounced peaks in both modeled and observed concentrations, highlighting the model's ability to respond to such episodes. In particular, a significant peak is observed towards the end of July in the MAR and DEM stations, potentially linked to a specific forest fire

event, as depicted by the model ~~fires~~ fire contribution (orange color in Fig. 3). This is corroborated by observations at DEM, although ~~,~~ no observational data is available for MAR for that episode~~to validate the output of the model~~. However, the model does not ~~appear to~~ effectively capture high-pollution events in KRA during ~~the~~ winter, where peaks exceeding 60 $\mu g/m^3$ were monitored. KRA is recognized as a major pollution hotspot in Europe (e.g., Casotto et al., 2023), ~~largely~~ mainly due to the extensive use of coal and wood for energy production and residential heating. This likely ~~accounts for the elevated OA levels~~ explains the elevated levels of OA monitored in KRA during the winter of 2018, ~~given that~~ since the prohibition on solid fuels (coal and wood) in boilers, stoves ~~,~~ or fireplaces was only implemented after September 2019. ~~Additionally~~Furthermore, KRA's location within a basin with poor ventilation makes it susceptible to air pollution buildup (Sekula et al., 2022). These factors indicate potential shortcomings in the emissions data and the model's ability to accurately simulate strong inversion events.
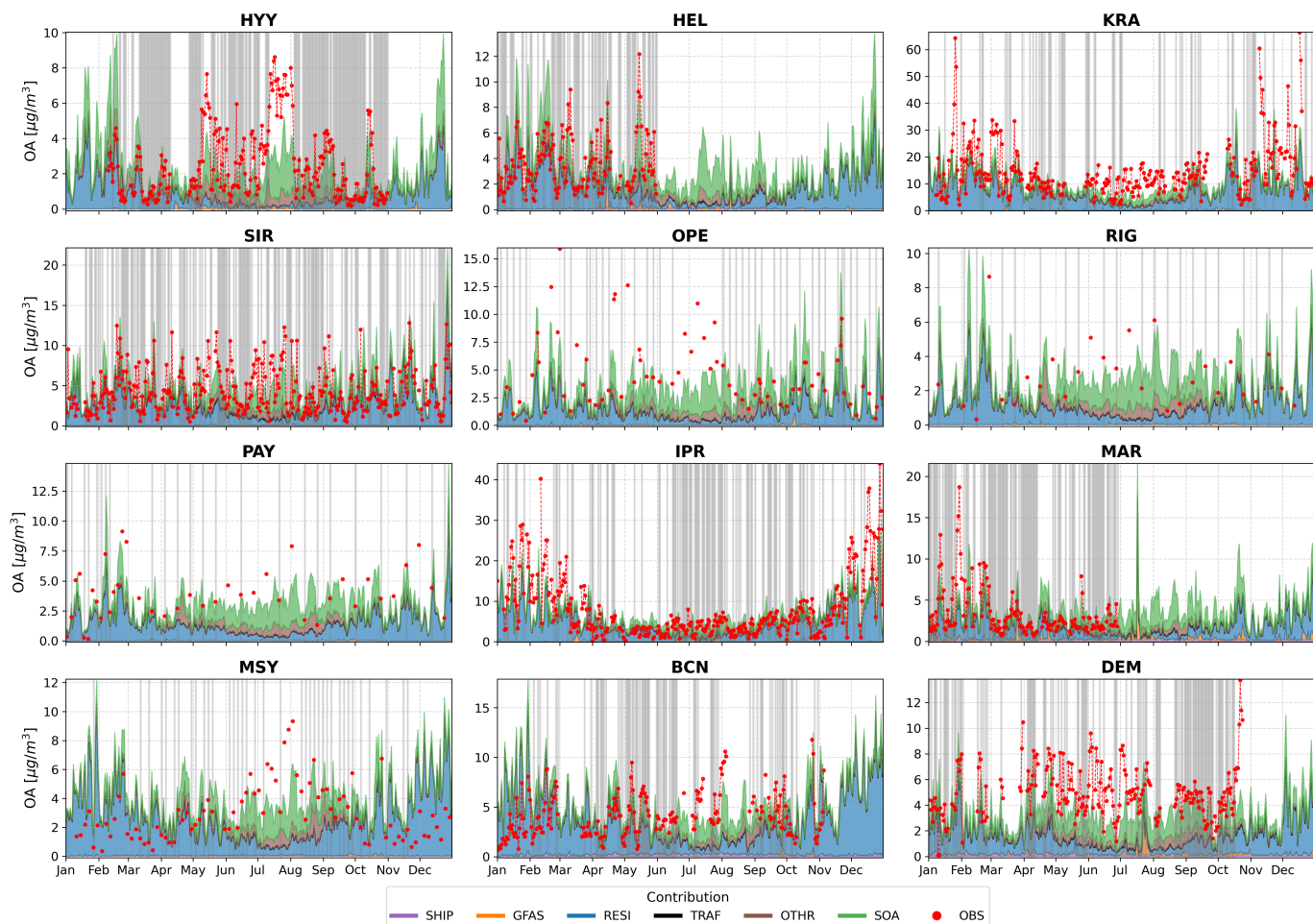
Figure 3. ~~Time series of observed~~ Observed and modeled daily mean OA mass concentrations [$\mu g m^{-3}$] ~~for the~~ at twelve European monitoring stations. ~~Contributions~~ Stacked colors represent contribution from ~~various~~ different emission sources~~to primary organic aerosol including~~: Shipping (SHIP), Residential (RESI), Fires (GFAS), and Other (OTHR)~~are presented. Secondary Organic Aerosol (~~SOA ~~)~~ is shown as a separate component. Observed data points are indicated with red points. Gray background indicates that the bias is within an acceptable range (± 1.5 $\mu g m^{-3}$). Y-axis scales differ across panels.

~~Our analysis is further complemented by a statistical evaluation of OA mass concentrations using five metrics: Normalized Mean Bias (NMB), Normalized Mean Error (NME), Pearson Correlation Coefficient (r), Fraction of Predictions within a Factor of Two (FAC2) of observations, and Fractional Bias (FB). We followed the performance assessment approach recommended by Emery et al. (2017) for photochemical models, particularly for pollutants such as Elemental Carbon (EC) and OC, focusing on metrics including FB, NME, and NMB. These recommendations are based on the "goal" and "criteria" benchmarks proposed by Boylan and Russell (2006), where the "goal" signifies the peak performance expected from a model, and the "criteria"~~

550

represents a level of performance that should be achievable by most models. The metrics are defined in supplementary material Table S1.

Table ?? summarizes the statistical evaluation for the twelve stations (DJF December-January-February; MAM March-April-May; JJA June-July-August; SON September-October-November). Overall, the "criteria" is achieved in most of the stations and seasons, while some sites do not meet the "goal". We observe that the model exhibits its strongest performance during the spring season (MAM), with many stations meeting the "goal" and "criteria" benchmarks. Conversely, the summer (JJA) and winter (DJF) seasons show more variation in the model's ability to accurately reproduce the observed OA concentrations.

During winter (DJF), for instance, the HYY station shows a strong correlation ($r = 0.94$) but a low FAC2 value ($FAC2 = 23.53$). This discrepancy suggests a tendency to overestimate concentrations, which could be attributed to an overrepresentation of residential emissions in the model during this season. In contrast, during spring (MAM), the HEL station achieves a high FAC2 value (93.59%) along with a good correlation ($r = 0.72$), which might be attributed to a balanced influence from various sectors, particularly as fire emissions become more significant during this period (Urbieta et al., 2015; Turco et al., 2017). Most stations have better performance in MAM compared to other seasons, with many achieving their "goal" achievements and benchmarks in NME and NMB, such as SIR with low fractional bias and normalized errors. Notably, a drop in correlation is observed during summer (JJA) and autumn (SON) at some stations (e.g., KRA in SON with $r = 0.34$), but several maintain high FAC2 values, like PAY in JJA (100%) and RIG in SON (100%). This suggests that the discrepancy could stem from challenges in accurately modeling biogenic SOA contributions during the warmer months. The gray highlighting for stations like SIR and OPE in these seasons indicates success in achieving targeted goals for NME and NMB, despite some challenges in FB. Unfortunately, data from stations such as, HEL and MAR is unavailable for the JJA and SON seasons.

Seasonal statistical evaluation of OA concentrations. Goal achievement (Gray) and criteria benchmarks (Bold) based on Emery et al. (2017). NMB: Normalized Mean Bias, NME: Normalized Mean Error, and FAC2 expressed as percentages.

3.2 Imaginary refractive index (k) optimization

The optimization of the imaginary refractive index (k) at 370 nm for OA across the twelve measurement stations presents challenges, particularly presented challenges, primarily due to limitations in data coverage. The data points used Data points for the optimization process were selected based on their consistency with observed OA concentrations. However, the availability of data varied significantly between stations, imposing limitations on the optimization process. For instance, the HEL station provided data only from January to May, and the MAR station had a similarly limited data range. The HYY station data coverage spanned from the end of February to the end of October. Other stations, such as OPE, PAY, RIG, and MSY, contributed relatively few data points throughout the year. This gaps in data coverage could potentially impact This data coverage gap could potentially affect the representativeness of the k optimization results.

The selection criteria for the data points to be used in the optimization process included The optimization process used a bias threshold , where only days with bias selecting only days where the simulation fell within $\pm 1.5 \ \mu g m^{-3}$ of the actual OA measurements were considered (identified in OA measurements (gray background in Figure 3). This approach aimed to ensure improve the reliability of the optimization results despite limitations in data availability results despite data limitations.

24

~~Once the OA measurements had been selected as described above, the aim of the *k* optimization procedure applied was to determine the most suitable *k* for the different sources considered that would optimize the comparison between the simulated and observed OA absorption coefficient.~~

590 ~~Table ?? presents the mean and standard deviation (std) of the optimization results for~~ A detailed discussion of the optimized *k* ~~across stations, classified by representative environments (Regional - REG, Suburban - SUB, Urban - URB; see Table 1), and optimization~~ values for cases 1 through 4 ~~(Table 3). Each case corresponding to unique assumptions discussed in Section 2.5. The mean *k* and std were analyzed for the five sources of study: GFAS, RESI, SHIP, TRAF, and OTHR. The row labeled "ALL" indicates the average values for all stations in Case 4.~~

595 ~~By comparing Table 3 and Table ??, the results of the performed *k* optimization process can be summarized as follow~~is provided in Sect. S5 in the Supplement. Overall, ~~for all settings and Cases (1-4), and also for ALL, the highest *k* was obtained for GFAS compared to the other sources with the highest *k* observed for URB sites , whereas similar k within the std were obtained at REG and SUB sites. In each setting, small differences were observed between Case 1 (GFAS weakly) and Cases 2 and 4 (GFAS moderately) indicating a~~ Case 4 was considered the most appropriate result to analyze absorption at the 12

600 measurement sites based on the consistent convergence of the different sources. A robust estimation of GFAS *k* in-between weakly and moderately absorbing OA ~~particles. Interestingly, in Case 3 (GFAS strongly) *k* reached the lowest allowed limit (cf. Table 3) with zero std (cf. Table ??)~~ was found, suggesting that GFAS OA ~~particles~~ cannot be treated as strongly absorbing.

~~RESI OA particles were considered as weakly absorbing (Cases 1 and 4) and moderately absorbing (Cases 2 and 3). Similarly to GFAS, higher RESI *k* was obtained for URB sites even if for this source the obtained *k* were comparable, within the std,~~

605 ~~among the three considered settings. This similarity could be associated to the fact that RESI emissions are mostly local, thus reducing the differences among the station settings. Moreover, for each setting small differences were observed for RESI *k* among the 4 considered Cases suggesting a robust estimation of the RESI *k* that lied in-between weakly and moderately absorbing OA particles. Note that for both GFAS and RESI the optimization process provided *k* values closer to the upper limit of the weakly category rather than the upper limit of the category moderately.~~

610 ~~Similarly to RESI, SHIP emissions were considered as weakly absorbing in Cases 1 and 4 and moderately absorbing in Cases 2 and 3. Overall, the optimization process provided rather similar *k* among the four Cases at URB sites with *k* values that were higher compared to REG and SUB. At URB sites, the SHIP *k* lied in-between the categories weakly and moderately with *k* values that, as for GFAS and RESI, were closer to the lower limit of the category moderately. At SUB sites, the SHIP *k* reached the lowest limit allowed for the category weak (0.005; Cases 1 and 4) and moderately (0.02; Cases 2 and 3) suggesting very~~

615 ~~low *k* of SHIP for this setting. At REG sites, SHIP *k* was higher than at SUB sites with low variability among Cases 1, 2 and 4 and higher values and much higher std for Case 3. Also for REG sites the optimization process suggest that~~ A similar result applies for RESI. In contrast, SHIP OA emissions ~~were~~ appeared to be more weakly absorbing than moderately absorbing~~.~~

~~TRAF emissions were treated as very weakly absorbing in Cases 1, 2 and 3 and as weakly absorbing in Case 4. Interestingly, the highest TRAF *k* were obtained for URB sites whereas much lower *k* were obtained at REG and SUB sites. At URB~~

620 ~~sites, Cases 1, 2 and 3 provided *k* values in the upper range of the very weakly category (0.04; cf. Table 3) with very low std suggesting that TRAF emissions were~~ whereas TRAF emissions leaned toward weakly absorbing rather than very weakly

absorbing. ~~In fact, Case 4 provided a TRAF *k* value of 0.06 that lied in-between the lower and upper limit of the category weakly absorbing. At both SUB and REG sites, the obtained TRAF~~ Very low *k* values were ~~much lower compared to URB sites. This result is consistent with recent evidences that OA from traffic at urban sites can be an important source of brown OA (e.g., Ho et al., 2023). Moreover, traffic emissions are not expected to be primarily local at REG and SUB sites, thus likely contributing to the observed reduced TRAF *k* in these two settings due to physico-chemical OA processes as dilution and photobleaching.~~

~~OTHR emissions were treated as very weakly absorbing for all the considered cases (1-4). The optimization process provided very low *k* values confirming the~~ derived for OTHR sources, confirming their very low absorption properties~~of OA particles emitted by OTHR sources. Note that higher OTHR *k* values were obtained at URB sites compared to REG and SUB sites where the obtained *k* were very close to the lower *k* value in the category very weakly (cf. Table 3).~~

~~Finally, and consistently with what was commented above, for the ALL case~~. In summary, the obtained *k* values followed the following order: GFAS>RESI>TRAF>SHIP>OTHR.

~~Statistical summary of mean and standard deviation (std) values for the optimization of the imaginary refractive index across the three settings (REG, SUB, URB) and the four cases (C1, C2, C3, C4). Each case corresponds to different assumptions detailed in Table 3, analyzed across five OA sources: GFAS, RESI, SHIP, TRAF, and OTHR. The row labeled "ALL" represents the averaged values across all stations for scenario C4. Metric mean std mean std mean std mean std mean std Setting Case Case 1 0.0619 0.0396 0.0458 0.0469 0.0196 0.0168 0.0093 0.0141 0.0015 0.0009 Case 2 0.0506 0.0434 0.0482 0.0448 0.0210 0.0071 0.0070 0.0139 0.0018 0.0010 Case 3 0.1241 0.0053 0.0476 0.0447 0.0527 0.0536 0.0068 0.0140 0.0014 0.0005 Case 4 0.0615 0.0387 0.0451 0.0462 0.0182 0.0150 0.0122 0.0132 0.0014 0.0008 Case 1 0.0409 0.0154 0.0409 0.0154 0.0049 0.0000 0.0011 0.0000 0.0014 0.0005 Case 2 0.0403 0.0148 0.0403 0.0148 0.0191 0.0017 0.0011 0.0000 0.0013 0.0003 Case 3 0.1219 0.0000 0.0395 0.0135 0.0181 0.0000 0.0011 0.0000 0.0011 0.0000 Case 4 0.0398 0.0146 0.0398 0.0146 0.0049 0.0000 0.0049 0.0000 0.0012 0.0001 Case 1 0.0924 0.0354 0.0635 0.0535 0.0418 0.0481 0.0354 0.0000 0.0098 0.0109 Case 2 0.0998 0.0238 0.0635 0.0534 0.0445 0.0456 0.0354 0.0000 0.0092 0.0102 Case 3 0.1229 0.0017 0.0634 0.0535 0.0527 0.0599 0.0345 0.0015 0.0091 0.0110 Case 4 0.0934 0.0291 0.0625 0.0551 0.0314 0.0458 0.0579 0.0078 0.0081 0.0105 ALL Case 4 0.0640 0.0342 0.0481 0.0388 0.0182 0.0231 0.0218 0.0229 0.0030 0.0052~~

~~Based on the aforementioned *k* optimization process, Case 4 was considered as the most appropriate to simulate absorption at the twelve measurement sites.~~

Figure 4 shows the ~~optimized~~ resulting *k* at 370 nm for total and individual components of ~~the OA at the different monitoring sites. Two different approaches were used to obtain the results. We determined the optimal~~ OA in the 12 sites. Results from two approaches are shown: optimizing *k* ~~either~~ by individual station (stn) ~~or~~ and by combining all data points ~~from every site~~ (all). The figure ~~illustrates the results for both~~ compares results from Case 4~~(based on source contribution)~~, which uses source-tagged contributions, and Case 5~~(, which applies~~ a single value for all ~~)~~sources without source tagging.

~~The optimization~~ Optimization based on the total OA mass per station, Case 5 (by stn), results in *k* values ranging from 0.005 (MSY site) to 0.07 (PAY site), which are representative of a very weakly to weakly/moderately absorbing OA (Table

3). In fact, 0.07 also falls within the lower range of the moderately category. A result of the overlap of k ranges at 370 nm as mentioned before.

For REG stations, the optimized k are notably low reflecting the importance of the contribution of biogenic SOA at these sites. MSY stands out with the lowest k value of 0.005, which can be explained by the large contribution to OA from biogenic SOA (over 50%) characterized by very low absorption properties (In't Veld et al., 2023; Nakayama et al., 2010, 2012). Similarly, the low k value (0.01) derived for HYY also indicates a high presence of biogenic SOA (Chen et al., 2022). Among regional stations, the highest OA k were obtained for IPR (0.03) and PAY (0.03) likely reflecting the influence of agricultural and domestic biomass burning sources at these sites and the strong accumulation of absorbing POA in winter (see Figure 3) (Lanz et al., 2010; Bozzetti et al., 2016; Daellenbach et al., 2017; Wolf et al., 2017).

In suburban environments, represented by KRA, SIR, and DEM, the k values suggested a mix of urban influence and regional aerosol contributions. For KRA, a pollution hotspot, a k value of 0.02 was derived. A moderately absorbing environment likely due to coal combustion, shipping activities from river cruise boats, and household heating emissions (Casotto et al., 2023; Skiba et al., 2024). On the other hand, SIR and DEM present k values of 0.01 and 0.02, respectively, are representative of environments that mix local urban emissions with regional air masses.

For urban stations, such as HEL, MAR, and BCN, weakly to moderately absorbing OA are derived, reflecting the diverse nature of urban emissions. Both HEL and BCN have similar k (0.0284 and 0.0262), while MAR presents a notably higher value (0.0494). The latter attributed to the harbor activities and local industrial emissions at that site (e.g., Chazeau et al., 2022).

Comparing the results with the single k derived from Case 5 (all) (dark green bars in Fig. 4), which corresponds to k of 0.02, suggests that OA ~~particles~~ across the different environments can be described on average as weakly absorbing~~particles~~. This result is attributed to the averaging effect of combining highly absorbing components with those that are very weakly absorbing into a single, undifferentiated category. Consequently, the optimization in this case likely masks the variability in absorption strengths of individual OA components observed across Europe and may introduce biases in model absorption estimates.

Now, we analyze the results using the granular data provided by each individual station and emission source, Case 4 (by stn), wherein the optimization is performed independently at each site (blue bars in Fig. 4) yielding different k values for each source. The observed variability for each component is as ~~follow~~follows: GFAS ranges from 0.03 to 0.13, RESI from 0.008 to 0.13, SHIP from 0.005 to 0.08, TRAF from 0.005 to 0.07, and OTHR from 0.001 to 0.02. These variations are associated with the different environmental conditions of each station, within the limitations of our methodology to properly describe each environment and the fact that sources that are negligible at a specific site ~~introduces~~ introduce additional complexity in deriving a robust estimate of k for them.

Among regional background stations, PAY stands out showing the highest k for GFAS (0.13) and RESI (0.13) components, suggesting the significant influence of sources such as residential heating, which was previously observed by Ciarelli et al. (2016), or the strong impact of regional events such as wildfires or agricultural waste burning. In contrast, RIG shows the lowest k for GFAS (0.03), while MSY presents the lowest value for RESI (0.008). As our optimization of k relies on comparing absorption measurements with modeled OA source components (assuming ranges of k from different sources), there ~~exists a~~ is an inherent relationship between mass contribution and absorption. This implies that although k is independent of mass, sector

27

contribution could assign higher/lower *k* values depending on the model uncertainties. Therefore, at regional sites like MSY, the lower *k* values for RESI may indicate reduced residential activity, as shown by Pandolfi et al. (2014) and Navarro-Barboza et al. (2024).

Suburban stations such as SIR, KRA, and DEM show consistent results across components, with *k* values for sources like GFAS and RESI significantly higher than for SHIP, TRAF, and OTHR. The *k* values for RESI and GFAS in DEM are nearly twice as high as those derived in SIR and KRA, indicating a mix of urban influence and regional aerosol contributions.

Conversely, urban stations, including HEL, MAR, and BCN, present significant variability, reflecting the diverse nature of urban emissions. MAR shows the highest *k* for GFAS and RESI (0.13), suggesting a strong contribution to absorption from these sources. Notably, TRAF (0.06) is more significant in these urban stations compared to regional and suburban locations. In HEL, *k* from shipping indicates a non-negligible contribution from this source, while in BCN, OTHR emerges as more significant (0.02), highlighting the complex and varied nature of urban aerosol sources.

Finally, Case 4 (all) represented by orange bars in Figure 4 involved the optimization by aggregating data from all stations while still differentiating between sources. The resulting *k* values were 0.06 for GFAS, 0.04 for RESI, 0.06 for SHIP, 0.005 for TRAF, and 0.0011 for OTHR. These results are consistent with those reported in the literature, for instance, Feng et al. (2013) derived a *k* of 0.075 for moderately absorbing BrC from biomass burning at 350 nm, which is in agreement with our optimization results for GFAS. Similarly, the *k* value for SHIP is consistent with Corbin et al. (2018), who reported a comparable value of 0.045 at 370 nm for this source. The optimized value for RESI is also consistent with literature, considering its association with biofuel combustion. Our estimation for TRAF, however, appears to be more than two times higher than the value found in the literature for this source (0.002 at 365 nm for octane combustion as reported by Hossen et al. (2023)). Nonetheless, we have observed considerable variability among URB sites, highlighting the intricate nature of urban environments. OTHR is identified as the least absorbing source, which is a reasonable outcome given its categorization.
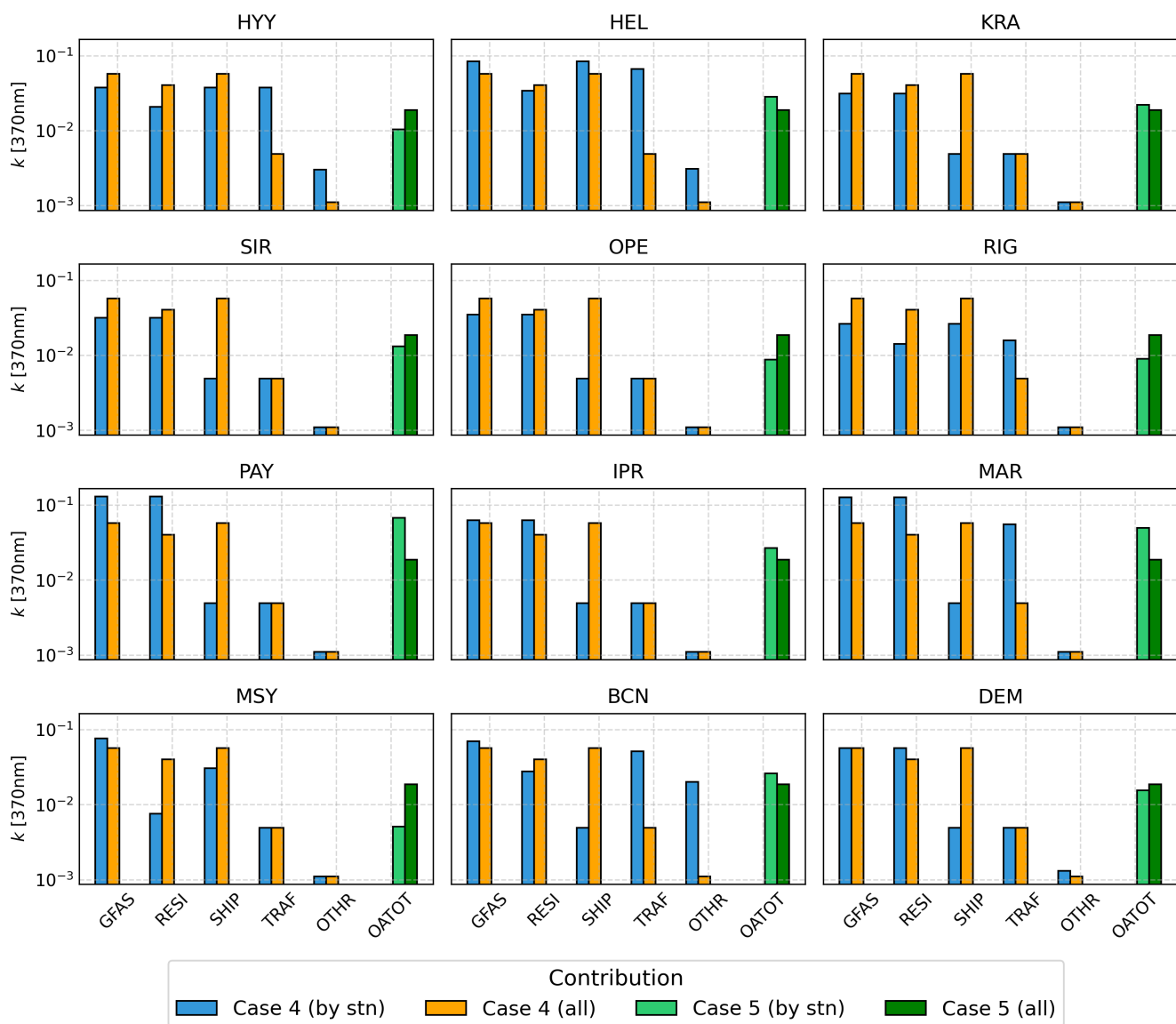
Figure 4. ~~Comparative optimization~~ <u>Optimization</u> of *k* at 370 nm for ~~various~~ OA sources, ~~illustrating the results of~~ <u>comparing</u> two ~~optimization~~ strategies: Case 4 ~~, which optimize~~ <u>(source-tagged) optimizes</u> *k* values for five distinct ~~OA~~ sources ~~including, fires~~ (GFAS), TRAF, SHIP, RESI, ~~and~~ OTHR), ~~and~~ <u>while</u> Case 5 ~~, which considers the total OA and~~ <u>(non-source-tagged)</u> optimizes <u>a single</u> *k* ~~by aggregating data across all stations~~<u>for total OA</u>. Both cases ~~present two approaches - one with *k* values optimized for each station and another with a single k value derived~~ <u>show results</u> from ~~all stations~~ <u>station-specific ('by stn') and all-station</u> combined <u>('all') approaches.</u>

In general, our findings agree well with values reported in the literature for specific sources. For instance, Pani et al. (2021) identified a *k* of 0.12 at 370 nm for biomass burning closely aligned with the site most influenced by this source, such as PAY. Furthermore, the SHIP component in our study shows a significant *k*, approaching to Corbin et al. (2018) who derived a value

of 0.045 at 370 nm. Conversely, our TRAF results show a variation of *k* from 0.005 to 0.07, falling in the upper range reported in the literature for specific sources, such as 0.002 at 365 nm for BrC from octane combustion (Hossen et al., 2023), or 0.027 for propane, 0.006 for diesel, 0.00074 for gasoline combustion reported at 550 nm (Lu et al., 2015).

3.3 OA Absorption results

In this section, we build upon the *k* values ~~obtained~~ derived in the previous section to analyze the OA absorption ~~derived from model simulation~~ and its annual variability. We explore the impact of using results obtained from aggregating all data (all) ~~or~~ versus exploiting the full granularity of the model and the observational data set (by stn).

3.3.1 ~~Absorption with optimized *k* by aggregating all data~~

The latter provides a closer alignment of the modeled absorption coefficients with the measurements as expected. Determining a specific *k* for each site and emission source gives detailed information on the absorption characteristics of the site environment. Nevertheless, this detailed information is too location-specific to be utilized in atmospheric models. Regardless, the analysis offers valuable information on the strengths and limitations of *k* discussed in the previous section for modeling applications.

Figure ~~??~~ 5 shows a scatter plot of the monthly mean observed versus modeled OA absorption ~~at each monitoring site. The plot uses results from~~ for source tagged (Case 4) and non-source tagged (Case 5) cases considering 'all' and 'stn' approaches (Figures S4 and S5 in the Supplement present similar information at daily resolution). Note that all observational data are used in this comparison beyond the observations employed in the optimization process (see Sect. 3.2). Additionally, Figure 6 shows the time series of the absorption of OA at 370 nm simulated in Case 4 (all) and Case 5 (all) ~~, where *k* values were obtained by using all the monitoring stations combined. To calculate total absorption~~ and the observational data for each monitoring site (by 'stn' in Fig. S6 in the Supplement). Although the absorption values could seem low, the annual mean OA absorption at 370 nm calculated from observations represented around 2-20% of the total measured absorption at some regional/remote sites (MSY, OPE and HYY) reaching contributions around 20-40% at the remaining sites. The OA absorption is the lowest in summer due to the lack of important primary BrC sources as domestic biomass burning.

In both figures, Case 4 (all) uses individual *k* values tailored to specific OA components ~~:~~ (0.0571 for fires, 0.0403 for RESI, 0.0571 for SHIP, 0.0049 for TRAF, and 0.0011 for OTHR). Meanwhile, Case 5 (all) applies a single *k* value of 0.0187 across all sources. ~~The key difference between the cases is that Case 4 includes a detailed source apportionment, discerning five different OA sources, while Case 5 considers the total OA without source differentiation.~~ Case 5 represents the common approximation adopted by models in the literature (Takemura et al., 2005; Donner et al., 2011; Tegen et al., 2019) to describe the optical properties of aerosol components, where a single ~~refractive index~~ *k* is assigned to each aerosol component. Conversely, Case 4 introduces the refinement at the source level to investigate the benefit of exploiting the source contribution to describe absorption. ~~Additionally, Figure 6 shows the time series of the absorption of OA at 370 nm simulated in Case 4 (all) and~~ The source-tagged method allows clearly the model to better account for the specific characteristics of OA source emissions at different sites, particularly in urban areas where sources of OA are more variable. In contrast, the

non-source-tagged approach (Case 5(all) and the observational data for each monitoring site) results in a broader range of errors, especially in higher-absorption environments such as urban and suburban areas.
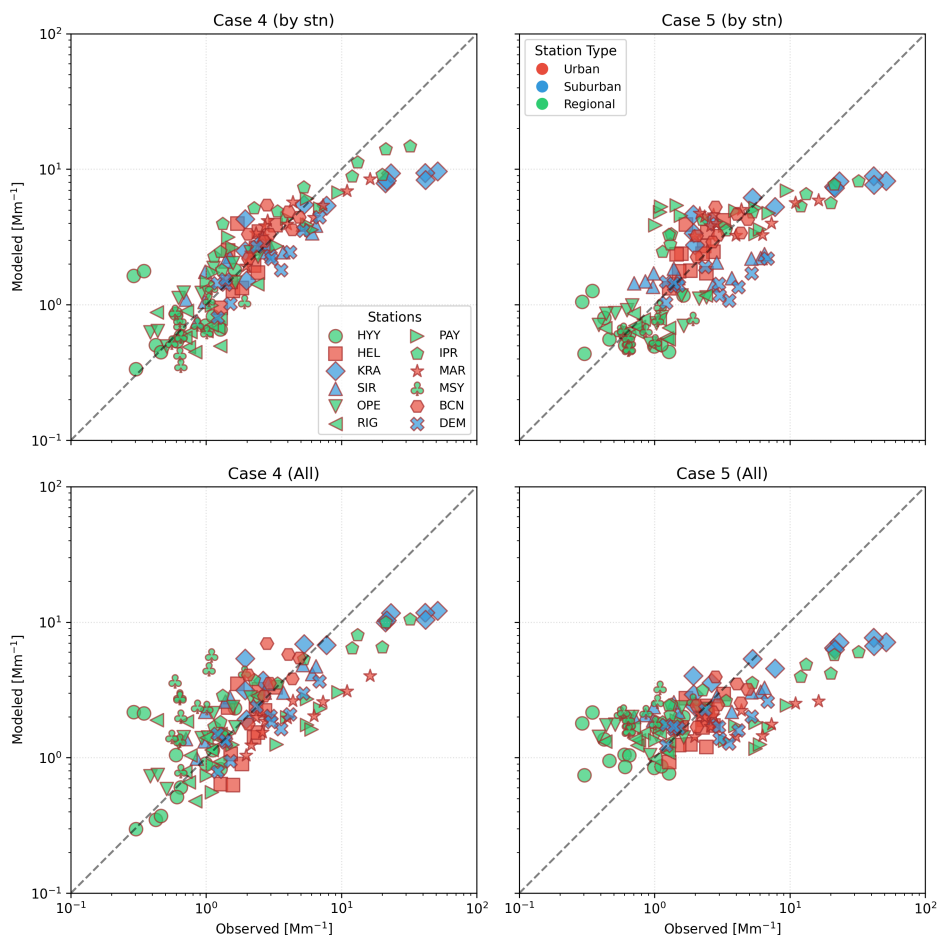

Figure 5. Monthly mean observed versus modeled OA absorption for Case 4 and Case 5 including approaches by 'stn' and 'all'. Symbols indicate individual stations and colors station type.

In Case 4 (dark green circles in Fig. ??all), the correlation coefficients (r) range from 0.34 to 0.74 across all stations and the fractional bias (FB) values vary widely from -70% to 107% (yellow circles in Fig. S4). Regional stations (OPE, PAY, and IPR), generally exhibit high correlations (>0.6) and a tendency to overestimate. Specifically, in MSY, the overestimation persists consistently Similar correlation results are obtained when optimizing per station (Case 4 (by stn) in Fig. S5), but with significant improvements in FB at all sites (see Table S4 in the Supplement). The use of station-specific and source-specific k values substantially reduces the bias as expected.

Among regional background stations, MSY stands out by improving results from a strong overestimation throughout the year (FB: 107%, assuming a constant k for each OA source over all aggregated data Case 4 (all)) to a slight underestimation in

Case 4 (by stn), as shown in Figure ~~6 orange. Conversely, in~~ S6 blue line. Both winter and summer periods are adjusted at this station, a good example of the added value of refining the characterization of sources for a specific environment. Other stations such as PAY, RIG, and IPR also show consistent improvements compared with Case 4 (all). In HYY, this overestimation is predominantly observed during the initial months, while in RIG, it becomes noticeable ~~towards~~ toward the end of the year. This pattern might not necessarily reflect higher absorption but could be due to overrepresentation of absorbing sources ~~in~~ at these sites, ~~that~~ which are characterized by the dominant contribution of biogenic SOA typically with little or no absorption. ~~This tendency could be attributed to the considerable influence of secondary aerosol contributions.~~ For instance, SHIP k value could be remarkably high, making it comparable to the values attributed to fires and potentially biasing the overall absorption metric at some of these sites.

Suburban stations such as SIR, KRA, and DEM show good r values in Case 4 (all), specifically 0.74, 0.57, and 0.67, respectively. SIR stands out with a small FB of 3.8%, reflecting a very accurate representation of observed absorption. However, the model tends to underestimate the OA absorption for KRA and DEM, a phenomenon that is particularly pronounced at KRA (in both all and stn cases), where absorption values exceed 50 Mm^{-1} at 370 nm. This underestimation is likely ~~linked~~ related to the increased emissions ~~from~~ of households and the energy industry at KRA site, as reported by Zgłobicki and Baran-Zgłobicka (2024), and the limitations previously highlighted in Section 3.1. The underestimation is predominantly observed during winter for KRA and DEM, whereas for SIR, the underestimation occurs mainly during warm months, as illustrated in Figure 6. These seasonal discrepancies indicate that while the emission inventory (CAMS-REG-APv4.2) effectively captures the emissions near the SIR station, it may not fully account for the increased emissions during winter at KRA and DEM.

~~The urban stations~~ HEL, MAR, and BCN urban stations show very different model performances. On the one hand, MAR is characterized by a substantial underestimation with low correlation value (0.49) and a ~~notably~~ notable negative FB of -82.3%. ~~Conversely~~In contrast, BCN exhibits significant overestimation in the first months of the year, likely related to attribution issues with residential, traffic, and shipping emissions ~~(Navarro-Barboza et al., 2024)~~ as discussed in Section 3.1 and Section S4 in the Supplement. On the other hand, HEL shows good agreement with the observations (r = 0.51, FB = -7.5%). The urban stations show different responses to the refined optimization by stn. Modeled absorption improves compared to Case 4 (all) in BCN and MAR, while in HEL a slight degradation occurs during the colder months. The fire event identified by the model in July in MAR is simulated with a significant overestimation. This could indicate a limitation in the fire emissions data for this specific event.

In Case 5 (all), where no source-specific components for OA are considered, ~~correlation generally degrades compare~~ the correlation generally decreases compared to Case 4, with r values ranging from 0.28 to 0.65 across stations. FB values ~~show again~~ again show a wide variability, ~~extending~~ ranging from a strong underestimation at a suburban site such as KRA (FB = -113%), particularly observed during winter, to an overestimation at a regional site ~~like~~ such as OPE (FB = 42%), mainly observed during summer and in MSY throughout the year. As seen before, results derived using k by station show clear improvement in FB at all sites.

The differences between Case 4 and Case 5 highlight the benefit of using source specific k in simulating OA absorption. ~~While~~ Although Case 5 represents the common practice in atmospheric modeling of using a unique refractive index to describe

aerosol optical properties, Case 4 provides an additional refinement that even improves seasonality, as illustrated in Figure 6 where Case 4 (all) follows increased absorption during winter and lower values during warmer months, while Case 5 (all) introduces important biases in some sites. Notably, OPE, SIR or HYY show substantial overestimation during the summertime in Case 5 due to imposing an overly absorbing biogenic SOA, an issue that is effectively resolved in Case 4.

795

~~Daily mean observed versus modeled OA absorption for Case 4 (all) and Case 5 (all) scenarios, with the imaginary refractive index (k) values derived from aggregated data across all monitoring stations. Each panel includes the correlation coefficients (r) and fractional bias (FB).~~
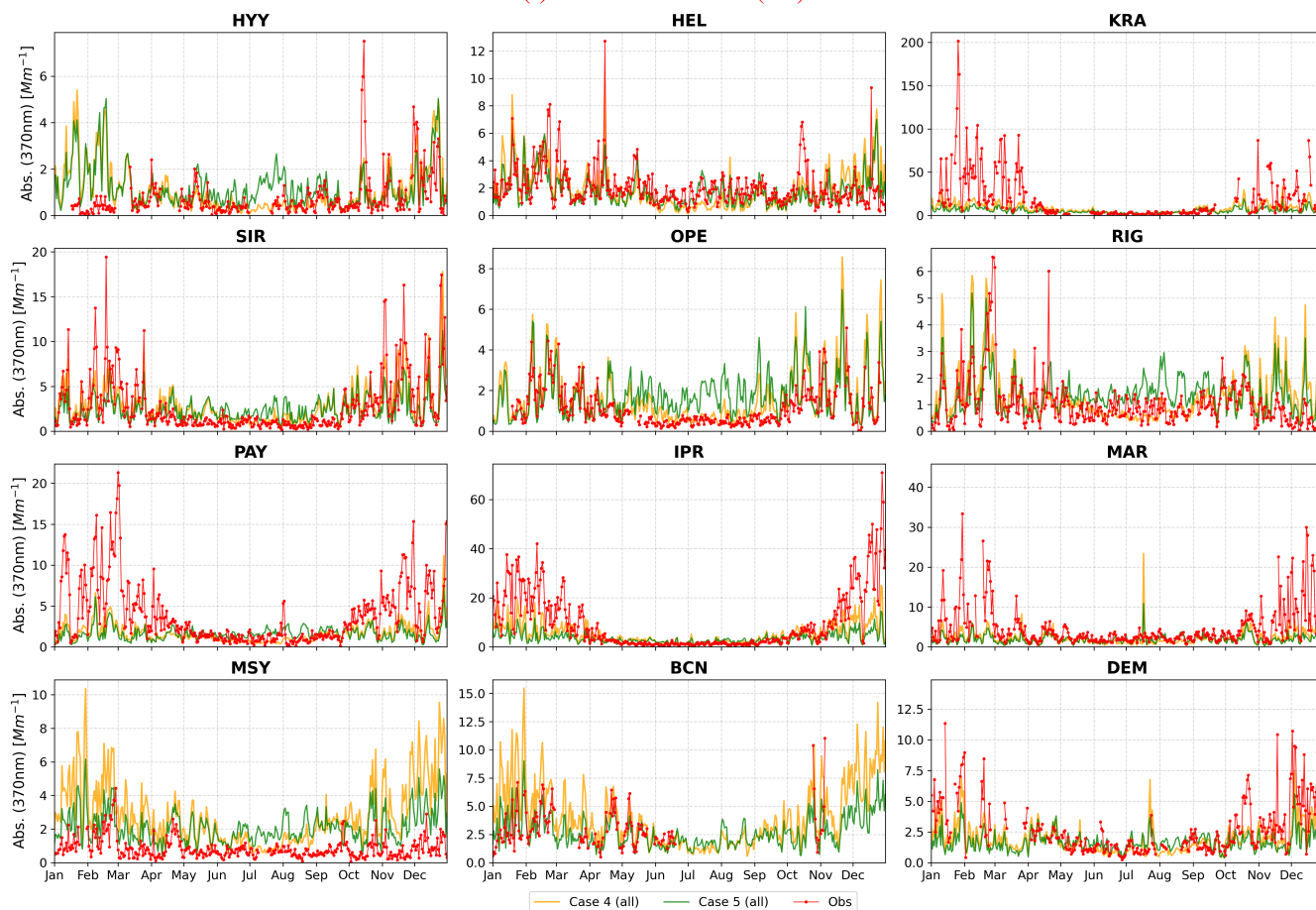

Figure 6. ~~Time series of the~~ OA light absorption ~~at~~ (370 nm~~across the~~) time series for 12 ~~monitoring stations~~sites. ~~Lines plot observed absorption~~ Observed (Obs) in red and modeled absorption for Case 4 (all) (orange line) and Case 5 (all) (dark green line). *k* values derived by combining data from all stations.~~Each set of panels corresponds to one season of the year (DJF: December-January-February, MAM: March-April-May), JJA: June-July-August), and SON: September-October-November).~~

~~In this regard~~Finally, Figure 7 shows the mean seasonal spatial variations in OA ~~absorption coefficient~~ light absorption at 370 nm simulated by MONARCH ~~for~~ at the surface level in Europe. Both the total absorption ~~coefficient~~ and the source con-

tributions are shown. The results are calculated based on optimized k for each OA source derived from Case 4 (all)~~aggregating data from all stations~~.

800 The total OA absorption shows the combined effect from all sources, with higher absorption observed in Central and Eastern Europe. Particularly relevant are the hot spots in the Po Valley (Italy), some regions in central and southern Poland and Romania reaching absorption ~~coefficient~~ values above 20 Mm^{-1}. RESI stands as the dominant contributor to total OA absorption, especially during the colder seasons (DJF, SON). In winter, the mean total absorption in Europe is around 0.9 Mm^{-1}, with residential sources explaining 80% of this (0.7 Mm^{-1}). Absorption shows a clear seasonality across Europe, as seen in Figure

805 6. During summer, ~~RESI contribution~~ the contribution of RESI to light absorption (at 370 nm) in Europe reaches its minimum value, with a mean absorption ~~coefficient~~ of 0.1 Mm^{-1}, representing 28% of the summer OA absorption in Europe. ~~Spring and Autumn periods are characterized by still~~ The spring and autumn periods are still characterized by significant levels of absorption of 0.6 Mm^{-1} and 0.7 Mm^{-1} on average, respectively, dominated by RESI.

The second major source of absorption in our simulations is attributed to GFAS, particularly important during events in the

810 summer (0.15 Mm^{-1} on average and maximum mean values above 10 Mm^{-1}). The mean absorption over Europe from fires is lower compared to residential sources, but surface dominates in certain areas, especially in northern and southeast Europe, where strong fires were detected by the satellite product. Notably, GFAS increases the background absorption in Europe with absorption values around 0.1 to 1 Mm^{-1}. Spring and ~~Autumn are important wild fire~~ fall are important wildfire seasons in eastern Europe, where large regions are affected by notably high GFAS absorption.

815 ~~Another major contributor to absorption appears to be SHIP~~ SHIP emerge as another significant contributor to light absorption, with high absorption levels reaching values close to 5 Mm^{-1} identified along major shipping routes, such as the English Channel, the North Sea, and the Mediterranean Sea. In this sense, coastal regions are affected by this source, and the Mediterranean ~~seas exhibit~~ sea exhibits significant increases in absorption compared to inland areas. Some contributions are also visible along river routes in eastern Europe. Shipping sources contribute relatively little to mean absorption in Europe, with the highest

820 values in spring (0.02 Mm^{-1}).

Traffic-related ~~absorption coefficients at 370 nm are~~ light absorption is relatively low compared to residential and shipping sources. There is a slight increase in absorption in urban areas and major transportation corridors, with minor seasonal variability in this source. The traffic sources show their highest mean absorption ~~coefficient~~ in the surface layer in winter (0.04 Mm^{-1}), dominant in central Europe. ~~Absorption from other sources~~ OTHR absorption is generally low across Europe, with

825 minor seasonal variations. The highest mean ~~absorption from OTHR occurs in~~ OTHR absorption occurs in the autumn (0.08 Mm^{-1}).
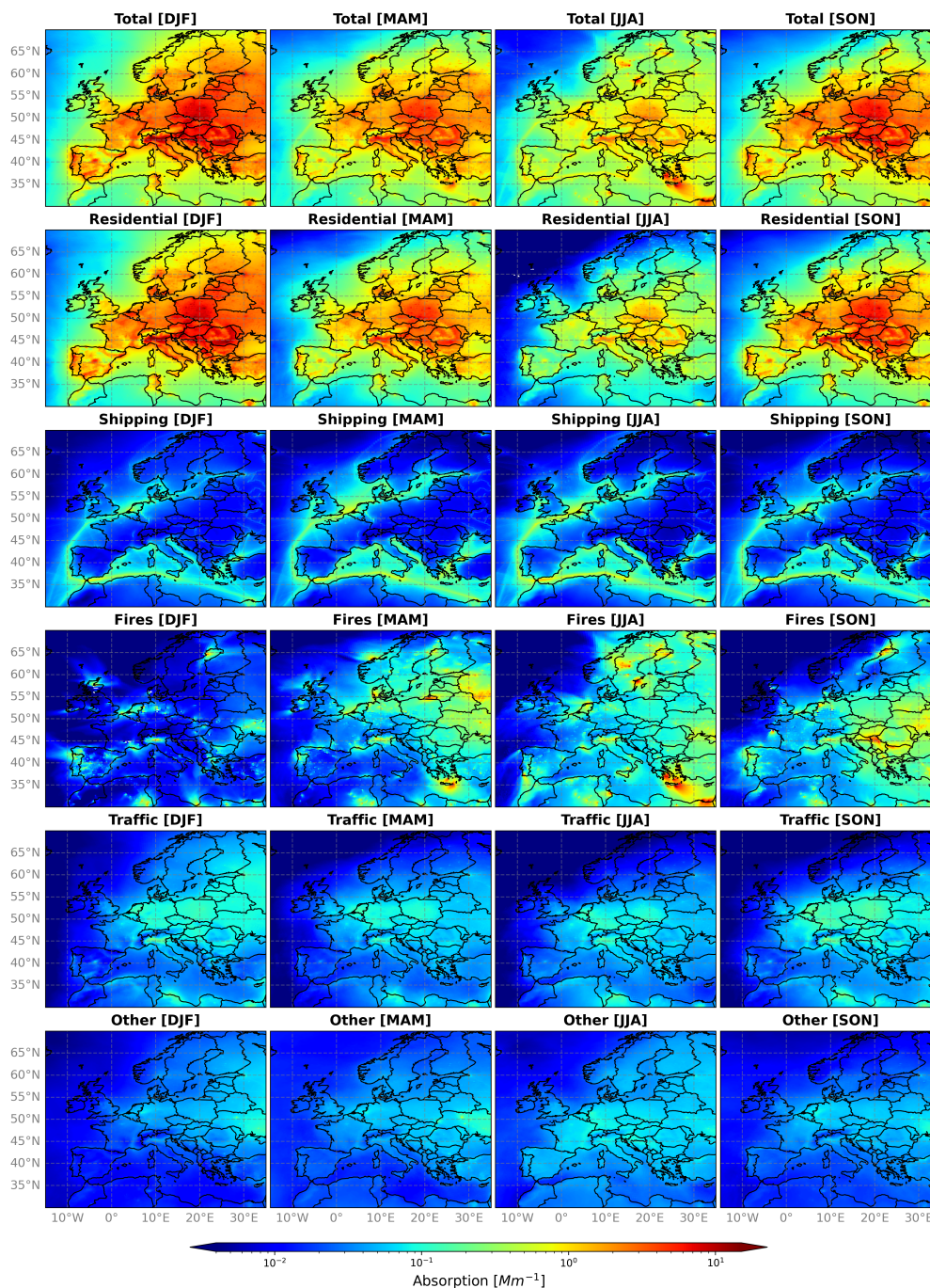
Figure 7. Seasonal ~~source contribution to~~ OA surface absorption ~~at 370nm~~ (370 nm) source contributions in Europe~~for the year~~, 2018. MONARCH simulation ~~using the~~ with optimized *k* ~~for each OA source derived~~ values from Case 4 (all) ~~shown in~~ (Fig. 4, orange bars~~in Figure 4)~~. ~~The seasonal breakdown is as follows~~Columns: the first column represents December-January-February (DJF~~)~~, ~~the second column represents~~ March-April-May (MAM~~)~~, ~~the third column represents~~ June-July-August (JJA~~)~~, ~~and the fourth column represents~~ September-October-November (SON~~)~~. ~~The rows indicate different sources, with the top row showing the~~ Rows: total, ~~followed by~~ residential, shipping, fires, traffic, ~~and~~ other sources~~in descending order~~. 35

3.3.1 ~~Absorption with optimized *k* by station~~

~~Ultimately, a closer alignment of modeled absorption coefficients with measurements can be achieved by optimizing *k* for each individual monitoring site. Determining a specific *k* for each site and emission source gives detailed information on the absorption characteristics of the site environments. Nevertheless, this detailed information is too location-specific to be utilized in atmospheric models. Regardless, the analysis offers valuable insights into the strengths and limitations of *k* discussed in the previous section for modeling applications.~~

~~Figure **??** shows scatter plots of modeled vs observed data. Moreover, Figure **??** depicts the time series of absorption at 370 nm for the twelve monitoring stations for these new two cases, Case 4 (blue line) and Case 5 (light green line).~~

~~Looking at the results for Case 4 (by stn) (blue dots in Figure **??**), and comparing them with those of Case 4 (all) in Figure **??** (orange dots), we observe similar r values ranging from 0.36 to 0.74 in both figures. However, optimizing per station significantly improves the FB values at all sites (see Table S2). The use of station-specific and category-specific *k* values appears to substantially reduce bias, as expected. Among regional background stations, MSY stands out improving results from a strong overestimation (FB: 107%, assuming a constant *k* for each OA source over all aggregated data, orange line in Figure 6) to a slight underestimation, as shown in Figure **??** blue line. Both winter and summer periods are adjusted in this station, a good example of the added value of refining the characterization of sources for a specific environment. Other stations such as PAY, RIG and IPR also show consistent improvements compared with Case 4 (all).~~

~~At suburban sites, the model reasonably captures the absorption at DEM, particularly noting the well-captured peaks during winter. Interestingly, KRA persistently shows large underestimations during colder months (FB = -103%). This clearly indicates the limitations in the way emissions are represented in the inventory used in this study.~~

~~Urban stations show different responses to the refined optimization. Modeled absorption improves compared to Case 4 (all) in BCN and MAR, while in HEL a slight degradation during the colder months occurs. In general, the model captures the peaks throughout the year. The fire event identified by the model in July in MAR is simulated with a significant overestimation. This could indicate a limitation in the fire emissions data for this specific event.~~

~~In Case 5 (by stn), a unique station-specific *k* value is employed without source differentiation. When comparing r values with the approach that utilizes a single *k* across all stations (as depicted in Figure **??**), consistent results are found with a clear improvement in the FB across all stations as also shown in Case 4. This tailored approach generally leads to underestimations of the absorption coefficient at 370 nm in the surface layer at most of the twelve stations studied. In contrast, absorption is notably overestimated at PAY (regional background station) from April to October. The limited number of observations used in the optimization step at this site, mainly dominated by few winter measurements, could explain the overestimated *k* value.~~

Overall, the insights gained from this analysis recommends adopting approaches towards refining *k* values used in models to better represent the unique characteristics of ~~each station and emission source~~different environments and emission sources. The tailored approach of Case 4 (all), with its more granular differentiation of *k* values, contributes in the characterization of the different sites investigated in this work.

~~Similar to Figure **??**, but with *k* derived for each station.~~

~~Similar to Figure 6 but the *k* optimization process was done at each station.~~

4 Summary and conclusions

In this ~~study, we explored the refractive imaginary~~ work, we have analyzed the light absorption of OA in Europe by optimizing the imaginary part of the OA refractive index (*k*) ~~for OA components from different sources,~~ at 370 nm. Five different components of OA were studied including fires (GFAS), residential (RESI), shipping (SHIP), traffic (TRAF), and ~~others emissions~~ other sources (OTHR). Our analysis relied on 12 distinct monitoring stations~~throughout Europe~~, representative of regional, suburban, and ~~background urban environments~~ urban background environments, to capture the diverse environmental conditions prevalent at each site. ~~Using a synergistic approach that combined both modeling and observational techniques, we conducted~~ We used the MONARCH model to perform year-long ~~simulations covering the year 2018. These simulations were designed to evaluate the OA mass concentrations using the MONARCH chemical transport model and constrain the OA light absorbing properties.~~

simulation (year 2018) and developed an offline optical tool to derive optimized *k* values to characterize OA light absorption for each source under study. We used OA mass concentrations derived from ~~Aerosol Chemical Speciation Monitor~~ aerosol chemical speciation monitor (ACSM) and ~~filter based~~ filter-based measurements, and ~~BrC absorption coefficients data~~ OA absorption retrieved from aethalometer ~~measurement at 370 nm as reference datasets.~~

~~Furthermore, we developed an offline optical tool designed to estimate the OA absorption coefficient from the OA mass concentrations calculated from the model. We used the optical tool to derive *k* values at 370 nm that minimize the error with the absorption measured at the 12 monitoring stations in Europe using a Sequential Least Squares algorithm (SLSQP). Bounding values based on Saleh (2020) were imposed to derive the optimized *k* for each station and emission source. The analysis combined optimizations using all the observational data aggregated, exploring the granular information available (source contribution estimates at each monitoring site) and intermediate combinations~~measurements.

~~Overall the MONARCH model shows~~ MONARCH model showed good performance in simulating OA ~~mass concentrations, with good agreement between measured and modeled concentrations for the majority of the stations. The statistical evaluation indicates that most of the stations~~met the evaluation benchmark defined by Emery et al. (2017) concentrations in most stations, meeting the evaluation statistical benchmarks throughout the year~~. The model best performance is identified during spring~~, with peak performance in the spring season. RESI sources (which accounts for domestic heating, cooking, and water heating) ~~emerge as a predominant source of OA mass concentrations during~~ dominated OA concentrations during the colder months. This share may be biased in some European regions by an overrepresentation of residential heating emissions in the CAMS-REG-AP_v42 inventory, as was already highlighted by Navarro-Barboza et al. (2024). ~~The second most relevant contribution to OA mass concentrations comes from secondary organic aerosols (SOA) in most of the stations, particularly~~ SOA emerged as the second most significant contributor, especially during warmer periods at regional sites, such as MSY, HYY, OPE, RIG, and PAY~~. SOA is~~, though slightly underestimated in summer ~~, probably due to low~~ due to likley low biogenic SOA yields used in the ~~simulation for biogenic sources. Furthermore, shipping emissions (SHIP~~

model. SHIP emissions notably affected near-port stations, while TRAF emissions had minimal influence. Despite the limitations identified, the model effectively captured specific events like wildfires and high-pollution episodes, demonstrating its ability to reproduce episodic events.

Optimization of k across stations has underscored the complex, dynamic nature of OA light absorbing properties, influenced not only by emission sources but also by environmental conditions. Derived k values for total OA ranged from 0.005 (weakly absorbing) to 0.068 (weakly to moderately absorbing), indicating significant variability throughout Europe. This aligns with the existing knowledge that OA properties vary with composition, source, and atmospheric age (Cappa et al., 2011). Regional background stations such as MSY and HYY showed the lowest k values, consistent with their predominant biogenic SOA in these regions.

Optimizing k for OA sources highlighted the benefit of source apportionment in characterizing OA light absorbing properties. Our results revealed the significant impact of local and regional emissions on k values. In PAY, elevated k values were derived for GFAS and RESI sources (e.g., biomass, coal combustion), aligned with the known strong absorption characteristics of biomass burning aerosols (Zhang et al., 2020b; Pani et al., 2021). This is further supported by evidence suggesting that BrC from biomass burning can undergo significant dark chemical processing, affecting more than 70% of OA from this source (Kodros et al., 2020). Other regional stations such as HYY, OPE, RIG, and MSY showed the dominance of SOA from biogenic emissions, which explains their low k values (Zhao et al., 2015). In urban environments, TRAF emissions emerged as a significant contributor to light absorption, with derived k values (0.06) twice those reported for specific TRAF emissions (e.g., propane, diesel, gasoline) (Hossen et al., 2023; Lu et al., 2015), highlighting the complexity in urban environments. Stations near ports demonstrated the relevant SHIP contribution to OA light absorption, consistent with previous studies (Kapoor et al., 2023). In summary, we have derived specific ranges of k values at 370 nm for various emission sources using all the granular information available in our study as follows:

– Biomass burning (GFAS): k values range from 0.03 to 0.13. This broad range reflects the variability between stations close to and far from fire sources, highlighting the diverse impact of biomass burning on OA absorption and significance of bleaching processes.

– Residential sources (RESI): k values range from 0.008 to 0.13. Highlighting the variability in residential activities and practices across different regions (e.g., extensive use of coal combustion in KRA).

- Shipping sources (SHIP): Near port areas, k values range from 0.005 to 0.08. In some sites, the second most absorbing source identified in our study in terms of k values.

930
- Traffic (TRAF): k values range from 0.005 to 0.07 i.e., larger than found for specific traffic emission sources in the literature. This result indicate possible unaccounted processes contributing to enhance absorption in urban environments.

- other sources (OTHR): k values range from 0.001 to 0.02. These sources include emissions from power generation, industry,solvents, aviation, waste treatment and disposal, agriculture, etc. and exhibit lower absorption properties indicating the varied influence of emissions on OA absorption.

935 The implementation of these source-specific k values significantly ~~enhances the agreement between modeled and observational data, improving the~~ improves model performance compared to ~~the use of~~ using a constant k value ~~to characterize~~ for OA absorption. This is actually a common practice in ~~several atmospheric models adopting for instance~~ atmospheric models that typically adopt k value at 550 nm ranging from 0.005 to 0.006 (Matsui and Mahowald, 2017; Tegen et al., 2019; Bozzo et al., 2020; Wang et al., 2013; Burgos et al., 2020).

940 This widespread modeling practice underscores the relevance of our findings, proposing a refined method for determining k values that could improve the accuracy of future estimates of BrC radiative forcing.

~~In this sense, we computed and presented the~~ Our analysis of source contribution to OA light absorption at the surface level in Europe~~based on the~~, based on optimized k ~~derived from our analysis. Total absorption is the highest~~ values, revealed highest total absorption in Central and Eastern Europe, with ~~notable~~ hotspots in the Po Valley, Poland, and Romania. ~~Residential sources are the dominant contributors to~~ RESI sources dominante OA absorption, especially ~~during the~~ in colder seasons (DJF, SON)~~. In winter, RESI accounts~~, accounting for 80% of total absorption ~~, a value that decreases to~~ in winter and 28% in summer. ~~Fires (GFAS)~~ GFAS are the second major source, particularly ~~during~~ in summer, while ~~shipping (SHIP) contributes to high absorption levels along major routes, impacting coastal regions . Traffic-related~~ SHIP significantly impacts coastal regions and major shipping routes. TRAF absorption is relatively low ~~,~~ with minor seasonal variability, ~~and presents its major contribution during~~ peaking in winter in central Europe. ~~Lastly, other sources (OTHR) have the lowest contribution~~ OTHR sources contribute minimally to total absorption levels ~~in Europe with reduced~~ with little seasonal variation.

~~Our study also recognizes the limitations of~~ This study acknowledges limitations in current models and emission inventory ~~, which may contribute to~~ that may cause discrepancies between observed and modeled data. ~~For instance, the underestimation of light absorption by OA could result~~ Underestimation of OA light absorption could stem from underpredicted biomass burning or biofuel emissions, ~~as well as~~ uncertainties in particle size and mixing state (Huang et al., 2013). Additionally, the role of BrC may be underestimated in the study, as fossil fuel OA could also be light-absorbing (Lee et al., 2014). Future enhancements should aim at refining emission inventories~~and improving the representation of~~, improving BrC and SOA representation in atmospheric models~~. Moreover, this study underscores the need to increase observational measurements of~~, and increasing BrC light absorption ~~across Europe, which could help further constrain the effect of various sources on OA~~ measurements across Europe to better constrain source effects on OA optical properties.

By establishing a link between laboratory measurements, field observations and modeling experiments, our study offers insights ~~that could improve the representation~~ to advance in the characterization of OA optical properties in ~~global atmospheric models , thereby advancing our understanding of~~ models and reduce the uncertainties in aerosol-climate interactions and their broader environmental implications.

970 *Competing interests.* At least one of the (co-)authors is a member of the editorial board of Atmospheric Chemistry and Physics.

References

Andreae, M., Andreae, T., Annegarn, H., Beer, J., Cachier, H., Le Canut, P., Elbert, W., Maenhaut, W., Salma, I., Wienhold, F., et al.: Airborne studies of aerosol emissions from savanna fires in southern Africa: 2. Aerosol chemical composition, Journal of Geophysical Research: Atmospheres, 103, 32 119–32 128, 1998.

Andreae, M. O. and Gelencsér, A.: Black carbon or brown carbon? the nature of light-absorbing carbonaceous aerosols, Atmospheric Chemistry and Physics, 6, 3131–3148, https://doi.org/10.5194/acp-6-3131-2006, 2006.

Backman, J., Schmeisser, L., Virkkula, A., Ogren, J. A., Asmi, E., Starkweather, S., Sharma, S., Eleftheriadis, K., Uttal, T., Jefferson, A., et al.: On Aethalometer measurement uncertainties and an instrument correction factor for the Arctic, Atmospheric Measurement Techniques, 10, 5039–5062, 2017.

Badia, A. and Jorba, O.: Gas-phase evaluation of the online NMMB/BSC-CTM model over Europe for 2010 in the framework of the AQMEII-Phase2 project, Atmospheric Environment, 115, 657–669, 2015.

Badia, A., Jorba, O., Voulgarakis, A., Dabdub, D., Pérez García-Pando, C., Hilboll, A., Gonçalves Ageitos, M., and Zavisa, J.: Description and evaluation of the Multiscale Online Nonhydrostatic AtmospheRe CHemistry model (NMMB-MONARCH) version 1.0: gas-phase chemistry at global scale, Geoscientific Model Development, 10, 609–638, 2017.

Basnet, S., Hartikainen, A., Virkkula, A., Yli-Pirilä, P., Kortelainen, M., Suhonen, H., Kilpeläinen, L., Ihalainen, M., Väätäinen, S., Louhisalmi, J., et al.: Contribution of brown carbon on light absorption in emissions of European residential biomass combustion appliances, EGUsphere, 2023, 1–27, 2023.

Bond, T. C., Anderson, T. L., and Campbell, D.: Calibration and intercomparison of filter-based measurements of visible light absorption by aerosols, Aerosol Science & Technology, 30, 582–600, 1999.

Bond, T. C., Doherty, S. J., Fahey, D. W., Forster, P. M., Berntsen, T., DeAngelo, B. J., Flanner, M. G., Ghan, S., Kärcher, B., Koch, D., et al.: Bounding the role of black carbon in the climate system: A scientific assessment, Journal of geophysical research: Atmospheres, 118, 5380–5552, 2013.

Boylan, J. W. and Russell, A. G.: PM and light extinction model performance metrics, goals, and criteria for three-dimensional air quality models, Atmospheric environment, 40, 4946–4959, 2006.

Bozzetti, C., Daellenbach, K. R., Hueglin, C., Fermo, P., Sciare, J., Kasper-Giebl, A., Mazar, Y., Abbaszade, G., El Kazzi, M., Gonzalez, R., et al.: Size-resolved identification, characterization, and quantification of primary biological organic aerosol at a European rural site, Environmental science & technology, 50, 3425–3434, 2016.

Bozzo, A., Benedetti, A., Flemming, J., Kipling, Z., and Rémy, S.: An aerosol climatology for global models based on the tropospheric aerosol scheme in the Integrated Forecasting System of ECMWF, Geoscientific Model Development, 13, 1007–1034, 2020.

Brege, M. A., China, S., Schum, S., Zelenyuk, A., and Mazzoleni, L. R.: Extreme molecular complexity resulting in a continuum of carbonaceous species in biomass burning tar balls from wildfire smoke, ACS Earth and Space Chemistry, 5, 2729–2739, 2021.

Brown, H., Liu, X., Feng, Y., Jiang, Y., Wu, M., Lu, Z., Wu, C., Murphy, S., and Pokhrel, R.: Radiative effect and climate impacts of brown carbon with the Community Atmosphere Model (CAM5), Atmospheric Chemistry and Physics, 18, 17 745–17 768, 2018.

Burgos, M. A., Andrews, E., Titos, G., Benedetti, A., Bian, H., Buchard, V., Curci, G., Kipling, Z., Kirkevåg, A., Kokkola, H., et al.: A global model–measurement evaluation of particle light scattering coefficients at elevated relative humidity, Atmospheric Chemistry and Physics, 20, 10 231–10 258, 2020.

Cappa, C. D., Che, D. L., Kessler, S. H., Kroll, J. H., and Wilson, K. R.: Variations in organic aerosol optical and hygroscopic properties upon heterogeneous OH oxidation, Journal of Geophysical Research: Atmospheres, 116, 2011.

Cappa, C. D., Onasch, T. B., Massoli, P., Worsnop, D. R., Bates, T. S., Cross, E. S., Davidovits, P., Hakala, J., Hayden, K. L., Jobson, B. T., et al.: Radiative absorption enhancements due to the mixing state of atmospheric black carbon, Science, 337, 1078–1081, 2012.

Casotto, R., Skiba, A., Rauber, M., Strähl, J., Tobler, A., Bhattu, D., Lamkaddam, H., Manousakas, M. I., Salazar, G., Cui, T., Canonaco, F., Samek, L., Ryś, A., El Haddad, I., Kasper-Giebl, A., Baltensperger, U., Necki, J., Szidat, S., Styszko, K., Slowik, J. G., Prévôt, A. S., and Daellenbach, K. R.: Organic aerosol sources in Krakow, Poland, before implementation of a solid fuel residential heating ban, Science of The Total Environment, 855, 158 655, https://doi.org/https://doi.org/10.1016/j.scitotenv.2022.158655, 2023.

Cavalli, F., Viana, M., Yttri, K. E., Genberg, J., and Putaud, J.-P.: Toward a standardised thermal-optical protocol for measuring atmospheric organic and elemental carbon: the EUSAAR protocol, Atmospheric Measurement Techniques, 3, 79–89, https://doi.org/10.5194/amt-3-79-2010, 2010.

Chakrabarty, R., Moosmüller, H., Chen, L.-W., Lewis, K., Arnott, W., Mazzoleni, C., Dubey, M. K., Wold, C., Hao, W., and Kreidenweis, S.: Brown carbon in tar balls from smoldering biomass combustion, Atmospheric Chemistry and Physics, 10, 6363–6370, 2010.

Chakrabarty, R. K., Shetty, N. J., Thind, A. S., Beeler, P., Sumlin, B. J., Zhang, C., Liu, P., Idrobo, J. C., Adachi, K., Wagner, N. L., et al.: Shortwave absorption by wildfire smoke dominated by dark brown carbon, Nature Geoscience, 16, 683–688, 2023.

Chazeau, B., El Haddad, I., Canonaco, F., Temime-Roussel, B., d'Anna, B., Gille, G., Mesbah, B., Prévôt, A. S., Wortham, H., and Marchand, N.: Organic aerosol source apportionment by using rolling positive matrix factorization: Application to a Mediterranean coastal city, Atmospheric environment: X, 14, 100 176, 2022.

Chen, G., Canonaco, F., Tobler, A., Aas, W., Alastuey, A., Allan, J., Atabakhsh, S., Aurela, M., Baltensperger, U., Bougiatioti, A., et al.: European aerosol phenomenology- 8: Harmonised source apportionment of organic aerosol using 22 Year-long ACSM/AMS datasets, Environment international, 166, 107 325, 2022.

Cheng, Z., Atwi, K., Hajj, O. E., Ijeli, I., Fischer, D. A., Smith, G., and Saleh, R.: Discrepancies between brown carbon light-absorption properties retrieved from online and offline measurements, Aerosol Science and Technology, 55, 92–103, 2021.

Chin, M., Ginoux, P., Kinne, S., Torres, O., Holben, B. N., Duncan, B. N., Martin, R. V., Logan, J. A., Higurashi, A., and Nakajima, T.: Tropospheric aerosol optical thickness from the GOCART model and comparisons with satellite and Sun photometer measurements, Journal of the atmospheric sciences, 59, 461–483, 2002.

Ciarelli, G., Aksoyoglu, S., Crippa, M., Jimenez, J.-L., Nemitz, E., Sellegri, K., Äijälä, M., Carbone, S., Mohr, C., O'Dowd, C., et al.: Evaluation of European air quality modelled by CAMx including the volatility basis set scheme, Atmospheric Chemistry and Physics, 16, 10 313–10 332, 2016.

Corbin, J. C., Pieber, S. M., Czech, H., Zanatta, M., Jakobi, G., Massabò, D., Orasche, J., El Haddad, I., Mensah, A. A., Stengel, B., et al.: Brown and black carbon emitted by a marine engine operated on heavy fuel oil and distillate fuels: optical properties, size distributions, and emission factors, Journal of Geophysical Research: Atmospheres, 123, 6175–6195, 2018.

Cuesta-Mosquera, A., Glojek, K., Močnik, G., Drinovec, L., Gregorič, A., Rigler, M., Ogrin, M., Romshoo, B., Weinhold, K., Merkel, M., et al.: Optical properties and simple forcing efficiency of the organic aerosols and black carbon emitted by residential wood burning in rural Central Europe, EGUsphere, 2023, 1–34, 2023.

Daellenbach, K., Bozzetti, C., Křepelová, A., Canonaco, F., Wolf, R., Zotter, P., Fermo, P., Crippa, M., Slowik, J., Sosedova, Y., et al.: Characterization and source apportionment of organic aerosol using offline aerosol mass spectrometry, Atmospheric Measurement Techniques, 9, 23–39, 2016.

Daellenbach, K. R., Stefenelli, G., Bozzetti, C., Vlachou, A., Fermo, P., Gonzalez, R., Piazzalunga, A., Colombi, C., Canonaco, F., Hueglin, C., et al.: Long-term chemical analysis and organic aerosol source apportionment at nine sites in central Europe: source identification and uncertainty assessment, Atmospheric Chemistry and Physics, 17, 13 265–13 282, 2017.

1065 Denier Van Der Gon, H., Bergström, R., Fountoukis, C., Johansson, C., Pandis, S., Simpson, D., and Visschedijk, A. J.: Particulate emissions from residential wood combustion in Europe–revised estimates and an evaluation, Atmospheric Chemistry and Physics, 15, 6503–6519, 2015.

Donner, L. J., Wyman, B. L., Hemler, R. S., Horowitz, L. W., Ming, Y., Zhao, M., Golaz, J.-C., Ginoux, P., Lin, S.-J., Schwarzkopf, M. D., et al.: The dynamical core, physical parameterizations, and basic simulation characteristics of the atmospheric component AM3 of the 1070 GFDL global coupled model CM3, Journal of Climate, 24, 3484–3519, 2011.

Drinovec, L., Močnik, G., Zotter, P., Prévôt, A., Ruckstuhl, C., Coz, E., Rupakheti, M., Sciare, J., Müller, T., Wiedensohler, A., et al.: The" dual-spot" Aethalometer: an improved measurement of aerosol black carbon with real-time loading compensation, Atmospheric measurement techniques, 8, 1965–1979, 2015.

Drinovec, L., Gregorič, A., Zotter, P., Wolf, R., Bruns, E. A., Prévôt, A. S., Petit, J.-E., Favez, O., Sciare, J., Arnold, I. J., et al.: The 1075 filter-loading effect by ambient aerosols in filter absorption photometers depends on the coating of the sampled particles, Atmospheric Measurement Techniques, 10, 1043–1059, 2017.

Emery, C., Liu, Z., Russell, A. G., Odman, M. T., Yarwood, G., and Kumar, N.: Recommendations on statistics and benchmarks to assess photochemical model performance, Journal of the Air & Waste Management Association, 67, 582–598, 2017.

European Commission: Commission Staff Working Paper Establishing Guidelines for Determination of Contributions From the Resuspen- 1080 sion of Particulates Following Winter Sanding or Salting of Roads Under the Directive 2008/50/EC on Ambient Air Quality and Cleaner Air for Europe, http://ec.europa.eu/environment/air/quality/legislation/pdf/sec_2011_0207.pdf, european Commission, SEC(2011) 207, 43pp., 2011.

Favez, O., El Haddad, I., Piot, C., Boréave, A., Abidi, E., Marchand, N., Jaffrezo, J.-L., Besombes, J.-L., Personnaz, M.-B., Sciare, J., et al.: Inter-comparison of source apportionment models for the estimation of wood burning aerosols during wintertime in an Alpine city 1085 (Grenoble, France), Atmospheric Chemistry and Physics, 10, 5295–5314, 2010.

Feng, Y., Ramanathan, V., and Kotamarthi, V.: Brown carbon: a significant atmospheric absorber of solar radiation?, Atmospheric Chemistry and Physics, 13, 8607–8621, 2013.

Flemming, J., Huijnen, V., Arteta, J., Bechtold, P., Beljaars, A., Blechschmidt, A.-M., Diamantakis, M., Engelen, R. J., Gaudel, A., Inness, A., et al.: Tropospheric chemistry in the Integrated Forecasting System of ECMWF, Geoscientific model development, 8, 975–1003, 2015.

1090 Forrister, H., Liu, J., Scheuer, E., Dibb, J., Ziemba, L., Thornhill, K. L., Anderson, B., Diskin, G., Perring, A. E., Schwarz, J. P., et al.: Evolution of brown carbon in wildfire plumes, Geophysical Research Letters, 42, 4623–4630, 2015.

Freney, E., Zhang, Y., Croteau, P., Amodeo, T., Williams, L., Truong, F., Petit, J.-E., Sciare, J., Sarda-Esteve, R., Bonnaire, N., et al.: The second ACTRIS inter-comparison (2016) for Aerosol Chemical Speciation Monitors (ACSM): Calibration protocols and instrument performance evaluations, Aerosol Science and Technology, 53, 830–842, 2019.

1095 Fröhlich, R., Cubison, M., Slowik, J., Bukowiecki, N., Prévôt, A., Baltensperger, U., Schneider, J., Kimmel, J., Gonin, M., Rohner, U., et al.: The ToF-ACSM: a portable aerosol chemical speciation monitor with TOFMS detection, Atmospheric Measurement Techniques, 6, 3225–3241, 2013.

Gasteiger, J. and Wiegner, M.: MOPSMAP v1. 0: a versatile tool for the modeling of aerosol optical properties, Geoscientific Model Development, 11, 2739–2762, 2018.

1100 Glojek, K., Thuy, V. D. N., Weber, S., Uzu, G., Manousakas, M., Elazzouzi, R., Džepina, K., Darfeuil, S., Ginot, P., Jaffrezo, J., et al.: Annual variation of source contributions to PM10 and oxidative potential in a mountainous area with traffic, biomass burning, cement-plant and biogenic influences, Environment international, p. 108787, 2024.

Granier, C., Darras, S., van der Gon, H. D., Jana, D., Elguindi, N., Bo, G., Michael, G., Marc, G., Jalkanen, J.-P., Kuenen, J., et al.: The Copernicus atmosphere monitoring service global and regional emissions (April 2019 version), Ph.D. thesis, Copernicus Atmosphere
1105 Monitoring Service, 2019.

Guenther, A., Karl, T., Harley, P., Wiedinmyer, C., Palmer, P. I., and Geron, C.: Estimates of global terrestrial isoprene emissions using MEGAN (Model of Emissions of Gases and Aerosols from Nature), Atmospheric Chemistry and Physics, 6, 3181–3210, https://doi.org/10.5194/acp-6-3181-2006, 2006.

Guevara, M., Tena, C., Porquet, M., Jorba, O., and Pérez García-Pando, C.: HERMESv3, a stand-alone multi-scale atmospheric emission
1110 modelling framework–Part 1: global and regional module, Geoscientific Model Development, 12, 1885–1907, 2019.

Guevara, M., Tena, C., Porquet, M., Jorba, O., and Pérez García-Pando, C.: HERMESv3, a stand-alone multi-scale atmospheric emission modelling framework–Part 2: The bottom–up module, Geoscientific Model Development (GMD), 13, 873–903, 2020.

Hanisch, F. and Crowley, J. N.: The heterogeneous reactivity of gaseous nitric acid on authentic mineral dust samples, and on individual mineral and clay mineral components, Physical Chemistry Chemical Physics, 3, 2474–2482, 2001.

1115 Heikkinen, L., Äijälä, M., Daellenbach, K. R., Chen, G., Garmash, O., Aliaga, D., Graeffe, F., Räty, M., Luoma, K., Aalto, P., et al.: Eight years of sub-micrometre organic aerosol composition data from the boreal forest characterized using a machine-learning approach, Atmospheric Chemistry and Physics, 21, 10 081–10 109, 2021.

Hems, R. F., Schnitzler, E. G., Liu-Kang, C., Cappa, C. D., and Abbatt, J. P.: Aging of atmospheric brown carbon aerosol, ACS Earth and Space Chemistry, 5, 722–748, 2021.

1120 Hess, M., Koepke, P., and Schult, I.: Optical properties of aerosols and clouds: The software package OPAC, Bulletin of the American meteorological society, 79, 831–844, 1998.

Ho, C. S., Lv, Z., Peng, J., Zhang, J., Choe, T.-H., Zhang, Q., Du, Z., and Mao, H.: Optical properties of vehicular brown carbon emissions: Road tunnel and chassis dynamometer tests, Environmental Pollution, 320, 121 037, 2023.

Hoffer, A., Tóth, A., Nyirő-Kósa, I., Pósfai, M., and Gelencsér, A.: Light absorption properties of laboratory-generated tar ball particles,
1125 Atmospheric Chemistry and Physics, 16, 239–246, 2016.

Hoffer, A., Tóth, Á., Pósfai, M., Chung, C. E., and Gelencsér, A.: Brown carbon absorption in the red and near-infrared spectral region, Atmospheric Measurement Techniques, 10, 2353–2359, 2017.

Hossen, M. A.-a., Roy, S., Zaman, S. U., and Salam, A.: Emission of water soluble brown carbon from different combustion sources: optical properties and functional group characterisation, Environmental Research Communications, 5, 081 002, 2023.

1130 Huang, Y., Wu, S., Dubey, M., and French, N.: Impact of aging mechanism on model simulated carbonaceous aerosols, Atmospheric Chemistry and Physics, 13, 6329–6343, 2013.

In't Veld, M., Alastuey, A., Pandolfi, M., Amato, F., Perez, N., Reche, C., Via, M., Minguillon, M. C., Escudero, M., and Querol, X.: Compositional changes of PM2. 5 in NE Spain during 2009–2018: A trend analysis of the chemical composition and source apportionment, Science of the Total Environment, 795, 148 728, 2021.

1135 In't Veld, M., Khare, P., Hao, Y., Reche, C., Pérez, N., Alastuey, A., Yus-Díez, J., Marchand, N., Prevot, A. S., Querol, X., et al.: Characterizing the sources of ambient PM10 organic aerosol in urban and rural Catalonia, Spain, Science of the Total Environment, 902, 166 440, 2023.

Jaeglé, L., Quinn, P., Bates, T., Alexander, B., and Lin, J.-T.: Global distribution of sea salt aerosols: new constraints from in situ and remote sensing observations, Atmospheric Chemistry and Physics, 11, 3137–3157, 2011.

1140 Janjic, Z. and Gall, L.: Scientific documentation of the NCEP nonhydrostatic multiscale model on the B grid (NMMB). Part 1 Dynamics, Tech. rep., NATIONAL CENTER FOR ATMOSPHERIC RESEARCH, 2012.

Janjic, Z. I., Gerrity Jr, J., and Nickovic, S.: An alternative approach to nonhydrostatic modeling, Monthly Weather Review, 129, 1164–1178, 2001.

Jorba, O., Dabdub, D., Blaszczak-Boxe, C., Pérez, C., Janjic, Z., Baldasano, J., Spada, M., Badia, A., and Gonçalves, M.: Potential sig-
1145 nificance of photoexcited NO2 on global air quality with the NMMB/BSC chemical transport model, Journal of Geophysical Research: Atmospheres, 117, 2012.

Kaiser, J., Heil, A., Andreae, M., Benedetti, A., Chubarova, N., Jones, L., Morcrette, J.-J., Razinger, M., Schultz, M., Suttie, M., et al.: Biomass burning emissions estimated with a global fire assimilation system based on observed fire radiative power, Biogeosciences, 9, 527–554, 2012.

1150 Kapoor, T. S., Phuleria, H. C., Sumlin, B., Shetty, N., Anurag, G., Bansal, M., Duhan, S. S., Khan, M. S., Laura, J. S., Manwani, P., et al.: Optical Properties and Refractive Index of Wintertime Aerosol at a Highly Polluted North-Indian Site, Journal of Geophysical Research: Atmospheres, 128, e2022JD038 272, 2023.

Kirchstetter, T. W., Novakov, T., and Hobbs, P. V.: Evidence that the spectral dependence of light absorption by aerosols is affected by organic carbon, Journal of Geophysical Research: Atmospheres, 109, 2004.

1155 Klose, M., Jorba, O., Gonçalves Ageitos, M., Escribano, J., Dawson, M. L., Obiso, V., Di Tomaso, E., Basart, S., Montané Pinto, G., Macchia, F., et al.: Mineral dust cycle in the Multiscale Online Nonhydrostatic AtmospheRe CHemistry model (MONARCH) version 2.0, Geoscientific Model Development, 14, 6403–6444, 2021.

Kodros, J., Papanastasiou, D., Paglione, M., Masiol, M., Squizzato, S., Florou, K., Kołodziejczyk, A., Skyllakou, K., Nenes, A., and Pandis, S.: The oxidizing power of the dark side: Rapid nocturnal aging of biomass burning as an overlooked source of oxidized organic aerosol,
1160 in: EGU General Assembly Conference Abstracts, EGU General Assembly Conference Abstracts, p. 7382, 2020.

Kuenen, J., Dellaert, S., Visschedijk, A., Jalkanen, J.-P., Super, I., and Denier van der Gon, H.: CAMS-REG-v4: a state-of-the-art high-resolution European emission inventory for air quality modelling, Earth System Science Data, 14, 491–515, 2022.

Kumar, N. K., Corbin, J. C., Bruns, E. A., Massabó, D., Slowik, J. G., Drinovec, L., Močnik, G., Prati, P., Vlachou, A., Baltensperger, U., et al.: Production of particulate brown carbon during atmospheric aging of residential wood-burning emissions, Atmospheric Chemistry
1165 and Physics, 18, 17 843–17 861, 2018.

Lana, A., Bell, T. G., Simó, R., Vallina, S. M., Ballabrera-Poy, J., Kettle, A. J., Dachs, J., Bopp, L., Saltzman, E. S., Stefels, J., Johnson, J. E., and Liss, P. S.: An updated climatology of surface dimethylsulfide concentrations and emission fluxes in the global ocean, Global Biogeochemical Cycles, 25, https://doi.org/https://doi.org/10.1029/2010GB003850, 2011.

Lanz, V., Prévôt, A., Alfarra, M., Weimer, S., Mohr, C., DeCarlo, P., Gianini, M., Hueglin, C., Schneider, J., Favez, O., et al.: Characterization
1170 of aerosol chemical composition with aerosol mass spectrometry in Central Europe: an overview, Atmospheric Chemistry and Physics, 10, 10 453–10 471, 2010.

Laskin, A., Laskin, J., and Nizkorodov, S. A.: Chemistry of atmospheric brown carbon, Chemical reviews, 115, 4335–4382, 2015.

Lee, H. J., Aiona, P. K., Laskin, A., Laskin, J., and Nizkorodov, S. A.: Effect of solar radiation on the optical properties and molecular composition of laboratory proxies of atmospheric brown carbon, Environmental science & technology, 48, 10 217–10 226, 2014.

1175　Li, L., Dubovik, O., Derimian, Y., Schuster, G. L., Lapyonok, T., Litvinov, P., Ducos, F., Fuertes, D., Chen, C., Li, Z., et al.: Retrieval of aerosol components directly from satellite and ground-based measurements, Atmospheric Chemistry and Physics, 19, 13 409–13 443, 2019.

Li, Q., Liu, D., Jiang, X., Tian, P., Wu, Y., Li, S., Hu, K., Liu, Q., Huang, M., Li, R., et al.: Concurrent photochemical whitening and darkening of ambient brown carbon, Atmospheric Chemistry and Physics, 23, 9439–9453, 2023.

1180　Liakakou, E., Stavroulas, I., Kaskaoutis, D., Grivas, G., Paraskevopoulou, D., Dumka, U., Tsagkaraki, M., Bougiatioti, A., Oikonomou, K., Sciare, J., et al.: Long-term variability, source apportionment and spectral properties of black carbon at an urban background site in Athens, Greece, Atmospheric environment, 222, 117 137, 2020.

Lin, G., Penner, J. E., Flanner, M. G., Sillman, S., Xu, L., and Zhou, C.: Radiative forcing of organic aerosol in the atmosphere and on snow: Effects of SOA and brown carbon, Journal of Geophysical Research: Atmospheres, 119, 7453–7476, 2014.

1185　Liu, J., Bergin, M., Guo, H., King, L., Kotra, N., Edgerton, E., and Weber, R.: Size-resolved measurements of brown carbon in water and methanol extracts and estimates of their contribution to ambient fine-particle light absorption, Atmospheric Chemistry and Physics, 13, 12 389–12 404, 2013.

Liu, J., Lin, P., Laskin, A., Laskin, J., Kathmann, S. M., Wise, M., Caylor, R., Imholt, F., Selimovic, V., and Shilling, J. E.: Optical properties and aging of light-absorbing secondary organic aerosol, Atmospheric Chemistry and Physics, 16, 12 815–12 827, 2016.

1190　Liu, Q., Xu, X., Zhao, W., Zhou, J., Rahman, M. M., Cai, Y., Wang, S., Fang, B., and Zhang, W.: Broadband spectrum characteristics and radiative effects of primary brown carbon from wood pyrolysis, Science of The Total Environment, 882, 163 500, 2023.

Lu, Z., Streets, D. G., Winijkul, E., Yan, F., Chen, Y., Bond, T. C., Feng, Y., Dubey, M. K., Liu, S., Pinto, J. P., et al.: Light absorption properties and radiative effects of primary organic aerosol emissions, Environmental science & technology, 49, 4868–4877, 2015.

Luo, B., Kuang, Y., Huang, S., Song, Q., Hu, W., Li, W., Peng, Y., Chen, D., Yue, D., Yuan, B., et al.: Parameterizations of size distribution and
1195　refractive index of biomass burning organic aerosol with black carbon content, Atmospheric Chemistry and Physics, 22, 12 401–12 415, 2022.

Manubens-Gil, D., Vegas-Regidor, J., Prodhomme, C., Mula-Valls, O., and Doblas-Reyes, F. J.: Seamless management of ensemble climate prediction experiments on HPC platforms, pp. 895–900, 2016.

Massabò, D., Caponi, L., Bernardoni, V., Bove, M., Brotto, P., Calzolai, G., Cassola, F., Chiari, M., Fedi, M., Fermo, P., et al.: Multi-
1200　wavelength optical determination of black and brown carbon in atmospheric aerosols, Atmospheric Environment, 108, 1–12, 2015.

Mathai, S., Veghte, D., Kovarik, L., Mazzoleni, C., Tseng, K.-P., Bucci, S., Capek, T., Cheng, Z., Marinoni, A., and China, S.: Optical Properties of Individual Tar Balls in the Free Troposphere, Environmental science & technology, 57, 16 834–16 842, 2023.

Matsui, H. and Mahowald, N.: Development of a global aerosol model using a two-dimensional sectional method: 2. Evaluation and sensitivity simulations, Journal of Advances in Modeling Earth Systems, 9, 1887–1920, 2017.

1205　Methymaki, G., Bossioli, E., Boucouvala, D., Nenes, A., and Tombrou, M.: Brown carbon absorption in the Mediterranean basin from local and long-range transported biomass burning air masses, Atmospheric Environment, 306, 119 822, 2023.

Metzger, S., Dentener, F., Pandis, S., and Lelieveld, J.: Gas/aerosol partitioning: 1. A computationally efficient model, Journal of Geophysical Research: Atmospheres, 107, ACH–16, 2002.

Middlebrook, A. M., Bahreini, R., Jimenez, J. L., and Canagaratna, M. R.: Evaluation of composition-dependent collection efficiencies for
1210　the aerodyne aerosol mass spectrometer using field data, Aerosol Science and Technology, 46, 258–271, 2012.

Minguillón, M. C., Perron, N., Querol, X., Szidat, S., Fahrni, S. M., Alastuey, A., Jimenez, J. L., Mohr, C., Ortega, A. M., Day, D., et al.: Fossil versus contemporary sources of fine elemental and organic carbonaceous particulate matter during the DAURE campaign in Northeast Spain, Atmospheric Chemistry and Physics, 11, 12 067–12 084, 2011.

Mishchenko, M. I., Travis, L. D., and Lacis, A. A.: Scattering, absorption, and emission of light by small particles, Cambridge university press, 2002.

Moosmüller, H., Chakrabarty, R., and Arnott, W.: Aerosol light absorption and its measurement: A review, Journal of Quantitative Spectroscopy and Radiative Transfer, 110, 844–878, 2009.

Müller, T. and Fiebig, M.: ACTRIS In Situ Aerosol: Guidelines for Manual QC of AE33 absorption photometer data, https://www.actris-ecac.eu/, accessed on 3 January 2024, 2018.

Nakayama, T., Matsumi, Y., Sato, K., Imamura, T., Yamazaki, A., and Uchiyama, A.: Laboratory studies on optical properties of secondary organic aerosols generated during the photooxidation of toluene and the ozonolysis of α-pinene, Journal of Geophysical Research: Atmospheres, 115, 2010.

Nakayama, T., Sato, K., Matsumi, Y., Imamura, T., Yamazaki, A., and Uchiyama, A.: Wavelength dependence of refractive index of secondary organic aerosols generated during the ozonolysis and photooxidation of α-pinene, Sola, 8, 119–123, 2012.

Navarro-Barboza, H., Pandolfi, M., Guevara, M., Enciso, S., Tena, C., Via, M., Yus-Díez, J., Reche, C., Pérez, N., Alastuey, A., et al.: Uncertainties in source allocation of carbonaceous aerosols in a Mediterranean region, Environment international, 183, 108 252, 2024.

Neyestani, S. E. and Saleh, R.: Observationally constrained representation of brown carbon emissions from wildfires in a chemical transport model, Environmental Science: Atmospheres, 2, 192–201, 2022.

Ng, N. L., Herndon, S. C., Trimborn, A., Canagaratna, M. R., Croteau, P., Onasch, T. B., Sueper, D., Worsnop, D. R., Zhang, Q., Sun, Y., et al.: An Aerosol Chemical Speciation Monitor (ACSM) for routine monitoring of the composition and mass concentrations of ambient aerosol, Aerosol Science and Technology, 45, 780–794, 2011.

Obiso, V.: Assessment of dynamic aerosol-radiation interaction in atmospheric models, 2018.

Okuljar, M., Garmash, O., Olin, M., Kalliokoski, J., Timonen, H., Niemi, J. V., Paasonen, P., Kontkanen, J., Zhang, Y., Hellén, H., et al.: Influence of anthropogenic emissions on the composition of highly oxygenated organic molecules in Helsinki: a street canyon and urban background station comparison, Atmospheric Chemistry and Physics, 23, 12 965–12 983, 2023.

Pai, S. J., Heald, C. L., Pierce, J. R., Farina, S. C., Marais, E. A., Jimenez, J. L., Campuzano-Jost, P., Nault, B. A., Middlebrook, A. M., Coe, H., et al.: An evaluation of global organic aerosol schemes using airborne observations, Atmospheric Chemistry and Physics (Online), 20, 2020.

Pandolfi, M., Querol, X., Alastuey, A., Jimenez, J., Jorba, O., Day, D., Ortega, A., Cubison, M., Comerón, A., Sicard, M., et al.: Effects of sources and meteorology on particulate matter in the Western Mediterranean Basin: An overview of the DAURE campaign, Journal of Geophysical Research: Atmospheres, 119, 4978–5010, 2014.

Pani, S. K., Lin, N.-H., Griffith, S. M., Chantara, S., Lee, C.-T., Thepnuan, D., and Tsai, Y. I.: Brown carbon light absorption over an urban environment in northern peninsular Southeast Asia, Environmental Pollution, 276, 116 735, 2021.

Paraskevopoulou, D., Kaskaoutis, D., Grivas, G., Bikkina, S., Tsagkaraki, M., Vrettou, I., Tavernaraki, K., Papoutsidaki, K., Stavroulas, I., Liakakou, E., et al.: Brown carbon absorption and radiative effects under intense residential wood burning conditions in Southeastern Europe: New insights into the abundance and absorptivity of methanol-soluble organic aerosols, Science of The Total Environment, 860, 160 434, 2023.

Park, R. J., Kim, M. J., Jeong, J. I., Youn, D., and Kim, S.: A contribution of brown carbon aerosol to the aerosol light absorption and its radiative forcing in East Asia, Atmospheric Environment, 44, 1414–1421, 2010.

Pérez, C., Haustein, K., Jorba Casellas, O., Janjic, Z., Huneeus, N., Baldasano Recio, J. M., Black, T., Basart, S., Nickovic, S., Miller, R., et al.: Atmospheric dust modeling from meso to global scales with the online NMMB/BSC-Dust model–Part 1: Model description, annual simulations and evaluation, Atmospheric Chemistry and Physics, 11, 13 001–13 027, 2011.

Putaud, J.-P., Cavalli, F., Crippa, M., et al.: Long-term trends in black carbon from biomass and fossil fuel combustion detected at the JRC atmospheric observatory in Ispra, 2018.

Qin, Y. M., Tan, H. B., Li, Y. J., Li, Z. J., Schurman, M. I., Liu, L., Wu, C., and Chan, C. K.: Chemical characteristics of brown carbon in atmospheric particles at a suburban site near Guangzhou, China, Atmospheric Chemistry and Physics, 18, 16 409–16 418, 2018.

Riemer, N., Vogel, H., Vogel, B., Schell, B., Ackermann, I., Kessler, C., and Hass, H.: Impact of the heterogeneous hydrolysis of N2O5 on chemistry and nitrate aerosol formation in the lower troposphere under photosmog conditions, Journal of Geophysical Research: Atmospheres, 108, https://doi.org/https://doi.org/10.1029/2002JD002436, 2003.

Saleh, R.: From measurements to models: toward accurate representation of brown carbon in climate calculations, Current Pollution Reports, 6, 90–104, 2020.

Saleh, R., Robinson, E. S., Tkacik, D. S., Ahern, A. T., Liu, S., Aiken, A. C., Sullivan, R. C., Presto, A. A., Dubey, M. K., Yokelson, R. J., et al.: Brownness of organics in aerosols from biomass burning linked to their black carbon content, Nature Geoscience, 7, 647–650, 2014.

Saleh, R., Marks, M., Heo, J., Adams, P. J., Donahue, N. M., and Robinson, A. L.: Contribution of brown carbon and lensing to the direct radiative effect of carbonaceous aerosols from biomass and biofuel burning emissions, Journal of Geophysical Research: Atmospheres, 120, 10–285, 2015.

Saleh, R., Cheng, Z., and Atwi, K.: The brown–black continuum of light-absorbing combustion aerosols, Environmental Science & Technology Letters, 5, 508–513, 2018.

Sand, M., Samset, B. H., Myhre, G., Gliß, J., Bauer, S. E., Bian, H., Chin, M., Checa-Garcia, R., Ginoux, P., Kipling, Z., et al.: Aerosol absorption in global models from AeroCom phase III, Atmospheric Chemistry and Physics, 21, 15 929–15 947, 2021.

Sarwar, G., Simon, H., Bhave, P., and Yarwood, G.: Examining the impact of heterogeneous nitryl chloride production on air quality across the United States, Atmospheric Chemistry and Physics, 12, 6455–6473, 2012.

Savadkoohi, M., Pandolfi, M., Reche, C., Niemi, J. V., Mooibroek, D., Titos, G., Green, D. C., Tremper, A. H., Hueglin, C., Liakakou, E., et al.: The variability of mass concentrations and source apportionment analysis of equivalent black carbon across urban Europe, Environment international, 178, 108 081, 2023.

Segelstein, D. J.: The complex refractive index of water, Ph.D. thesis, University of Missouri–Kansas City, 1981.

Sekula, P., Ustrnul, Z., Bokwa, A., Bochenek, B., and Zimnoch, M.: Random forests assessment of the role of atmospheric circulation in PM10 in an urban area with complex topography, Sustainability, 14, 3388, 2022.

Skiba, A., Styszko, K., Tobler, A., Casotto, R., Gorczyca, Z., Furman, P., Samek, L., Wideł, D., Zimnoch, M., Kasper-Giebl, A., et al.: Source attribution of carbonaceous fraction of particulate matter in the urban atmosphere based on chemical and carbon isotope composition, Scientific Reports, 14, 7234, 2024.

Spada, M.: Development and evaluation of an atmospheric aerosol module implemented within the NMMB/BSC-CTM, Ph.D. thesis, Universitat Politècnica de Catalunya, 2015.

Spada, M., Jorba, O., Pérez García-Pando, C., Janjic, Z., and Baldasano, J.: Modeling and evaluation of the global sea-salt aerosol distribution: sensitivity to size-resolved and sea-surface temperature dependent emission schemes, Atmospheric Chemistry and Physics, 13, 11 735–11 755, 2013.

Takemura, T., Nozawa, T., Emori, S., Nakajima, T. Y., and Nakajima, T.: Simulation of climate response to aerosol direct and indirect effects with aerosol transport-radiation model, Journal of Geophysical Research: Atmospheres, 110, 2005.

Tegen, I., Neubauer, D., Ferrachat, S., Siegenthaler-Le Drian, C., Bey, I., Schutgens, N., Stier, P., Watson-Parris, D., Stanelle, T., Schmidt, H., et al.: The global aerosol–climate model ECHAM6. 3–HAM2. 3–Part 1: Aerosol evaluation, Geoscientific Model Development, 12, 1643–1677, 2019.

Tian, J., Wang, Q., Ma, Y., Wang, J., Han, Y., and Cao, J.: Impacts of biomass burning and photochemical processing on the light absorption of brown carbon in the southeastern Tibetan Plateau, Atmospheric Chemistry and Physics, 23, 1879–1892, 2023.

Tobler, A. K., Skiba, A., Canonaco, F., Močnik, G., Rai, P., Chen, G., Bartyzel, J., Zimnoch, M., Styszko, K., Nęcki, J., et al.: Characterization of non-refractory (NR) PM 1 and source apportionment of organic aerosol in Kraków, Poland, Atmospheric chemistry and physics, 21, 14 893–14 906, 2021.

Tolocka, M. P., Saul, T. D., and Johnston, M. V.: Reactive uptake of nitric acid into aqueous sodium chloride droplets using real-time single-particle mass spectrometry, The Journal of Physical Chemistry A, 108, 2659–2665, 2004.

Turco, M., von Hardenberg, J., AghaKouchak, A., Llasat, M. C., Provenzale, A., and Trigo, R. M.: On the key role of droughts in the dynamics of summer fires in Mediterranean Europe, Scientific reports, 7, 81, 2017.

Urbieta, I. R., Zavala, G., Bedia, J., Gutiérrez, J. M., San Miguel-Ayanz, J., Camia, A., Keeley, J. E., and Moreno, J. M.: Fire activity as a function of fire–weather seasonal severity and antecedent climate across spatial scales in southern Europe and Pacific western USA, Environmental Research Letters, 10, 114 013, 2015.

Valenzuela, A., Olmo, F., Lyamani, H., Antón, M., Titos, G., Cazorla, A., and Alados-Arboledas, L.: Aerosol scattering and absorption Angström exponents as indicators of dust and dust-free days over Granada (Spain), Atmospheric Research, 154, 1–13, 2015.

Via, M., Minguillón, M. C., Reche, C., Querol, X., and Alastuey, A.: Increase in secondary organic aerosol in an urban environment, Atmospheric Chemistry and Physics, 21, 8323–8339, 2021.

Wang, J., Nie, W., Cheng, Y., Shen, Y., Chi, X., Wang, J., Huang, X., Xie, Y., Sun, P., Xu, Z., et al.: Light absorption of brown carbon in eastern China based on 3-year multi-wavelength aerosol optical property observations and an improved absorption Ångström exponent segregation method, Atmospheric Chemistry and Physics, 18, 9061–9074, 2018a.

Wang, L., Li, Z., Tian, Q., Ma, Y., Zhang, F., Zhang, Y., Li, D., Li, K., and Li, L.: Estimate of aerosol absorbing components of black carbon, brown carbon, and dust from ground-based remote sensing data of sun-sky radiometers, Journal of Geophysical Research: Atmospheres, 118, 6534–6543, 2013.

Wang, X., Heald, C., Ridley, D., Schwarz, J., Spackman, J., Perring, A., Coe, H., Liu, D., and Clarke, A.: Exploiting simultaneous observational constraints on mass and absorption to estimate the global direct radiative forcing of black carbon and brown carbon, Atmospheric Chemistry & Physics, 2014.

Wang, X., Heald, C. L., Sedlacek, A. J., de Sá, S. S., Martin, S. T., Alexander, M. L., Watson, T. B., Aiken, A. C., Springston, S. R., and Artaxo, P.: Deriving brown carbon from multiwavelength absorption measurements: method and application to AERONET and Aethalometer observations, Atmospheric Chemistry and Physics, 16, 12 733–12 752, 2016.

Wang, X., Heald, C. L., Liu, J., Weber, R. J., Campuzano-Jost, P., Jimenez, J. L., Schwarz, J. P., and Perring, A. E.: Exploring the observational constraints on the simulation of brown carbon, AGUFM, 2018b.

Washenfelder, R., Azzarello, L., Ball, K., Brown, S., Decker, Z., Franchin, A., Fredrickson, C., Hayden, K., Holmes, C., Middlebrook, A., et al.: Complexity in the evolution, composition, and spectroscopy of brown carbon in aircraft measurements of wildfire plumes, Geophysical Research Letters, 49, e2022GL098 951, 2022.

Weingartner, E., Saathoff, H., Schnaiter, M., Streit, N., Bitnar, B., and Baltensperger, U.: Absorption of light by soot particles: determination of the absorption coefficient by means of aethalometers, Journal of Aerosol Science, 34, 1445–1463, 2003.

Wild, O., Zhu, X., and Prather, M. J.: Fast-J: Accurate simulation of in-and below-cloud photolysis in tropospheric chemical models, Journal of Atmospheric Chemistry, 37, 245–282, 2000.

Wolf, R., El-Haddad, I., Slowik, J., Dällenbach, K., Bruns, E., Vasilescu, J., Baltensperger, U., and Prévôt, A.: Contribution of bacteria-like particles to PM2. 5 aerosol in urban and rural environments, Atmospheric environment, 160, 97–106, 2017.

Wong, J. P., Tsagkaraki, M., Tsiodra, I., Mihalopoulos, N., Violaki, K., Kanakidou, M., Sciare, J., Nenes, A., and Weber, R. J.: Atmospheric evolution of molecular-weight-separated brown carbon from biomass burning, Atmospheric Chemistry and Physics, 19, 7319–7334, 2019.

Xiong, R., Li, J., Zhang, Y., Zhang, L., Jiang, K., Zheng, H., Kong, S., Shen, H., Cheng, H., Shen, G., et al.: Global brown carbon emissions from combustion sources, Environmental Science and Ecotechnology, 12, 100 201, 2022.

Yarwood, G., Rao, S., Yocke, M., and Whitten, G.: Updates to the carbon bond chemical mechanism: CB05, Final report to the US EPA, RT-0400675, 8, 13, 2005.

Yli-Juuti, T., Mielonen, T., Heikkinen, L., Arola, A., Ehn, M., Isokääntä, S., Keskinen, H.-M., Kulmala, M., Laakso, A., Lipponen, A., et al.: Significance of the organic aerosol driven climate feedback in the boreal area, Nature Communications, 12, 5637, 2021.

Yus-Díez, J., Bernardoni, V., Močnik, G., Alastuey, A., Ciniglia, D., Ivančič, M., Querol, X., Perez, N., Reche, C., Rigler, M., et al.: Determination of the multiple-scattering correction factor and its cross-sensitivity to scattering and wavelength dependence for different AE33 Aethalometer filter tapes: a multi-instrumental approach, Atmospheric Measurement Techniques, 14, 6335–6355, 2021.

Yus-Díez, J., Via, M., Alastuey, A., Karanasiou, A., Minguillón, M. C., Perez, N., Querol, X., Reche, C., Ivančič, M., Rigler, M., et al.: Absorption enhancement of black carbon particles in a Mediterranean city and countryside: effect of particulate matter chemistry, ageing and trend analysis, Atmospheric Chemistry and Physics, 22, 8439–8456, 2022.

Zgłobicki, W. and Baran-Zgłobicka, B.: Air pollution in major Polish cities in the period 2005–2021: Intensity, effects and attempts to reduce it, Environmental Research, 240, 117 497, 2024.

Zhang, A., Wang, Y., Zhang, Y., Weber, R. J., Song, Y., Ke, Z., and Zou, Y.: Modeling the global radiative effect of brown carbon: a potentially larger heating source in the tropical free troposphere than black carbon, Atmospheric Chemistry and Physics, 20, 1901–1920, 2020a.

Zhang, G., Peng, L., Lian, X., Lin, Q., Bi, X., Chen, D., Li, M., Li, L., Wang, X., Sheng, G., et al.: An improved absorption Ångström exponent (AAE)-based method for evaluating the contribution of light absorption from brown carbon with a high-time resolution, Aerosol and Air Quality Research, 19, 15–24, 2019.

Zhang, Q., Worsnop, D., Canagaratna, M., and Jimenez, J.: Hydrocarbon-like and oxygenated organic aerosols in Pittsburgh: insights into sources and processes of organic aerosols, Atmospheric Chemistry and Physics, 5, 3289–3311, 2005.

Zhang, Y., Albinet, A., Petit, J.-E., Jacob, V., Chevrier, F., Gille, G., Pontet, S., Chrétien, E., Dominik-Sègue, M., Levigoureux, G., et al.: Substantial brown carbon emissions from wintertime residential wood burning over France, Science of the Total Environment, 743, 140 752, 2020b.

Zhao, R., Lee, A. K., Huang, L., Li, X., Yang, F., and Abbatt, J. P.: Photochemical processing of aqueous atmospheric brown carbon, Atmospheric Chemistry and Physics, 15, 6087–6100, 2015.

Supplement of

Characterization of Brown Carbon absorption in different European environments through source contribution analysis

S1   Flowchart of the *k* optimization process

The optimization process described in Section 2.4 is illustrated in the flowchart shown in Figure S1. The procedure starts with the tagging of OA per source derived from MONARCH runs, followed by the application of a priori *k* values imposed based on Saleh (2020). The subsequent steps include calculating absorption and determining *k* values for each source with the SLSQP (Sequential Least Squares Programming) algorithm that minimizes the error with the observed absorption. The process concludes with the resulting optimized *k* values at 370 nm for each component and the calculation of the final OA absorption.
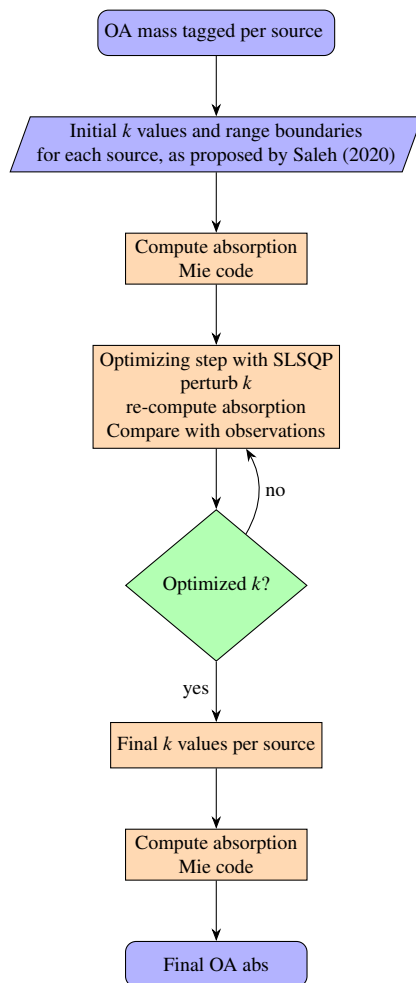
Figure S1. Steps to derive optimized imaginary refractive index k for total or tagged OA.

S2   Statistical metrics

The model results presented in Section 3 are evaluated using five statistical metrics: Normalized Mean Bias (NMB), Normalized Mean Error (NME), Pearson's correlation coefficient (r), Fraction of Predictions within a Factor of Two (FAC2) of observations and Fractional Bias (FB). We followed the performance assessment approach recommended by Emery et al. (2017) for photochemical models, particularly for pollutants such as Elemental Carbon (EC) and Organic Carbon (OC), focusing on metrics including FB, NME, and NMB. These recommendations are based on the "goal" and "criteria" proposed by Boylan and Russell (2006), where the "goal" signifies the peak performance expected from a model, and the "criteria" represent a level of performance that should be achievable by most models. The metrics are defined in Table S1.

Table S1. Statistical metrics used for model performance evaluation. m: model, o: observations.

Metric	Equation	Goal		Criteria	
		OC	EC	OC	EC
Normalized mean bias (NMB)	$\frac{\sum(m_i - o_i)}{\sum o_i} \times 100$	$< \pm 15\%$	$< \pm 20\%$	$< \pm 50\%$	$< \pm 40\%$
Normalized mean error (NME)	$\frac{\sum|m_i - o_i|}{\sum o_i} \times 100$	$< 45\%$	$< 50\%$	$< 65\%$	$< 75\%$
Fractional bias (FB)	$\frac{2}{N}\sum \frac{(m_i - o_i)}{(o_i + o_i)}$	$< \pm 30\%$[a]	$< \pm 30\%$[a]	$< \pm 60\%$[a]	$< \pm 60\%$[a]
Factor two (FAC2)	Fraction where $0.5 < m/o < 2$	–	–	$\geq \pm 50\%$[b]	$\geq \pm 50\%$[b]
Pearson correlation coefficient (r)	$\frac{\sum[(m_i - \overline{m}) \times (o_i - \overline{o})]}{\sqrt{\sum(m_i - \overline{m})^2 \times \sum(o_i + \overline{o})^2}}$	–	–	–	–
Bias	$\frac{\sum(m_i - o_i)}{N}$	–	–	–	–
Root mean square error (RMSE)	$\sqrt{\frac{1}{N}\sum(m_i - o_i)^2}$	–	–	–	–

[a] Recommended FB values for PM by Boylan and Russell (2006).
[b] Recommended metrics for air quality models by Chang and Hanna (2004) and Soni et al. (2021).

S3 Evaluation of OA Concentrations Across Europe

Figure S2 presents scatter plots comparing modeled and observed OA concentrations at the 12 stations. The correlation coefficients (r) vary by site, ranging from 0.21 at MSY to 0.77 at PAY, indicating different levels of agreement between the model and observations. At the KRA and DEM stations, the model tends to overestimate OA concentrations, as indicated by positive fractional bias (FB) values of 32.17 and 34.57, respectively. Conversely, at the HEL and MSY stations, the model underestimates OA concentrations, with negative FB values of -19.31 and -37.90, respectively. Seasonal variations are evident in the scatter plots. Higher concentrations are observed during the DJF (blue) and MAM (orange) seasons, particularly at KRA and RIG, while lower concentrations are seen during the JJA (green) and SON (red) seasons. This seasonal trend highlights the importance of considering temporal variations in OA modeling.
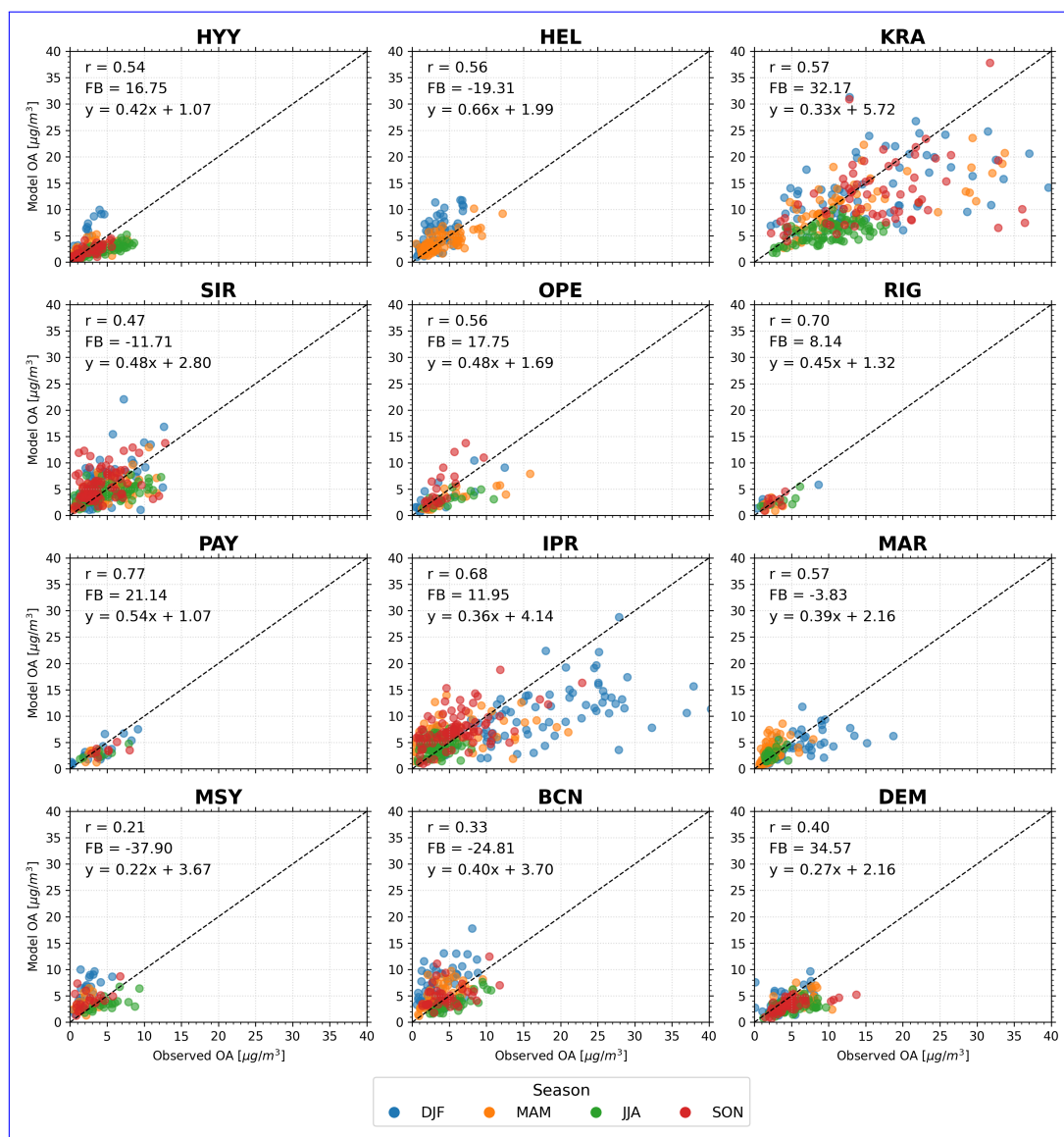
Figure S2. Scatter plots comparing modeled and observed OA concentrations across twelve different locations (HYY, HEL, KRA, SIR, OPE, RIG, PAY, IPR, MAR, MSY, BCN, DEM). Each plot includes data points color-coded by season: DJF (blue), MAM (orange), JJA (green), and SON (red). The plots also display the correlation coefficient (r), fractional bias (FB), and the linear regression equation (y) for each location. The dashed line represents the 1:1 line, indicating perfect agreement between modeled and observed values.

Complementary, Table S2 summarizes the statistical evaluation of the 12 stations (DJF December-January-February; MAM March-April-May; JJA June-July-August; SON September-October-November). In general, the "criteria" are met in most stations and seasons, although some sites fall short of the more stringent "goal". A key trend observed is that the model performs most robustly during the spring season (MAM), with many stations reaching the "goal" and "criteria". In contrast, the summer (JJA) and winter (DJF) seasons exhibit greater variability.

During winter (DJF), several stations show strong correlations, such as HYY ($r = 0.9$), but discrepancies arise in metrics such as FAC2 (e.g., HYY with a low $FAC2 = 23.5$), indicating a tendency to overestimate OA concentrations during this

4

period. This overestimation is likely related to the representation of residential emissions in the model, which are dominant during the colder months. In contrast, during the spring season (MAM) shows improved model performance, particularly at stations such as HEL, were high FAC2 value (93.6%) and strong correlation ($r = 0.7$) suggest a better balance between emission sources and atmospheric processes during this period. Fire emissions, which increase in significance during spring, may contribute to improved accuracy (Urbieta et al., 2015; Turco et al., 2017). Many stations show their best performance during MAM, achieving low FB and NME, such as SIR, which demonstrates consistent accuracy across multiple metrics.

Summer (JJA) and autumn (SON) introduce greater variability in model performance. Some stations, such as KRA in SON, exhibit low correlations ($r = 0.3$), but others maintain high FAC2 values, like PAY in JJA (100%) and RIG in SON (100%). This suggests that, while the model effectively captures overall concentrations in some cases, it faces difficulties with temporal dynamics, particularly the biogenic SOA contributions that become more pronounced during the warmer months. The challenges of modeling biogenic SOA during JJA are particularly evident at stations such as HYY and MSY, where the model underestimates the observed peaks in OA concentrations, driven by SOA formation. Stations like SIR and OPE manage to meet NME and NMB targets in these seasons, despite challenges in FB, as highlighted in gray in Table S2.

Data availability varies across stations, with notable gaps at HEL and MAR during JJA and SON, which limits the ability to fully assess model performance at these locations for those periods. Overall, the analysis indicates that while the model performs well across seasons, particularly in spring, it faces challenges during summer and winter in fully capturing the complex processes driving OA concentrations. These limitations are especially evident in modeling residential emissions during winter and SOA formation in summer.

Table S2. Seasonal statistical evaluation of OA concentrations. Goal achievement (Gray) and criteria benchmarks (Bold) based on Emery et al. (2017). NMB: Normalized Mean Bias, NME: Normalized Mean Error, and FAC2 expressed as percentages.

Metric Season STN	r DJF	FAC2 DJF	FB DJF	NME DJF	NMB DJF	r MAM	FAC2 MAM	FB MAM	NME MAM	NMB MAM	r JJA	FAC2 JJA	FB JJA	NME JJA	NMB JJA	r SON	FAC2 SON	FB SON	NME SON	NMB SON
HYY	0.94	23.53	84.43	146.11	146.11	0.64	**79.17**	**-9.02**	45.37	**-8.63**	0.84	**73.56**	-52.56	43.73	-41.62	0.83	72.13	**-3.78**	39.10	-3.71
HEL	0.65	**66.10**	45.89	70.61	59.55	0.72	**93.59**	**-3.64**	33.46	**-3.58**	nan	nan	nan	nan	nan	nan	nan	nan	nan	nan
KRA	0.53	**73.33**	-26.97	44.80	-23.77	0.67	**90.48**	-20.53	32.72	-18.62	0.55	65.43	-55.38	44.73	-43.37	0.34	74.63	-32.54	41.06	-27.99
SIR	0.61	61.84	28.93	58.73	33.82	0.55	79.27	**-3.06**	37.00	**-3.02**	0.63	**87.78**	**-12.93**	38.48	**-12.14**	0.36	66.25	32.90	64.81	39.37
OPE	0.80	70.59	**-4.48**	45.92	**-4.38**	0.85	68.42	-52.85	43.28	-41.81	0.57	66.67	-51.30	43.48	-40.83	0.78	85.00	29.82	49.58	35.05
RIG	0.94	40.00	**10.77**	53.95	**11.38**	-0.06	71.43	**-14.61**	50.09	**-13.62**	0.77	75.00	**-24.56**	32.22	-21.88	0.61	100.00	**3.16**	26.98	**3.21**
PAY	0.84	76.47	**-12.39**	32.32	**-11.67**	0.09	85.71	**-13.43**	28.80	**-12.58**	0.86	100.00	-32.95	33.78	-28.29	0.51	87.50	-31.94	29.23	-27.54
IPR	0.62	61.54	-50.53	43.89	-40.34	0.33	49.32	**17.31**	70.19	**18.95**	0.26	75.28	**17.77**	45.24	**19.50**	0.52	71.43	**21.84**	52.85	24.51
MAR	0.61	**80.77**	**-29.05**	37.95	-25.36	0.49	**77.78**	38.48	63.81	47.64	0.48	**96.00**	**15.29**	33.37	**16.56**	nan	nan	nan	nan	nan
MSY	0.66	14.29	95.00	180.93	180.93	0.39	57.14	54.86	86.62	75.59	0.63	**86.96**	**-31.59**	29.38	-27.28	0.52	70.00	48.39	69.02	63.84
BCN	0.58	41.82	70.13	112.18	108.01	0.62	**80.00**	28.34	**44.92**	33.02	0.80	**86.96**	-37.33	32.21	-31.46	0.37	75.00	**13.24**	45.74	**14.17**
DEM	0.47	**83.33**	**-0.40**	36.28	**-0.40**	0.41	86.21	-38.31	35.59	-32.15	0.38	72.22	-50.43	42.66	-40.27	0.58	83.02	-32.00	30.10	-27.59

S4   OA concentrations and source contribution at BCN and MSY sites using a local bottom-up emission inventory

Figure S3 shows the time series of OA concentrations and source contributions for BCN and MSY sites derived from a simulation of the MONARCH model using a local bottom-up emission inventory for Spain ~~(HERMESV3_BU Guevara et al., 2020)~~ (HERMESV3_BU; Guevara et al., 2020). The simulation was conducted for the months of January and July with a spatial resolution of $\sim$ 5 km. ~~Main~~ The main differences between HERMESv3_BU and CAMS-REG_v4.2 inventories are discussed in Navarro-Barboza et al. (2024). In contrast to results using the CAMS inventory depicted in Figure ~~4~~3, results with the HERMESv3_BU inventory closely align with observational data in BCN and MSY, particularly during winter. The comparison between the two inventories reveals marked differences in OA component contributions. For instance, with HERMESv3_BU, the residential component is less dominant than with CAMS, and the traffic component becomes more significant. A similar pattern is observed in MSY, where the CAMS inventory results tend to overestimate winter concentrations due to the residential component. These discrepancies highlight the existing constraints of European-scale emission inventories, ~~even though~~ although they remain the most reliable information source at present.
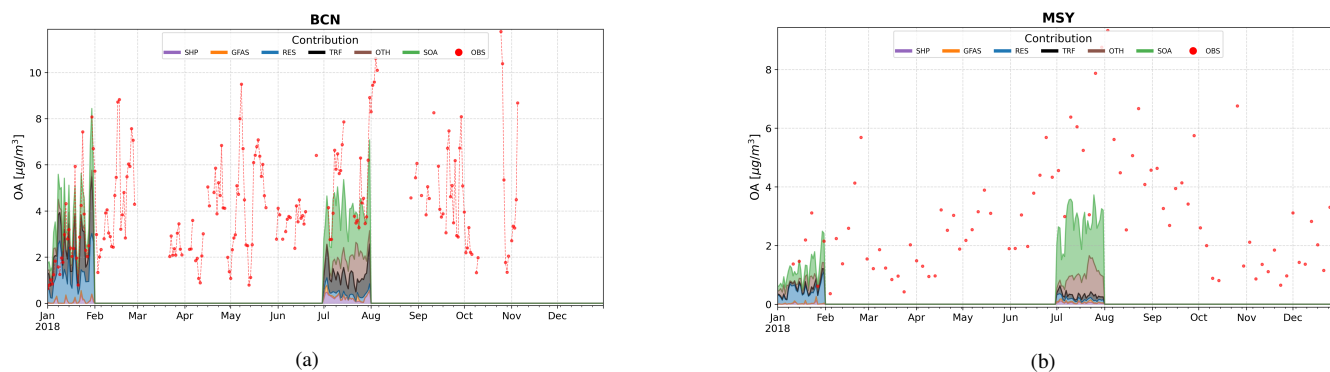
Figure S3. Daily average contributions of OA concentration in BCN (a) and MSY (b) for the year 2018, using the local bottom-up HER-MESv3 emission inventory. Measurements are expressed in $[\mu\,gm^{-3}]$, with each component distinguished by a specific color: Shipping (SHIP) in purple, Fires (GFAS) in orange, Residential (RESI) in blue, Traffic (TRAF) in black, Other (OTHR) in brown, and Secondary OA (SOA) in green. Observational data (OBS) are marked with red dots. Due to the limitations in simulation data availability, only the months of January and July are depicted.

~~Seasonal Comparison of Modeled vs. Observed OA Concentrations Across Europe~~

~~Figure S2 presents scatter plots comparing modeled and observed OA concentrations across twelve stations. The correlation coefficients (r)vary by site, ranging from 0.21 at MSY to 0.77 at PAY, indicating different levels of agreement between the model and observations. At the KRA and DEM stations, the model tends to overestimate OA concentrations, as indicated by~~
70 ~~positive fractional bias (FB) values of 32.17 and 34.57, respectively. Conversely, at the HEL and MSY stations, the model underestimates OA concentrations, with negative FB values of -19.31 and -37.90, respectively. Seasonal variations are evident in the scatter plots. Higher concentrations are observed during the DJF (blue)~~

S5 *k* optimization results

The results of the performed *k* optimization process are summarized in Table S3, which presents the mean and standard
75 deviation (std) of obtained *k* values across stations, classified by representative environments (Regional - REG, Suburban - SUB, Urban - URB; see Table 1), and optimization cases 1 through 4 (Table 3). Each case corresponding to unique assumptions discussed in Sect. 2.5. The mean *k* and std were analyzed for the five sources of study: GFAS, RESI, SHIP, TRAF, and OTHR. The row labeled "ALL" indicates the average values for all stations in Case 4.

Overall, for all settings and cases (1-4), and also for ALL, the highest *k* was obtained for GFAS compared to the other
80 sources with the highest *k* observed for URB sites, whereas similar *k* within the std were obtained at REG and SUB sites. In each setting, small differences were observed between Case 1 (GFAS weakly) and Cases 2 and ~~MAM (orange)seasons, particularly at KRA and RIG, while lower concentrations are seen during the JJA (green)~~4 (GFAS moderately) indicating a robust estimation of GFAS *k* in-between weakly and moderately absorbing OA. Interestingly, in Case 3 (GFAS strongly) *k* reached the lowest allowed limit (cf. Table 3) with zero std (cf. Table S3) suggesting that GFAS OA cannot be treated as
85 strongly absorbing.

RESI OA were considered as weakly absorbing (Cases 1 and ~~SON (red)seasons. This seasonal trend highlights the importance of considering temporal variations in OA modeling~~4) and moderately absorbing (Cases 2 and 3). Similarly to GFAS, higher RESI *k* was obtained for URB sites even if for this source the obtained *k* were comparable, within the std, among the three considered settings. This similarity could be associated with the fact that RESI emissions are mostly local, thus reducing the
90 differences between the station settings. Moreover, for each setting small differences were observed for RESI *k* among the 4 considered Cases suggesting a robust estimation of the RESI *k* that lied in-between weakly and moderately absorbing OA. Note that for both GFAS and RESI the optimization process provided *k* values closer to the upper limit of the weakly category rather than the upper limit of the category moderately.

6

Similarly to RESI, SHIP emissions were considered weakly absorbing in Cases 1 and 4, and moderately absorbing in Cases
95 2 and 3. Overall, the optimization process provided rather similar k among the four Cases at URB sites with k values that were
higher compared to REG and SUB. At URB sites, the SHIP k lied in-between the categories weakly and moderately with k
values that, as for GFAS and RESI, were closer to the lower limit of the category moderately. At SUB sites, the SHIP k reached
the lowest limit allowed for the category weak (0.005; Cases 1 and 4) and moderately (0.02; Cases 2 and 3) suggesting very
low k of SHIP for this setting. At REG sites, SHIP k was higher than at SUB sites with low variability among Cases 1, 2 and 4
100 and higher values and much higher std for case 3. Also for REG sites the optimization process suggest that SHIP OA emissions
were more weakly absorbing than moderately absorbing.

TRAF emissions were treated as very weakly absorbing in Cases 1, 2 and 3 and as weakly absorbing in Case 4. Interestingly,
the highest TRAF k were obtained for URB sites whereas much lower k were obtained at REG and SUB sites. At URB sites,
Cases 1, 2 and 3 provided k values in the upper range of the very weakly category (0.04; cf. Table 3) with very low std
105 suggesting that TRAF emissions were weakly absorbing rather than very weakly absorbing. In fact, Case 4 provided a TRAF
k value of 0.06 that lied in-between the lower and upper limit of the category weakly absorbing. At both SUB and REG sites,
the obtained TRAF k values were much lower compared to URB sites. This result is consistent with recent evidence that OA
from traffic in urban sites can be an important source of brown OA (e.g., Ho et al., 2023). Moreover, traffic emissions are not
expected to be primarily local at REG and SUB sites, thus likely contributing to the observed reduced TRAF k in these two
110 settings due to physico-chemical OA processes as dilution and photobleaching.

OTHR emissions were treated as very weakly absorbing for all the considered cases (1-4). The optimization process provided
very low k values confirming the very low absorption properties of OA particles emitted by OTHR sources. Note that higher
OTHR k values were obtained at URB sites compared to REG and SUB sites where the obtained k were very close to the lower
k value in the category very weakly (cf. Table 3).

Table S3. Statistical summary of mean and standard deviation (std) values for the optimization of the imaginary refractive index across the
three settings (REG, SUB, URB) and the four cases (Case 1, Case 2, Case 3, Case 4). Each case corresponds to different assumptions detailed
in Table 3, analyzed across five OA sources: GFAS, RESI, SHIP, TRAF, and OTHR. The row labeled "ALL" represents the averaged values
across all stations for Case 4.

		GFAS		RESI		SHIP		TRAF		OTHR	
	Metric	mean	std	mean	std	mean	std	mean	std	mean	std
Setting	Case										
REG	Case 1	0.0619	0.0396	0.0458	0.0469	0.0196	0.0168	0.0093	0.0141	0.0015	0.0009
	Case 2	0.0506	0.0434	0.0482	0.0448	0.0210	0.0071	0.0070	0.0139	0.0018	0.0010
	Case 3	0.1241	0.0053	0.0476	0.0447	0.0527	0.0536	0.0068	0.0140	0.0014	0.0005
	Case 4	0.0615	0.0387	0.0451	0.0462	0.0182	0.0150	0.0122	0.0132	0.0014	0.0008
SUB	Case 1	0.0409	0.0154	0.0409	0.0154	0.0049	0.0000	0.0011	0.0000	0.0014	0.0005
	Case 2	0.0403	0.0148	0.0403	0.0148	0.0191	0.0017	0.0011	0.0000	0.0013	0.0003
	Case 3	0.1219	0.0000	0.0395	0.0135	0.0181	0.0000	0.0011	0.0000	0.0011	0.0000
	Case 4	0.0398	0.0146	0.0398	0.0146	0.0049	0.0000	0.0049	0.0000	0.0012	0.0001
URB	Case 1	0.0924	0.0354	0.0635	0.0535	0.0418	0.0481	0.0354	0.0000	0.0098	0.0109
	Case 2	0.0998	0.0238	0.0635	0.0534	0.0445	0.0456	0.0354	0.0000	0.0092	0.0102
	Case 3	0.1229	0.0017	0.0634	0.0535	0.0527	0.0599	0.0345	0.0015	0.0091	0.0110
	Case 4	0.0934	0.0291	0.0625	0.0551	0.0314	0.0458	0.0579	0.0078	0.0081	0.0105
ALL	Case 4	0.0640	0.0342	0.0481	0.0388	0.0182	0.0231	0.0218	0.0229	0.0030	0.0052

115 **S6 Evaluation of absorption results employing different optimized k values**

Figure S4 shows a scatter plot of the observed versus modeled OA absorption at each monitoring site. The plot uses results from Case 4 (all) and Case 5 (all), where k values were obtained using all the monitoring stations combined. To calculate total absorption, Case 4 uses individual k values tailored to specific OA components: 0.0571 for fires, 0.0403 for RESI, 0.0571 for SHIP, 0.0049 for TRAF, and 0.0011 for OTHR. Meanwhile, Case 5 applies a single k value of 0.0187 across all sources. The key difference between the cases is that Case 4 includes a detailed source apportionment, discerning five different OA sources, while Case 5 considers the total OA without source differentiation. Complementary, Figure S5 shows similar results to Figure S4, but using k values optimized for each individual monitoring site (by stn). The statistics and time series for the latter case are presented in Table S4 and Figure S6, respectively.
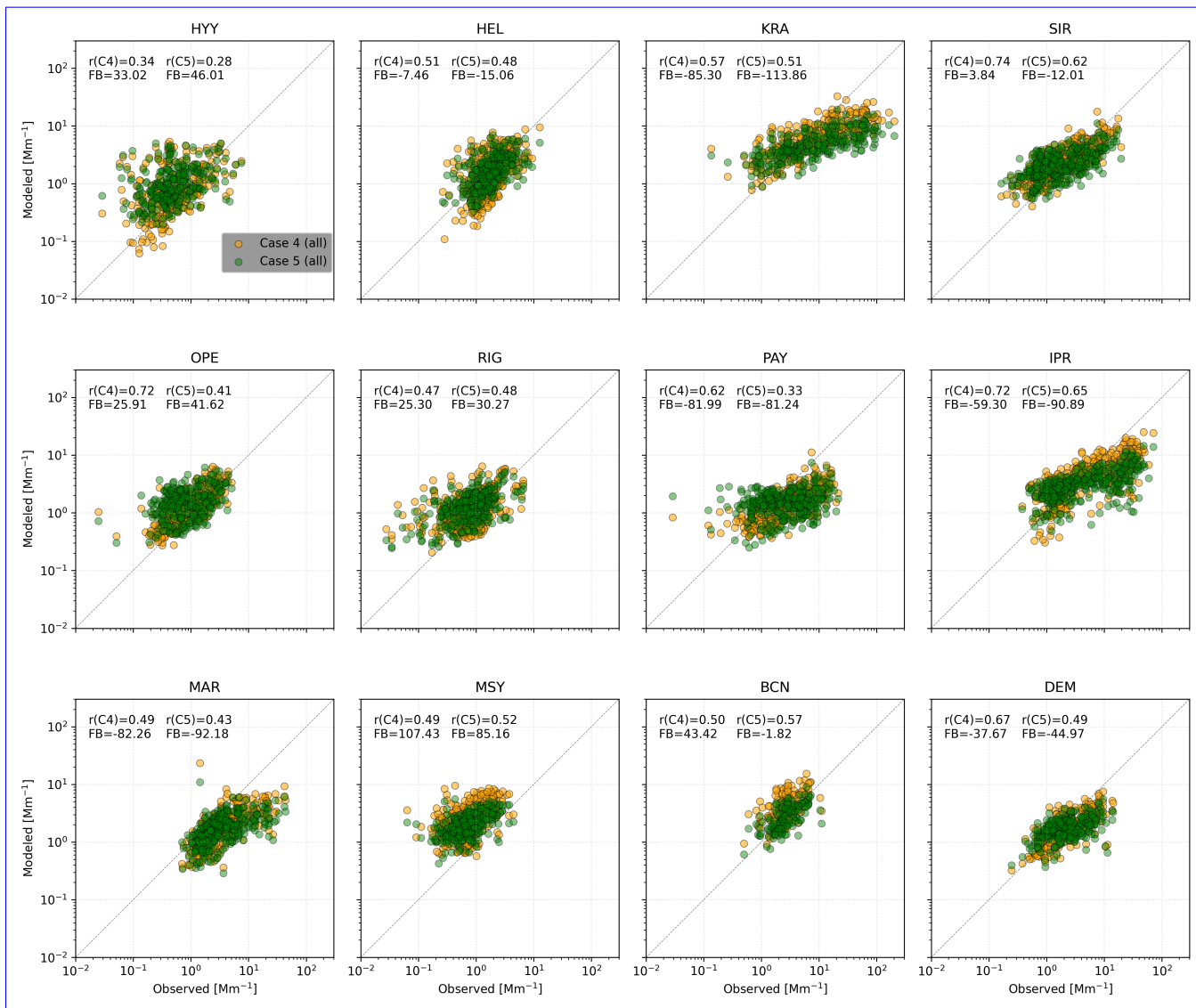
120

8

Figure S4. ~~Scatter plots comparing modeled and~~ Daily mean observed versus modeled OA ~~concentrations across twelve different locations~~ ~~(HYY, HEL, KRA, SIR, OPE, RIG, PAY, IPR, MAR, MSY, BCN, DEM). Each plot includes data points color-coded by season: DJF (blue),~~ ~~MAM~~ absorption for Case 4 (~~orange~~all) ~~, JJA~~ and Case 5 (~~green~~all) scenarios, ~~and SON~~ with the imaginary refractive index (~~red~~*k*) values derived from aggregated data across all monitoring stations. ~~The plots also display~~ Each panel includes the correlation ~~coefficient~~ coefficients (r) ~~,~~ and fractional bias (FB)~~, and the linear regression equation (y) for each location. The dashed line represents the 1:1 line, indicating perfect~~ ~~agreement between modeled and observed values~~.

~~**Statistical metrics**~~

125 ~~Statistical metrics used for model performance evaluation. m: model, o: observations.~~
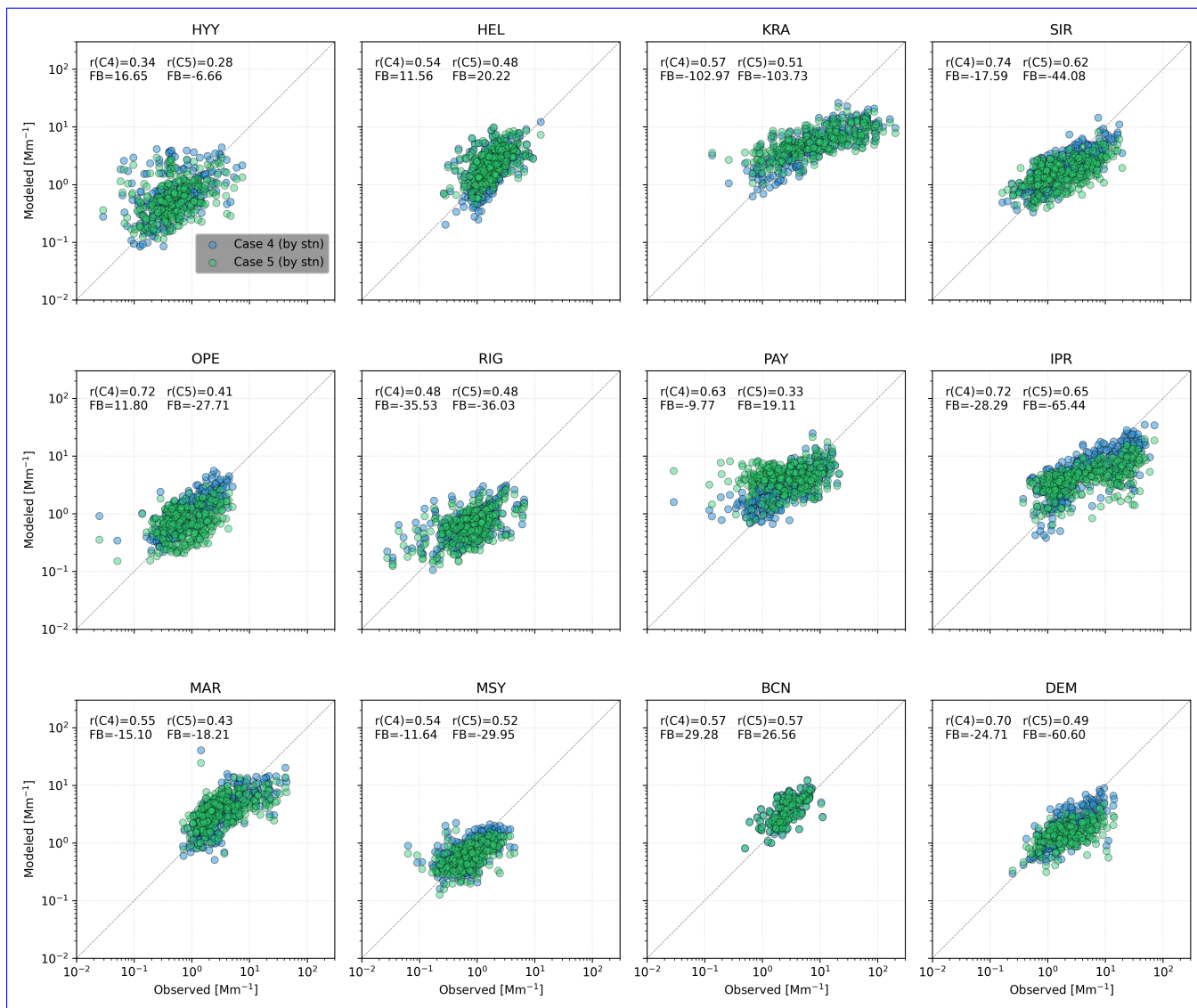
9

Figure S5. Similar to Figure S4, but with *k* derived for each station.

Table S4. Statistical evaluation of absorption results for Cases ~~1 to 5.~~4 and 5 by stn.

| Cases Metric	Case 4 r	FB	FAC2	Case 5 r	FB	FAC2
HYY	0.34	16.65	63.96	0.28	-6.66	58.66
HEL	0.54	11.56	74.79	0.48	20.22	78.08
KRA	0.57	-102.97	48.92	0.51	-103.73	43.17
SIR	0.74	-17.59	71.07	0.62	-44.08	56.75
OPE	0.72	11.80	80.58	0.41	-27.71	56.31
RIG	0.48	-35.53	67.04	0.48	-36.03	67.32
PAY	0.63	-9.77	68.77	0.33	19.11	44.11
IPR	0.72	-28.29	54.40	0.65	-65.44	43.13
MAR	0.55	-15.10	79.32	0.43	-18.21	65.16
MSY	0.54	-11.64	78.63	0.52	-29.95	80.34
BCN	0.57	29.28	77.94	0.57	26.56	80.88
DEM	0.70	-24.71	84.45	0.49	-60.60	62.54
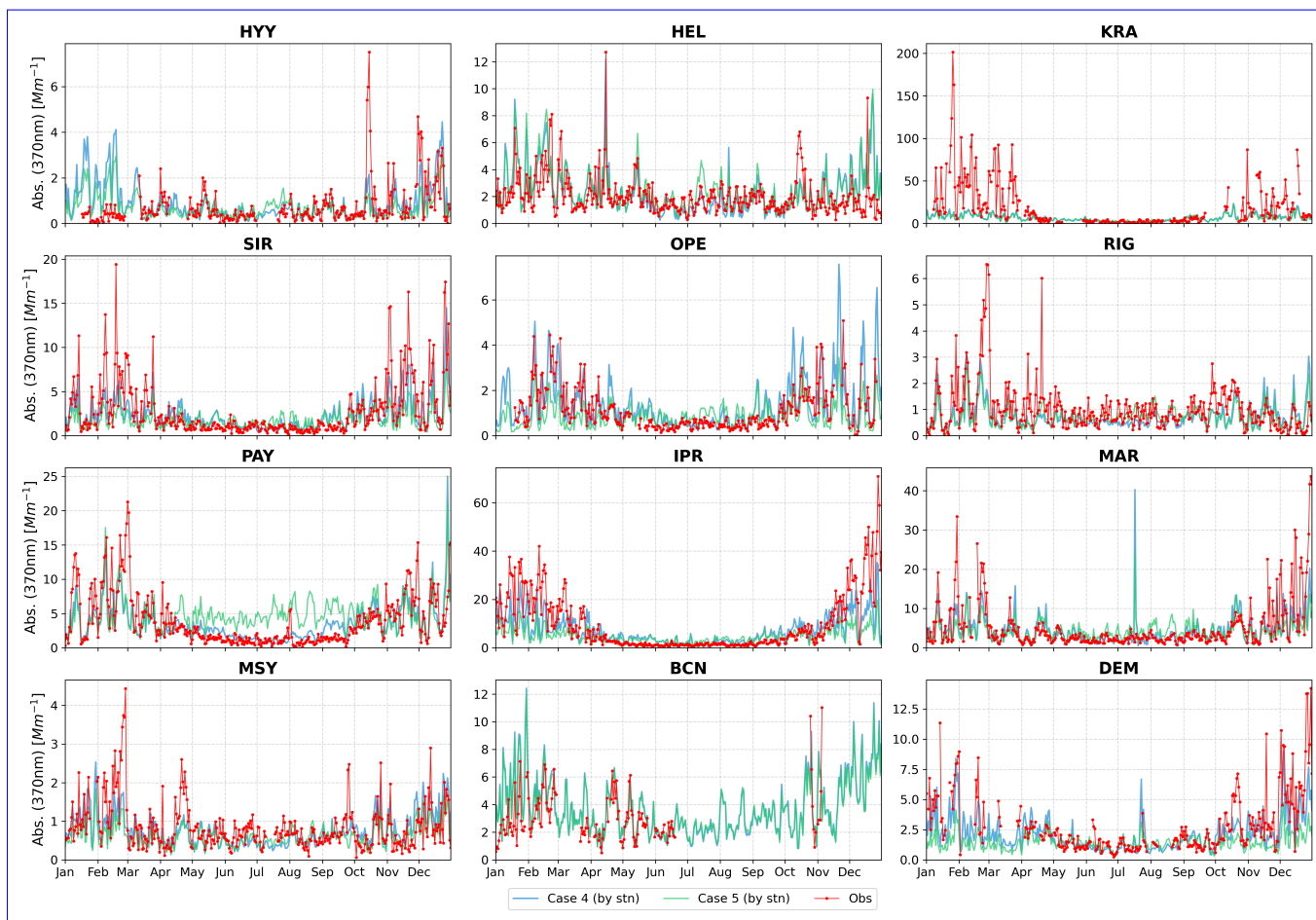
Figure S6. OA light absorption (370 nm) time series for 12 sites. Observed (Obs) in red and modeled absorption for Case 4 (by stn) (blue line) and Case 5 (by stn) (green line). *k* values derived at eact station.

References

Boylan, J. W. and Russell, A. G.: PM and light extinction model performance metrics, goals, and criteria for three-dimensional air quality models, Atmospheric environment, 40, 4946–4959, 2006.

130 Chang, J. C. and Hanna, S. R.: Air quality model performance evaluation, Meteorology and Atmospheric Physics, 87, 167–196, 2004.

Emery, C., Liu, Z., Russell, A. G., Odman, M. T., Yarwood, G., and Kumar, N.: Recommendations on statistics and benchmarks to assess photochemical model performance, Journal of the Air & Waste Management Association, 67, 582–598, 2017.

Guevara, M., Tena, C., Porquet, M., Jorba, O., and Pérez García-Pando, C.: HERMESv3, a stand-alone multi-scale atmospheric emission modelling framework–Part 2: The bottom–up module, Geoscientific Model Development (GMD), 13, 873–903, 2020.

135 Ho, C. S., Lv, Z., Peng, J., Zhang, J., Choe, T.-H., Zhang, Q., Du, Z., and Mao, H.: Optical properties of vehicular brown carbon emissions: Road tunnel and chassis dynamometer tests, Environmental Pollution, 320, 121 037, 2023.

Navarro-Barboza, H., Pandolfi, M., Guevara, M., Enciso, S., Tena, C., Via, M., Yus-Díez, J., Reche, C., Pérez, N., Alastuey, A., et al.: Uncertainties in source allocation of carbonaceous aerosols in a Mediterranean region, Environment international, 183, 108 252, 2024.

Saleh, R.: From measurements to models: toward accurate representation of brown carbon in climate calculations, Current Pollution Reports, 140 6, 90–104, 2020.

Soni, A., Mandariya, A. K., Rajeev, P., Izhar, S., Singh, G. K., Choudhary, V., Qadri, A. M., Gupta, A. D., Singh, A. K., and Gupta, T.: Multiple site ground-based evaluation of carbonaceous aerosol mass concentrations retrieved from CAMS and MERRA-2 over the Indo-Gangetic Plain, Environmental Science: Atmospheres, 1, 577–590, 2021.

Turco, M., von Hardenberg, J., AghaKouchak, A., Llasat, M. C., Provenzale, A., and Trigo, R. M.: On the key role of droughts in the 145 dynamics of summer fires in Mediterranean Europe, Scientific reports, 7, 81, 2017.

Urbieta, I. R., Zavala, G., Bedia, J., Gutiérrez, J. M., San Miguel-Ayanz, J., Camia, A., Keeley, J. E., and Moreno, J. M.: Fire activity as a function of fire–weather seasonal severity and antecedent climate across spatial scales in southern Europe and Pacific western USA, Environmental Research Letters, 10, 114 013, 2015.